

→ HEAVE-PITCH-ROLL ANALYSIS
AND TESTING OF
AIR CUSHION LANDING SYSTEMS

A.B. Eoghani
K.M. Captain
D.N. Wormley

Prepared Under Contract No. NAS1-12403

by

→ Foster-Miller Associates, Inc.
Waltham, MA.

for

National Aeronautics and Space Administration
Langley Research Center
Hampton, VA.

TABLE OF CONTENTS

	<u>Page</u>
SUMMARY	1
INTRODUCTION	2
Background	2
State-of-the-Art Review	3
ANALYSIS	13
Basic Configuration	13
Method of Approach	16
Analytical Development	24
The Static Model	25
The Dynamic Model	30
Subsystem Models	35
The Fan Model	35
The Trunk Model	42
Model Synopsis	58
The Flow System	58
The Force System	59
TESTING	60
Testing Objectives and Plan	60
Test Hardware	64
The Prototype Cushion	64
The Test Rig	68
The Instrumentation	72
Test Procedure	79
Static Tests	79
Dynamic Tests	81
Test Results	82
Parameter Evaluation	8
Trunk Shape and Base Pressure	
Static Characteristics	
Dynamic Characteristics	

TABLE OF CONTENTS (Cont'd)

	<u>Page</u>
VERIFICATION OF ANALYSIS	95
The Static Model	95
The Dynamic Model	99
MODEL USE	112
CONCLUSION	119
APPENDIX. The Equations of the Heave-Pitch-Roll Model . .	121
REFERENCES	190

LIST OF ILLUSTRATIONS

<u>Figure</u>		<u>Page</u>
1	Analytical Models for Cushion and Trunk Flow	7
2	Analytical Models for Trunk Deformation	8
3	Basic ACLS Configuration	14
4	Division of Trunk into Segments	17
5	Inertial and Vehicle Coordinate Frames	18
6	Coordinate Frame Rotation Sequence	23
7	ACLS Flow System	26
8	ACLS Force System	27
9	Fan Model Development	36
10	Static Fan Curve -- Measurement and Analytical Model	40
11	Comparison of Fan Analysis with Experiment	41
12	Measured Trunk Profile	43
13	Outward Excursion of Trunk Segments	44
14	Trunk Model Evaluation - Cushion Height and Width	47
15	Pressure Distribution between Bodies in Contact	48
16	Flow through Porous Plate	50
17	Pressure Distribution in Trunk Contact Zone	51
18	Trunk Element Force Balance	52
19	Trunk Model Evaluation -- Total Load and Load Sharing	54

LIST OF ILLUSTRATIONS (Cont'd)

<u>Figure</u>		<u>Page</u>
20	The Trunk Damping Model	56
21	The Test Rig	63
22	The Test Cushion	65
23	The Test Rib	69
24	The Yoke Assembly	71
25	Trunk Profile Measurement	74
26	Instrumentation System Schematic (Dynamic Tests)	76
27	The Signal Processor	77
28	Frequency Response of the Signal Processor	80
29	Trunk Profile and Base Pressure (Trunk Side) in Heave	85
30	Trunk Profile and Base Pressure (Trunk End) in Heave	86
31	Pressure Variation with Load	87
32	Hard Surface Clearance vs. Load	89
33	Angular Deflection vs. Moment	90
34	Dynamic Test Record (Heave)	92
35	The Stall Behavior of the Cushion	93
36	Dynamic Test Record (Pitch and Roll)	96
37	Static Model Verification -- Heave Deflection	97
38	Static Model Verification -- Cushion and Trunk Pressure	98
39	Static Model Verification -- Pitch and Roll Motion	100
40	Dynamic Model Verification -- Trunk and Cushion Pressure	101
41	Dynamic Model Verification -- Heave Acceleration and Displacement	102
42	Dynamic Model Verification -- Pitch Mode	104
43	Maximum Reduction in Hard Surface Clearance	105

LIST OF ILLUSTRATIONS (Cont'd)

<u>Figure</u>		<u>Page</u>
44	Peak Trunk and Cushion Pressure	107
45	Impact Acceleration and Stall Frequency . . .	108
46	Peak Angular Acceleration	109
47	Pitch and Roll Natural Frequency	110
48	Static Characteristics of Buffalo ACLS . . .	115
49	Landing Dynamics of Buffalo ACLS	116
50	Taxi Dynamics of Buffalo ACLS	118
51	Trunk Sections (Bottom View)	133
52	Trunk Shape	135
53	Hard Surface Clearance	140
54	Trunk Shape Model	144
55	The Position of the Center of Pressure . . .	159
56	Flow Through the ACLS	166
57	Schematic Diagram of Pressure Relief Valve .	187

LIST OF TABLES

<u>Table</u>		<u>Page</u>
I	ACLS Aircraft Development Summary	4
II	Summary of Principal ACLS Literature	5
III	The Test Plan	62
IV	Summary of Instrumentation	73
V	Dynamic Instrumentation Characteristics	78
VI	Model Verification Summary	111
VII	Predicted Equilibrium for Buffalo ACLS	113

HEAVE-PITCH-ROLL ANALYSIS AND TESTING
OF AIR CUSHION LANDING SYSTEMS

A. B. Boghani, K. M. Captain and D. N. Wormley
Foster-Miller Associates, Inc.

SUMMARY

The objective of the investigation was to develop the analytical tools (analysis and computer simulation) needed to explain and predict the dynamic operation of air cushion landing systems (ACLS). The work was carried out through the five tasks listed below.

1. Development of improved analytical models for the fan and trunk
2. Formulation of a heave-pitch-roll analysis for the complete ACLS
3. Development of a general purpose computer simulation to evaluate landing and taxi performance of an ACLS aircraft
4. Verification and refinement of the analysis by comparison with test data obtained through lab testing of a prototype cushion
5. Demonstration of simulation capabilities through typical landing and taxi simulations of an ACLS aircraft.

Initial results show that fan dynamics have a major effect on system performance. Comparison with lab test data (zero forward speed) indicates that the analysis can predict most of the key static and dynamic parameters (pressure, deflection, acceleration, etc.) within a margin of 10-25 percent. The simulation can thus be used to evaluate existing configurations and develop new designs.

INTRODUCTION

Background

The Air Cushion Landing System (ACLS) concept has been applied to several aircraft, such as the Buffalo (XC-8A), the LA-4 and the Jindivik drone. Tests with these aircraft and small scale models have demonstrated both the feasibility of the concept and the advantages of using such a system in place of conventional landing gear. In several instances, however, current designs have exhibited unexpected behavior, and the need for a better understanding of ACLS operation has thus been felt. Recognizing this need, NASA initiated a phased research program to develop the analytical tools necessary to understand and predict ACLS performance. Once the analytical models and verifying experiments are complete, this work will then lead to the design and fabrication of improved second generation air cushion landing systems.

This report represents the completion of the first stage of the research program in which the basic analysis has been developed and subjected to initial verification. The analytical model, based on the fundamentals of solid body and fluid mechanics, determines the heave, pitch and roll motion and pressure, flow and acceleration of an ACLS during landing impact, slideout and taxi. The model has been verified by comparing the analytical results with those obtained from controlled static and dynamic experiments with a prototype cushion in the laboratory. A computer program which incorporates the ACLS analysis has also been developed to evaluate current ACLS designs, and to help in the development of improved configurations.

Subsequent sections of this report describe details of the analytical model, the results of the experimental verification, and a typical application in which the analysis has been used to evaluate the characteristics of the Buffalo aircraft. The computer program itself is not described in this report, but is available to interested users through NASA COSMIC services.

State-of-the-Art Review

The feasibility of Air Cushion Landing Systems was established when an ACLS LA-4 aircraft first flew in 1967. Since that time, several aircraft applications have been studied by the Air Force, Navy and NASA (see Table I) and two of these (Buffalo and Jindivik) have been developed to the point of full-scale testing. Scale model tests of cushions and entire aircraft have also been carried out, including static tests, drop tests, forward speed tests and wind tunnel tests.

Over the last ten years, a number of reports and papers have been published describing this work, from initial feasibility and design studies to subsequent analyses, computer simulations and testing. This literature is summarized in Table II.

The first analysis of a complete ACLS was carried out by Earl (ref. 1). His report on the feasibility of using an ACLS for the C-119 aircraft included a static analysis of the cushion and its subsystems. The static theory was supported by scale model tests.

Digges (ref. 11) also analyzed the complete ACLS, starting with an evaluation of the various jet theories which model the outflow from the trunk and cushion. He compared the flow parameters (e.g., cushion-to-trunk pressure ratio) predicted by the theories for different jet heights. The jet analysis was then expanded to include distributed flow due to distributed trunk holes and the results thus obtained were compared with those found from the flow restrictor theory, which models the air gap as an orifice between the cushion chamber and atmosphere (Figure 1a, 1b). While test results showed that the flow restrictor theory, predicted the cushion flow more accurately than the distributed jet theory, it required specially measured orifice discharge coefficients. Digges also analyzed the trunk shape, assuming that the trunk material behaves like an ideal membrane (Figure 2a). Trunk shapes

TABLE I

ACLS AIRCRAFT DEVELOPMENT SUMMARY

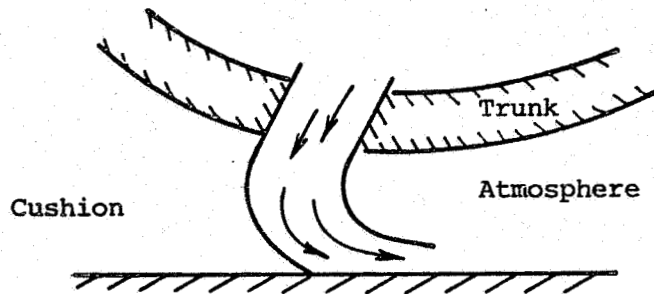
Aircraft Type	Designation	Sponsoring Agency	Development Level		
			Design Study	Model Tests	Full Scale Tests
1. <u>Light Amphibian</u>	LA-4	Bell	x	x	x
2. <u>Transport</u>					
Light	Buffalo	Air Force	x	x	x
Medium	C-119	Air Force	x	x	
Heavy	Span Loader	NASA	x		
3. <u>RPV</u>					
	Jindivik	Air Force	x	x	x
	Ryan 147G	Air Force	x		
4. <u>Fighter</u>					
	A-4	ARPA/Navy	x	x	
	F-8	ARPA/Navy	x	x	
5. <u>Space Shuttle</u>		NASA	x		

TABLE II
SUMMARY OF PRINCIPAL ACLS LITERATURE

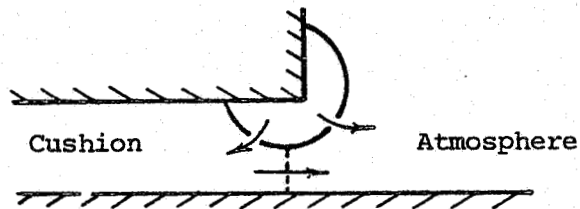
Performing Agency	Date	Principal Author & Reference	Aircraft Selected	ACLS Subsystem Studied	Analysis			Experiment				Remarks		
					Type	Static	Dynamic	Heave	Pitch	Roll	Static Test		Drop Test	Forward Speed Test
Bell Aerospace Co.	5/67	Earl (1)	C-119	Complete ACLS	x		x				1/3 Scale	1/3 Scale	1/12 Scale	Feasibility Study
	8/68	Earl (2)	C-119	Complete ACLS							1/3 Scale	1/3 Scale	1/4 Scale	Extension of Earlier Work
	9/69	Stauffer (3)	LA-4	Complete ACLS							1/3 Scale	1/3 Scale		Prototype ACLS Aircraft
	12/70	Ryken (4)	Space Shuttle	Complete ACLS	x	x	x	x	x					
	5/72	Coles (5)	Buffalo	Complete ACLS	x	x	x	x	x	2D Trunk 1/4 Scale 1/10 Scale	1/4 Scale 1/10 Scale	1/4 Scale 1/10 Scale	1/10 Scale	Includes Computer Simulation Development Design Study
	7/72	Ryken (6)	Ryan 1470 RPV	Complete ACLS	x		x							Similar to Coles' Analysis Design Study
	3/74	Ryken (7)	Jindivik	Complete ACLS	x	x	x	x	x					
	5/74	Earl (8)	Boeing 737	Complete ACLS	x		x							
	11/75	Earl (9)	LA-4	Suction Braking	x								Full Scale	
Wright Patterson AFB	1970	Gorman (10)	-	Peripheral Jet Airflow	x						2D Trunk			Computer Simulation Development
	6/71	Digges (11)	-	Complete ACLS	x	x	x	x			2D Trunk & Prototype Cushion	Prototype Cushion		Computer Simulation Development
	8/72	Vaughan (12)	Jindivik	Complete ACLS	x		x				1/4 Scale	1/4 Scale		
	9/72	Vaughan (13)	Buffalo	Complete ACLS							Ejector and tip turbine fan			
	1973	Kunstadt (14)	Jindivik	Air Source							1/10 Scale	1/10 Scale	1/10 Scale	Results Compared with Full Scale Model
	1973	Parker (15)	Jindivik	Complete ACLS							2D Trunk			
	9/73	Rogers (16)	-	Peripheral Jet Airflow	x						1/10 Scale	1/10 Scale		Results Compared with 1/1 Scale
	9/73	Rodriguez (17)	Buffalo	Complete ACLS							2D Trunk			Lumped parameter mechanical model
	3/74	Carreras (18)	-	Trunk/Cushion Airflow System	x	x	x	x	x					Model Developed from previous experiments
	3/74	Bauer (19)	Jindivik	Mechanical System	x	x	x	x	x					
	3/74	Stuart (20)	Buffalo (Scale Models)	Complete ACLS	x						Full Scale	Full Scale		Includes pull tests
	4/74	Vaughan (21)	Jindivik	Complete ACLS										

TABLE II (CONCLUDED)
SUMMARY OF PRINCIPAL ACLS LITERATURE

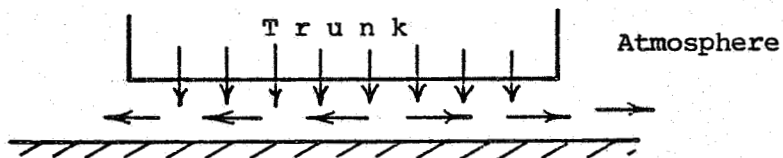
Performing Agency	Date	Principal Author & Reference	Aircraft Selected	ACLS Subsystem Studied	Type Analysis			Experiment				Remarks		
					Static	Dynamic	Heave	Pitch	Roll	Static Test	Drop Test		Forward Speed Test	Wind Tunnel Test
Ohio State	5/71	Han (22)	-	Cushion Airflow	x		x				2D Cushion Airflow test apparatus			Experimental Corroboration of Earlier Theory
	3/72	Han (23)	-	Cushion Airflow							2D Cushion Airflow test apparatus			Trunk Flutter Experiments
	7/75	Han (24)	-	Cushion Airflow							Trunk Flutter Test Apparatus			
	1975	Porzomo (25)	Jindivik	ACLS Trunk										Computer Simulation Development
Foster-Miller Associates	5/75	Captain (26)	-	Complete ACLS	x	x	x	x						
NSDC	2/73	Lee (27)	A-4	Aerodynamic Configuration									221 Model	
Boeing	3/73	Wilms (28)	A-4 (1/3 Scale)	Complete ACLS	x		x				1/3 Scale			
NASA	5/72	Thompson (29)	C-8	Complete ACLS							1/10 Scale			
	3/75	Inland (30)	Navy Fighter	Complete ACLS							0.3 Scale	0.3 Scale		
B.F. Goodrich	2/74	Mc (31)	Jindivik	Complete ACLS	x	x	x	x						Computer Simulation Development
Southwest Research Institute	6/73	Boss (32)	-	ACLS Trunk							Trunk Flutter Test Apparatus			Trunk Flutter Experiments
Sandair	1/73	McCudden (33)	Jindivik	Complete ACLS	x									Design Study
Lockheed	12/72	Hurkamp (34)	Span Loader	Complete ACLS	x									Design Study



(a) Jet Theory (refs. 10, 11, 16)

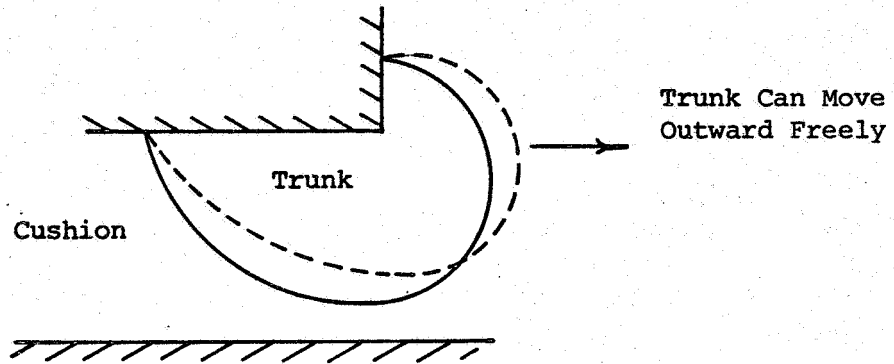


(b) Flow Restrictor Theory (ref. 11)

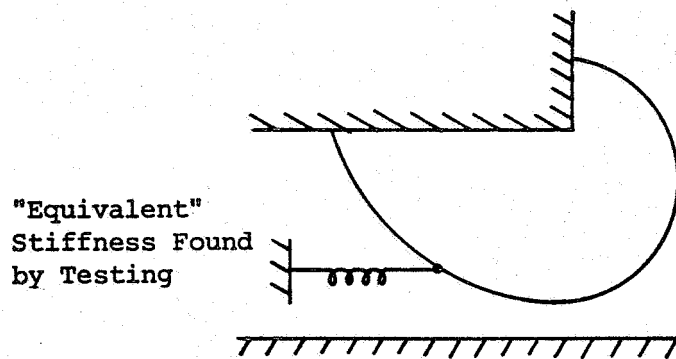


(c) Porous Plate Model (refs. 22, 23)

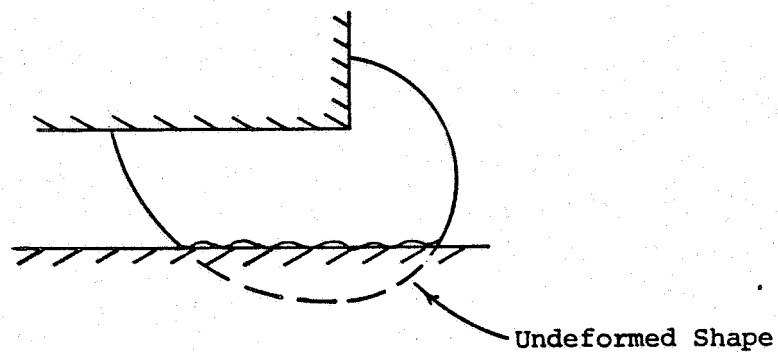
Figure 1. Analytical Models for Cushion and Trunk Flow



(a) Membrane Trunk - No Hoop Stiffness (ref. 11)



(b) Membrane Trunk - With Hoop Stiffness (ref. 5)



(c) "Frozen" trunk (ref. 26)

Figure 2. Analytical Models for Trunk Deformation

were predicted for various cushion-to-trunk pressure ratios and compared with the test results obtained with a straight (2 dimensional) section of trunk. This membrane trunk analysis however did not include the effects of the hoop stress and deflection of an actual (3 dimensional) torroidal trunk.* The trunk shape and cushion flow analysis was used to develop a dynamic model of the ACLS. A dynamic simulation computer program was also developed. Initial test data from a prototype cushion (at zero cushion pressure) were found to be in general agreement with the computer predictions.

A vertical energy absorption analysis for ACLS was performed by Vaughan (ref. 12), who also developed a dynamic simulation computer program. This program was restricted to heave mode simulation. A parametric analysis was performed to determine the effects of the various parameters on the load-stroke response of the system.

An analysis of pitch motion of the ACLS is described by Coles (ref. 5). In this analysis the trunk is divided into sections and the forces and moments for coupled heave-pitch motion are obtained by analyzing each section separately and then summing the results for the whole cushion. Hoop tension effects, not considered by Digges, were approximated in this study by introducing an experimentally calculated radial stiffness in the force balance analysis of the trunk by means of an external spring (Figure 2b). Trunk dynamics were modeled by using auxiliary pressure variables related to the actual pressure variables by first order lags. A computer simulation, which included aircraft aerodynamics, was developed to generate heave-pitch motion predictions of the ACLS during landing impact. Ryken (ref. 7) expanded Coles' analysis

* In this report, the term hoop refers to the trunk lines that run around the (oval) perimeter of the cushion and trunk.

by introducing two additional system pressures (the forward gap and the aft gap) calculated from an experimentally observed exponential relationship. The analysis was used to update the computer program developed by Coles, and various simulations were carried out to predict the behavior of the Jindivik.

In an attempt to include analytically the effects of circumferential tension, Captain (ref. 26) assumed the trunk to be "frozen", i.e., the trunk shape outside the ground contact zone to be fixed, and independent of pressure (Figure 2c). With this assumption, a dynamic heave analysis was developed and subsequently extended to include pitch motion. Computer simulations were developed for both the heave and heave-pitch modes.

A dynamic heave-pitch simulation of the Jindivik is described by Ho (ref. 31) who solved existing analytical models (refs. 2, 23) on a hand calculator.

Simpler approaches to modeling the ACLS have also been taken. In a preliminary study by Bauer (ref. 19), the ACLS is represented by a spring-mass-dashpot model, and the various system parameters are quantified from test data obtained with the full scale Jindivik. Stuart (ref. 20) proposed a similar type of model in which several of the equations were quantified through experiments with scale model cushions for the Buffalo.

In addition to studying the entire ACLS, several reports dealing with specific ACLS subsystems have also been published. The majority of these reports have dealt with the modeling of the fluid interaction between the trunk, cushion and atmosphere. Most of these studies have included experiments on two dimensional trunks with various orifice configurations. Theories used to predict the experimental behavior include the jet theories such as the Barratt, thin jet and exponential theories (Figure 1a) and the flow restrictor theory (Figure 1b). The jet theories generally use change of jet momentum to predict the cushion pressure, whereas the flow restrictor theory considers the gap area under the trunk as an

orifice and predicts the cushion pressure from the orifice equation (refs. 11, 16). The general conclusion drawn from these studies is that the orifice theory is more suitable for ACLS than the jet theories, apparently because a discrete jet pattern is not established. Han (ref. 22) has obtained theoretical results by approximating the trunk-cushion interaction by the airflow through a porous plate (Figure 1c). An experimental verification is also described (ref. 23). The theory works well for low gap heights characteristic of trunk-ground contact, but is not attractive for the larger clearances. More recently, Han (ref. 24) has reported some experimental work on a distributed jet emanating from single, double and triple slot configurations. About the only published studies on ACLS fans is the work of Kunstadt (ref. 14) who evaluated both ejectors and tip turbine fans for the Jindivik.

The general conclusions that emerge from the state-of-the-art review of ACLS model development are as follows.

1. Operation of the trunk-cushion-atmosphere airflow system should be modeled by an orifice theory rather than a jet theory.
2. The trunk model is a known bottleneck that has restricted the advancement of ACLS analysis. Of the three trunk models presently available, the membrane model (Digges) is too "soft" because it neglects hoop tension effects, the "frozen" trunk model (Captain) is too stiff, because it overcompensates for hoop tension, and the model developed by Coles is confined to modes and applications where special trunk test data are available to quantify the model.
3. The pressure distribution under the trunk in the ground contact zone has not been conclusively established. Most analyses assume that during ground contact the trunk forms a perfect seal with contact pressure equal to the trunk pressure. Very little data are available to validate this assumption for a real three dimensional trunk, and further analysis and testing is needed to establish the model for trunk contact pressure and sealing.

4. The air source has not received much attention, and the effects of source dynamics on ACLS landing behavior are largely unknown.
5. Although several computer models have been described in the literature, there is no generally available and experimentally verified simulation that can be used without special test data to evaluate and improve ACLS designs.

The conclusions of the state-of-the-art review helped define the specific tasks needed to address those critical areas that are as yet unresolved. The work was broken down into five tasks:

1. Development of improved models for the fan and trunk
2. Formulation of a heave-pitch-roll analysis for the complete ACLS
3. Development of a general purpose computer simulation to evaluate landing and taxi performance of an ACLS aircraft
4. Verification and refinement of the analysis by comparison with test data obtained through lab testing of a prototype cushion
5. Demonstration of simulation capabilities through typical landing and taxi simulations of an ACLS aircraft

The preceding section has summarized previous work in the field and identified the key areas for further study. The static and dynamic analysis of the ACLS is developed in the next section. All major assumptions are discussed, and the complete ACLS analytical model, including improved models for the trunk and fan, is derived. The full set of equations that describe the model are presented in the Appendix. The test setup and the static and dynamic experiments performed on the prototype cushion* are then presented. The experiments carried out include static heave, pitch and roll tests, in which various ACLS parameters, including

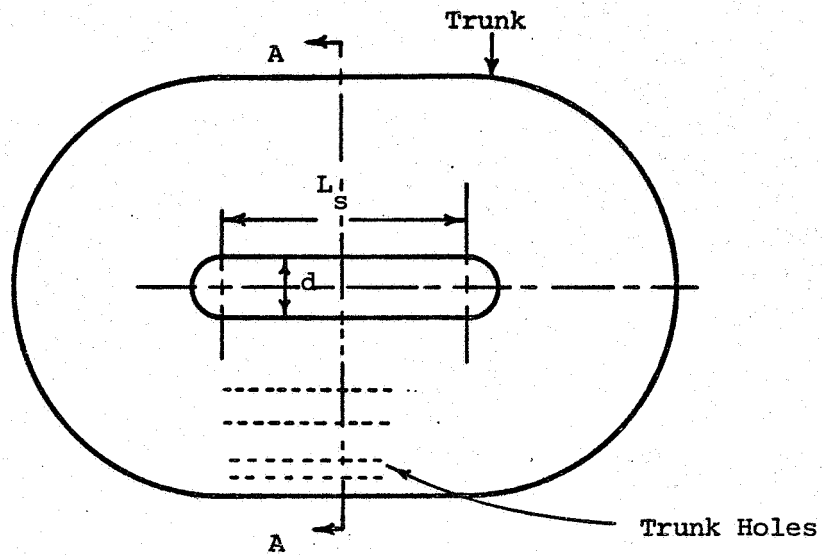
*One half of a 1/3 scale dual cushion landing system built by Boeing under an earlier Navy contract.

ground contact pressure distribution, were measured for different loading conditions. The dynamic tests consist of drop tests from different heights with different angles of attack, pitch and roll moment release tests, and a coupled heave-pitch start-up test. The validity of the analytical model is evaluated by comparison with the test results. Finally, the capabilities of the analytical model are demonstrated by carrying out a computer simulation of the Buffalo aircraft. The results presented include heave and pitch motions, pressures and accelerations during a typical 41 m/s (80 knot) approach and landing, and during taxi over an ungraded runway.

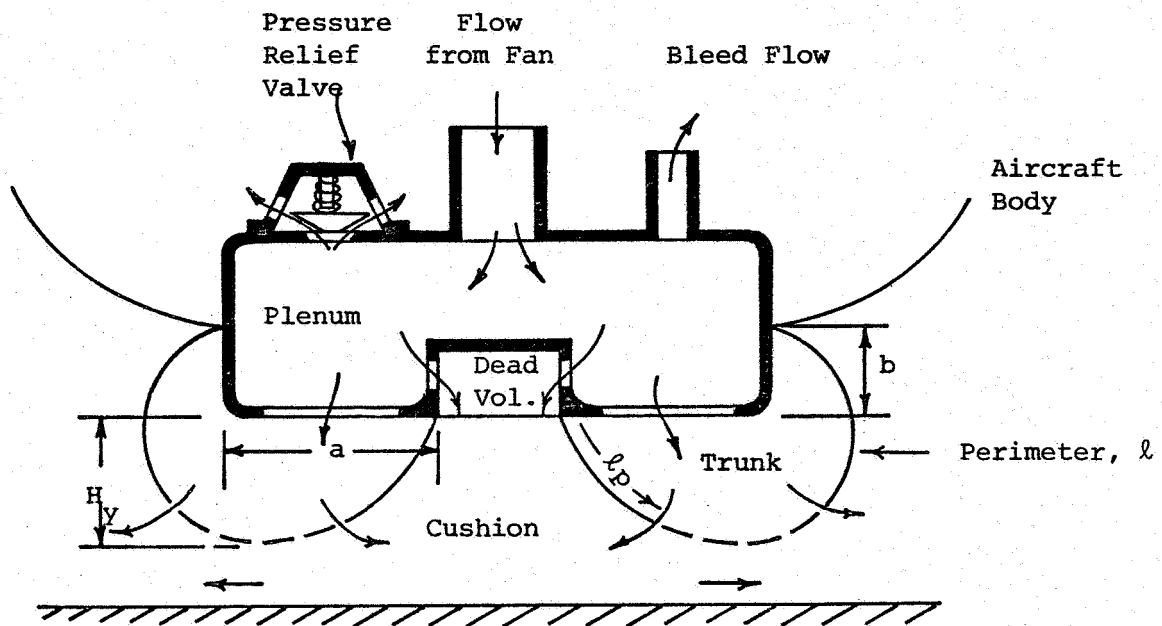
ANALYSIS

Basic Configuration

The basic ACLS configuration analyzed is shown in Figure 3. The model includes four primary subsystems: the fan, the feeding system, the trunk and the cushion. The configuration of these systems has been chosen sufficiently general so that they can represent a variety of practical designs. Air from the fan flows through the ducts and plenum (feeding system) and enters the trunk. The trunk has several rows of orifices that communicate both with the cushion and atmosphere. Thus, the airflow from the trunk has two components - one part entering the cushion and the other leading directly to the atmosphere. The cushion flow exhausts to the atmosphere through the clearance gap formed between the trunk and ground. In addition to the basic flows described above, two other flows have been included in the model for generality. These are the plenum bleed flow and the direct cushion flow. Plenum bleeding causes some of the air to flow directly from plenum to atmosphere, and has been used in some designs to improve the dynamic characteristics of the air supply system. Direct flow from the plenum to the cushion can also improve dynamic response. A pressure relief valve is also included in the basic configuration.



(a) Plan View



(b) Front View (Section A-A)

Figure 3. Basic ACLS Configuration

It allows additional flow to vent from the plenum whenever the pressure exceeds a preset level, and thus improves stability by reducing fan stall.

The support force acting on the aircraft is made up of two components. The first occurs due to the cushion pressure acting over the cushion area. The second, which comes about only during ground contact, is given by the contact pressure acting over the trunk contact area. The support force, in general, also gives rise to a moment, given by the product of the force and its distance from the CG of the aircraft.

In plan, the cushion has an oval shape, made up of a rectangular section with semicircular ends. The lengths a and b are the horizontal and vertical spacing between the points of attachment of the trunk to the aircraft body. The initial (undeformed) trunk shape is defined by the above two parameters, and the perimeter ℓ and height H_y as shown. S_h is the (uniform) spacing between the rows of peripherally distributed orifices. The number and orientation of the orifices is selected independently by the number of orifice rows N_r , the number of orifices per row N_h , and the orientation parameter ℓ_p . The cushion volume consists of two parts: an active (dynamically varying) region and a dead (static) region. The active volume depends on the trunk shape and ground profile. The dead volume, which is a design variable, includes recesses in the cushion cavity as shown.

Method of Approach

The configuration of the cushion was described in the last section. Here, a description of the overall system and the initial steps taken to set up the analytical model are presented.

The landing system forces transferred to the aircraft act through the cushion and trunk. To help calculate these forces, the trunk and cushion are divided into segments as shown in Figure 4. Each straight section of the cushion and trunk is divided into $2M$ rectangular segments, while each curved end is divided into $2N$ pie-shaped segments. Thus the total number of segments is $4(M + N)$. The cushion and trunk parameters are calculated first for each segment and then summed to give their total system values.

The dynamic analysis of the vehicle system is best derived with the help of two orthogonal coordinate frames of reference: a coordinate frame fixed in space (inertial frame), and a coordinate frame fixed to the vehicle (vehicle frame) with origin at the aircraft CG. The reason for two frames can be appreciated by recognizing that

- (a) Newton's law for translational motion can be directly applied to the CG acceleration expressed relative to the inertial frame.
- (b) The corresponding law for rotational motion can be applied more conveniently in the vehicle frame, because rotational inertia about any vehicle axis is constant, while the rotational inertia about any inertial (fixed) axis varies with aircraft position.

Accordingly, the two frames of reference have been defined as shown in Figure 5. The vehicle frame with origin at the aircraft CG has roll, yaw and pitch axes x , y and z respectively fixed to the aircraft body as shown. The inertial frame has corresponding axes X , Y and Z fixed in space. The two frames coincide only when the aircraft has not undergone any rotation from equilibrium.

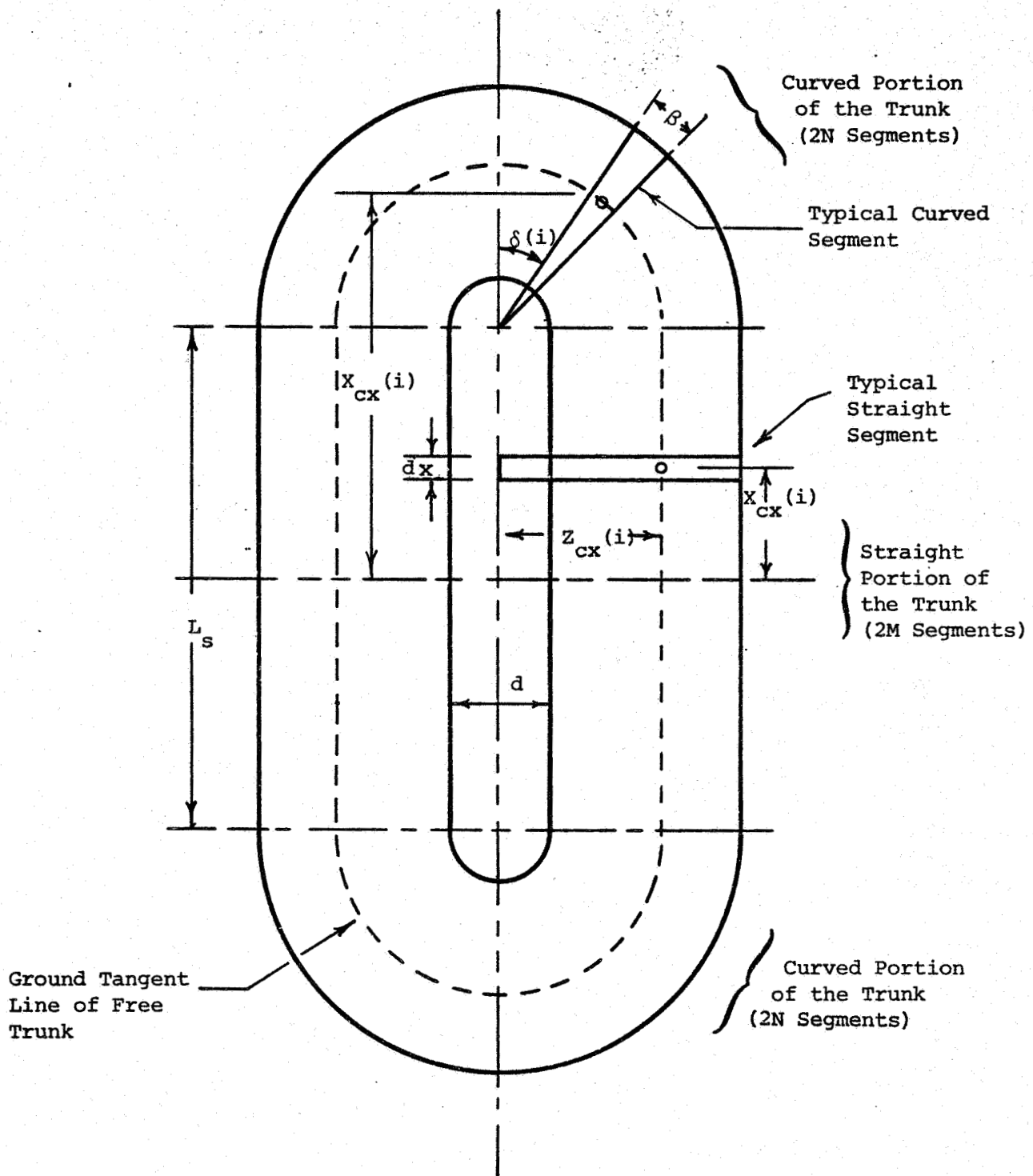
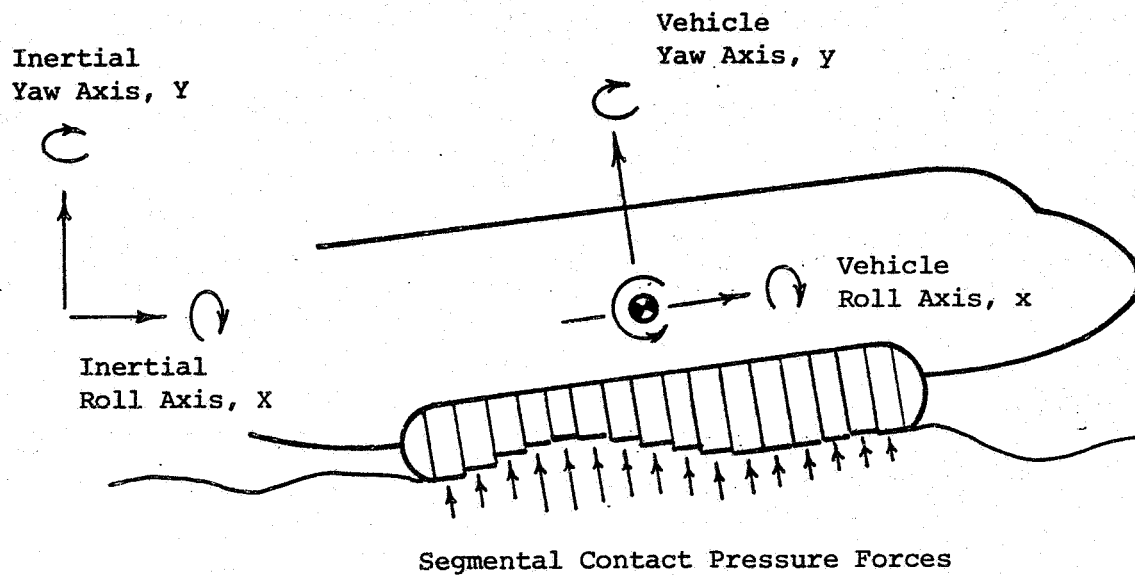
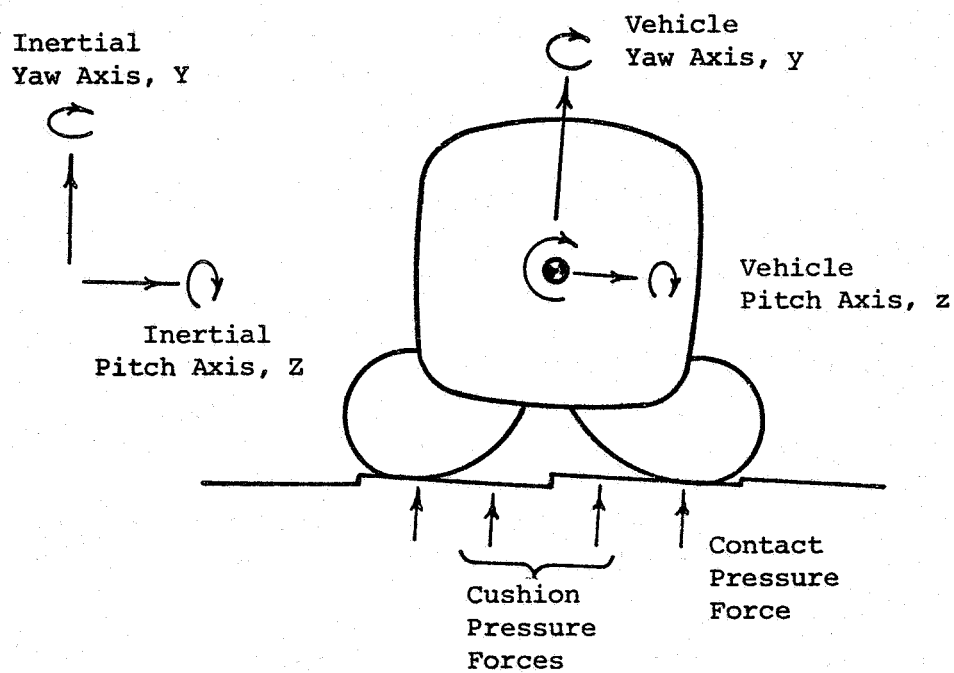


Figure 4. Division of Trunk into Segments



(a) Side View



(b) Front View

Figure 5. Inertial and Vehicle Coordinate Frames

In the analysis, the actual runway profile underneath the ACLS is approximated by segments that coincide in plan with those of the trunk and are parallel to the cushion hard surface as shown in Figure 5. With this model, all pressure forces act parallel to the vehicle yaw axis so that the segment torque component about the aircraft CG can be easily computed by multiplying the segment force by the fore-and-aft and/or lateral separation between the segment and the CG.

The model sketched in Figure 5, and the analysis derived subsequently, has been set up to cover the heave, pitch and roll motion of the aircraft during touchdown, slideout and taxi over an irregular runway. Sideslip forces and yaw moments about the vehicle axis have not been taken into account at this time on the grounds that, in practice, these will be determined by the response of the as yet undefined aircraft steering system. The forward velocity of the aircraft, determined independently of the dynamics, is found from the initial aircraft velocity and the selected braking coefficient.

As mentioned earlier, aircraft translational motion is found by applying Newton's law to the aircraft CG in the inertial frame. Thus for heave (vertical motion)

$$M_a \ddot{Y}_{cg} = F_y \quad (1)$$

where

M_a is the aircraft mass

Y_{cg} is the aircraft CG motion in the inertial vertical direction

and

F_y is the ACLS force in the inertial vertical direction

Similarly, for forward motion

$$\ddot{x}_{cg} = -\mu \quad (2)$$

where x_{cg} is the aircraft CG motion in the inertial forward direction

and μ is the braking coefficient.

For aircraft rotation about the CG, the angular momentum theorem gives

$$\vec{T} = \frac{d}{dt} \vec{H} \quad (3)$$

where \vec{T} is the torque vector about the aircraft CG

and \vec{H} is the angular momentum vector.

Substituting for the generalized angular momentum vector and expressing the above equation in matrix form gives

$$\begin{bmatrix} T_x \\ T_y \\ T_z \end{bmatrix} = \begin{bmatrix} I \\ I \\ I \end{bmatrix} \cdot \begin{bmatrix} \ddot{\theta} \\ \ddot{\psi} \\ \ddot{\phi} \end{bmatrix} + \begin{bmatrix} \dot{\theta} \\ \dot{\psi} \\ \dot{\phi} \end{bmatrix} \times \begin{bmatrix} I \\ I \\ I \end{bmatrix} \cdot \begin{bmatrix} \dot{\theta} \\ \dot{\psi} \\ \dot{\phi} \end{bmatrix} \quad (4)$$

where T_x , T_y and T_z are the torque components acting about the vehicle x, y and z axes

$\dot{\theta}$, $\dot{\psi}$, $\dot{\phi}$, $\ddot{\theta}$, $\ddot{\psi}$, and $\ddot{\phi}$ are the roll, yaw and pitch velocities and accelerations along the vehicle x, y and z axes

and the inertia matrix $[I]$ is given by

$$[I] = \begin{bmatrix} I_x & I_{xy} & I_{zx} \\ I_{xy} & I_y & I_{yz} \\ I_{zx} & I_{yz} & I_z \end{bmatrix}$$

where I_x, I_y, I_z are the moments of inertia of the aircraft along the vehicle x, y and z axes,

and I_{xy}, I_{yz}, I_{zx} are the cross products of inertia.

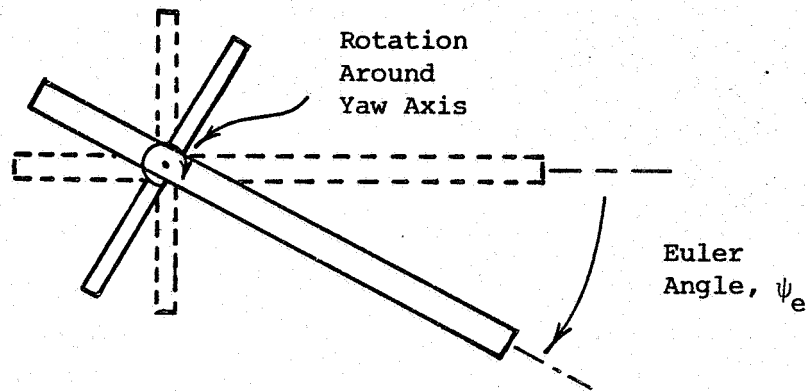
The translational equations of motion, Eqns (1) and (2), can be easily integrated to give the X and Y coordinates of the aircraft CG as a function of time. Integration of the rotational equation of motions, Eqn (4), however is less straightforward, because the end result of the integration which is angular rotation is not a vector and thus cannot be uniquely defined by the angles θ, ψ and ϕ as obtained from the solution of Eqn (4). In problems of this sort, in which it is necessary to uniquely determine the orientation of a body rotating about an arbitrary (and moving) axis, the difficulty is avoided by a coordinate transformation which expresses the rotational equations in terms of Euler angles. Euler angles signify nothing more than angular rotations about prescribed axes carried out in a defined sequence. Unlike conventional angles, the definition of a specific sequence for adding Euler angles allows them to uniquely fix the orientation of a body undergoing rotation about an arbitrary axis.

The Euler angles and rotation sequence adopted for the subsequent analysis is shown in Figure 6. The three steps needed to fix the angular orientation of the aircraft are as follows:

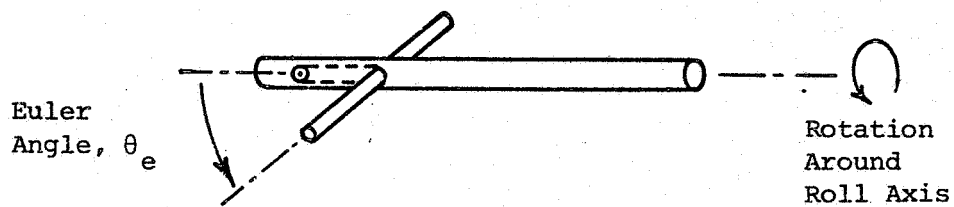
1. Beginning with the vehicle axes parallel to the inertial axes, the first Euler angle rotation ψ_e is made about the inertial yaw axis Y which, at this stage, coincides with the vehicle yaw axis, y . Note that after making this rotation, the inertial and vehicle pitch and roll axes are no longer parallel.
2. The second Euler angle rotation θ_e is made about the vehicle roll axis x . Note that after this rotation, the inertial and vehicle yaw axes are no longer parallel, and the orientation between vehicle and inertial pitch axes has further changed.
3. The third Euler angle rotation ϕ_e is made about the vehicle pitch axis z . Note that after this rotation, the vehicle roll axis has been displaced from the position it had during Step 2.

Thus, in summary, the first rotation is about the inertial yaw axis and the third rotation is about the final pitch axis; both of which are easy to identify. The second rotation however is about the intermediate vehicle roll axis, which is different both from the inertial roll axis due to the rotation of Step 1, and from the final vehicle roll axis due to the rotation of Step 3. Of course, when only pitch-heave simulations are carried out (i.e., when roll excitation is not present), then the Euler roll and yaw angles are zero ($\psi_e = \theta_e = 0$) and the Euler pitch angle ϕ_e coincides with the usual inertial pitch angle ϕ .

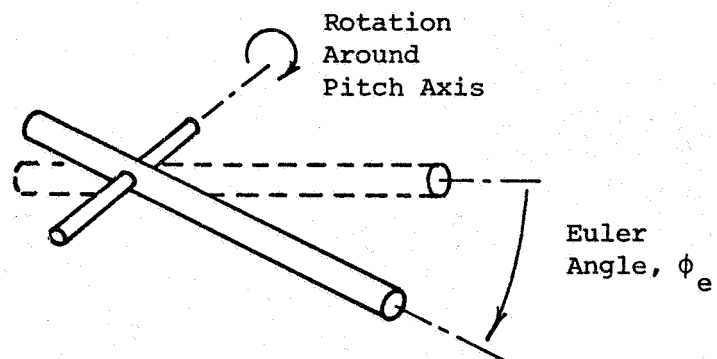
With the above definition, the coordinate transformation can be carried out to give the relationship between the angular velocities in the vehicle frame ($\dot{\theta}, \dot{\psi}, \dot{\phi}$) and the corresponding Euler angles and their derivatives. The derivation, which is presented in the Appendix shows that:



(a) First Rotation



(b) Second Rotation



(c) Third Rotation

Figure 6. Coordinate Frame Rotation Sequence

$$\dot{\theta} = \dot{\psi}_e \sin \phi_e \cos \theta_e + \dot{\theta}_e \cos \phi_e \quad (5)$$

$$\dot{\psi} = \dot{\psi}_e \cos \phi_e \cos \theta_e - \dot{\theta}_e \sin \phi_e \quad (6)$$

$$\dot{\phi} = \dot{\phi}_e - \dot{\psi}_e \sin \theta_e \quad (7)$$

Relationships for vehicle frame acceleration ($\ddot{\theta}$, $\ddot{\psi}$ and $\ddot{\phi}$) can also be obtained by differentiating the above equations with respect to time. When these relationships are substituted into Eqn (4), the differential equation can then be solved to give the Euler angle components, and thus fix the angular orientation of the aircraft as a function of time.

Analytical Development

The analytical model of the ACLS consists of a set of equations which when solved determines the pressures, flows, forces and motion of the system as a function of time for various aircraft and runway parameters. There are two parts to this model:

- (a) The Static Model, which comprises the relationships that determine the static characteristics of the system at equilibrium. In addition to providing design data these relationships also provide the initial conditions for the dynamic model.
- (b) The Dynamic Model, which comprises the differential equations of flow and motion (state equations) from which the pressures, flows, forces and motion can be determined as functions of time.

Before proceeding with the analytical development, it is helpful to divide the overall ACLS into two interrelated systems: the flow system and the force system. These systems are shown in

Figures 7 and 8. The flow system establishes the pressure-flow relationship for the various subsystems of the ACLS. The force system establishes the corresponding force-motion relationships. The interdependence of the two systems comes about because the trunk deflection obtained from the force system changes the volumes and orifice areas that form part of the flow system. Similarly, the cushion and trunk pressures found from the flow system give rise to forces and moments that form inputs to the force system. With the definition of these two systems, the analytical development can now proceed. The primary equations of the static and dynamic models are derived in the subsequent sections. The complete set of equations and symbol list is given in the Appendix.

The Static Model

The equilibrium conditions are found as follows:

- (a) By satisfying the fan flow constraint,

$$Q_{fx} = f(P_f) \quad (8)$$

where the functional relationship is found from the static fan characteristic.

- (b) By applying the steady-state flow continuity equations to the plenum, trunk and cushion cavities (Figure 7).

$$Q_{fx} = Q_{pa} + Q_{pt} + Q_{pc} + Q_v \quad (9)$$

$$Q_{pt} = Q_{tc} + Q_{ta} \quad (10)$$

$$Q_{ca} = Q_{pc} + Q_{tc} \quad (11)$$

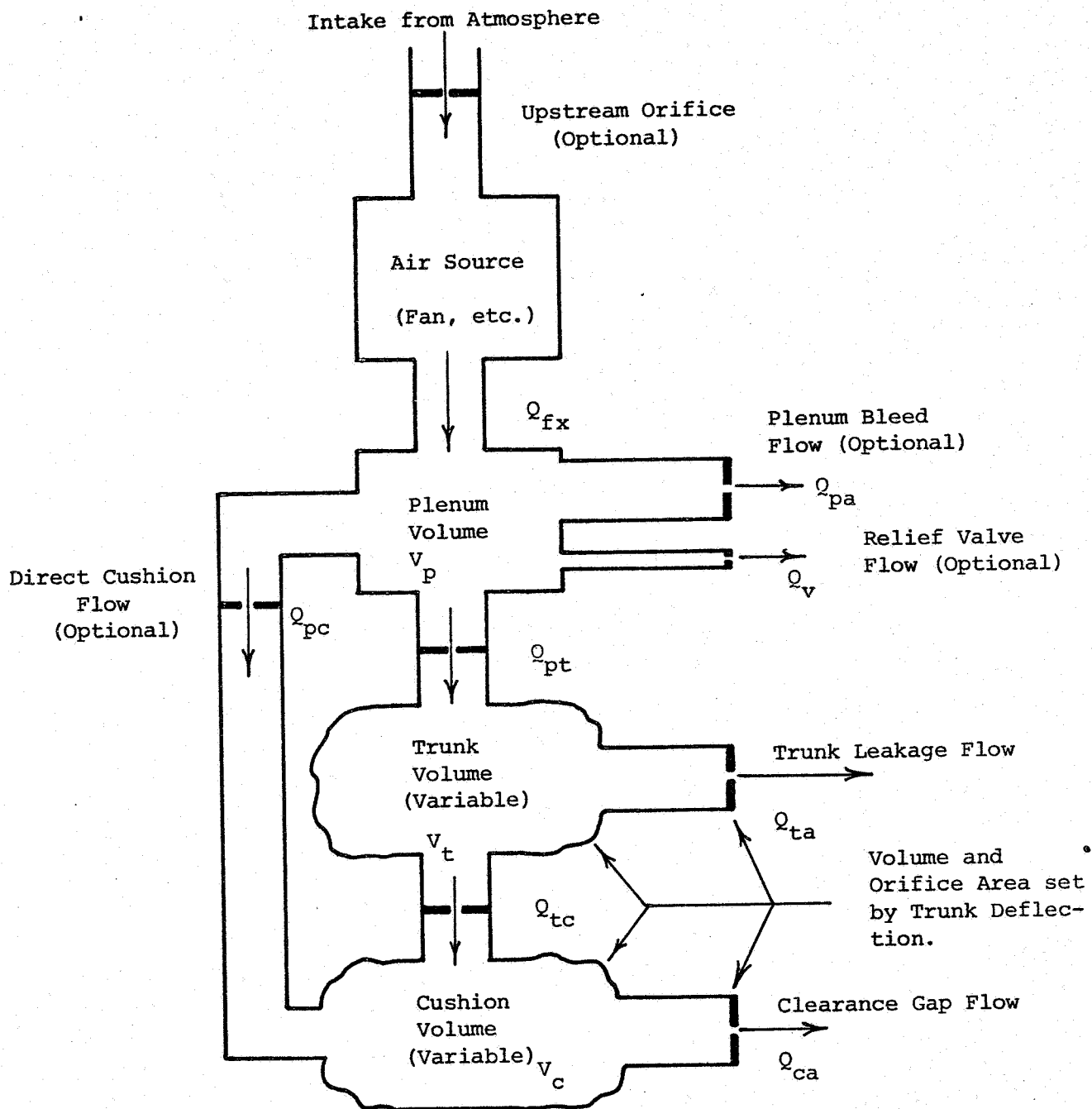


Figure 7. ACLS Flow System

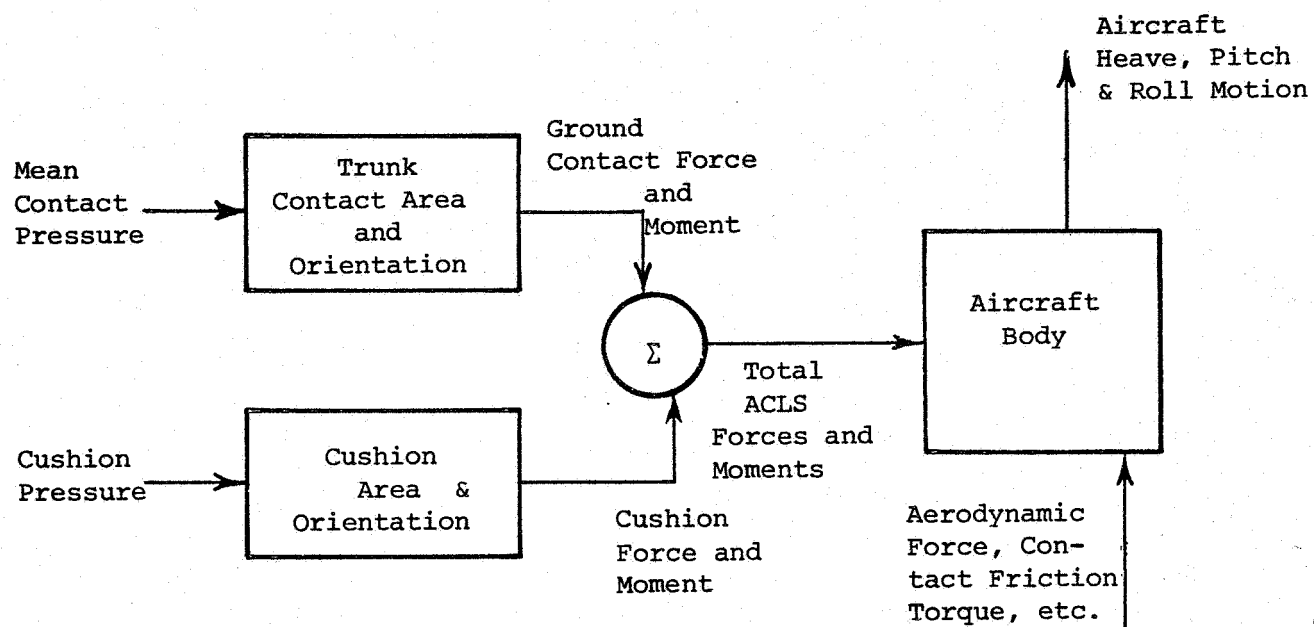


Figure 8. ACLS Force System

- (c) By satisfying the trunk shape constraint for the trunk sides,

$$\left(\frac{H_y}{H_{yi}} \right) = f \left(\frac{P_c}{P_t} \right) \quad (12)$$

where the functional relationship is found from the trunk model described later.

- (d) From static force balance in the vertical direction (Figure 5)

$$M_a g = \left(P_c A_c + P_t A_{cn} \right) \cos \phi_e \cos \theta_e \quad (13)$$

where

M_a	-	aircraft mass
P_c	-	cushion pressure
A_c	-	cushion area
P_t	-	trunk pressure
A_{cn}	-	trunk area in ground contact
ϕ_e	-	Eulerian pitch angle
θ_e	-	Eulerian roll angle
g	-	acceleration of gravity

- (e) From static torque balance in pitch (Figure 5).

$$\left(M_a g \right) C_c = T_{nz} \cos \phi_e \cos \theta_e \quad (14)$$

where T_{nz} is the total cushion and contact pressure torque obtained by adding the torque contributed by each

segment of the finite element trunk and cushion model, and is given by

$$T_{nz} = \sum_{i=1}^{4(M+N)} P_c A_c(i) X_{ch}(i) + P_t A_{cn}(i) X_{tk}(i) \quad (15)$$

- where
- P_c - cushion pressure (gage)
 - P_t - trunk pressure (gage)
 - $A_c(i)$ - cushion area of the i^{th} segment
 - $A_{cn}(i)$ - trunk contact area of the i^{th} segment
 - $X_{ch}(i)$ - x axis distance between the centroid of the i^{th} cushion segment and the geometric center of the cushion
 - $X_{tk}(i)$ - x axis distance between the centroid of the i^{th} trunk contact segment and the geometric center of the cushion
 - $4(M+N)$ - number of segments in cushion and trunk model

(f) From static torque balance in roll (Figure 5)

$$(M_a g) F_f = -T_{nx} \cos \phi_e \cos \theta_e \quad (16)$$

where T_{nx} is the total cushion and contact pressure torque about the vehicle x axis, and is given by

$$T_{nx} = \sum_{i=1}^{4(M+N)} \left[P_c (A_c(i)) (Z_{ch}(i)) + P_t (A_{cn}(i)) (Z_{tk}(i)) \right] \quad (17)$$

where $Z_{ch}(i)$ - z axis distance between the centroid of the i^{th} cushion segment and the geometric center of the cushion

$Z_{tk}(i)$ - z axis distance between the centroid of the i^{th} trunk contact segment and the geometric center of the cushion

and the other symbols are defined in (e) above.

The Dynamic Model

The state equations for the system are derived as follows:

- (a) By satisfying the dynamic fan flow constraint (see "The Fan Model")

$$\frac{dQ_{fx}}{dt} = \frac{P_f + P_{af} - P_p}{I_f} \quad (18)$$

where P_f is the static fan pressure rise for the flow Q_{fx}

P_{af} is the pressure drop across the upstream orifice

P_p is the plenum pressure

and I_f is the fluid inertance of the fan ducts

- (b) By applying the flow continuity equation to the plenum trunk and cushion cavities (Figure 7). The dynamic continuity equation requires that the net inflow into the cavity equals the rate of increase of fluid mass within the cavity.

$$\frac{d}{dt} (\rho V_p) = (Q_{fx} - Q_{pa} - Q_{pt} - Q_{pc} - Q_v) \rho \quad (19)$$

$$\frac{d}{dt} (\rho V_t) = (Q_{pt} - Q_{tc} - Q_{ta}) \rho \quad (20)$$

$$\frac{d}{dt} (\rho V_c) = (Q_{pc} + Q_{tc} - Q_{ca}) \rho \quad (21)$$

- (c) By satisfying the trunk shape constraint for the trunk sides,

$$\left(\frac{H_y}{H_{yi}} \right) = f \left(\frac{P_c}{P_t} \right) \quad (12)$$

- (d) From the dynamic force balance in the vertical direction (Figure 5)

$$\begin{aligned} M_a \ddot{Y}_{cg} &= (F_{cp} + F_{tp} + F_{df} + F_{ct}) \cos \phi_e \cos \theta_e \\ &\quad - M_a g \end{aligned} \quad (22)$$

where

- F_{cp} - cushion pressure force
- F_{tp} - trunk contact pressure force
- F_{df} - aerodynamic drag force
- F_{ct} - trunk damping force

These forces are evaluated as follows:

$$F_{cp} = P_c A_c$$

$$F_{tp} = P_t A_{cn}$$

$$F_{df} = -1/2 C_D A_{ph} \rho \frac{V^3}{|V|}$$

where V is the heave velocity component. (Trunk damping force is evaluated in the trunk model described later.)

- (e) By applying the moment of momentum theorem about the vehicle pitch axis (Eqn (4), with $\dot{\psi} = \ddot{\psi} = 0$ and $T_y = 0$)

$$\ddot{\phi} = I_x \left[T_z - \dot{\theta} (I_{xy} \dot{\theta} + I_{yz} \dot{\phi}) \right] / (I_x I_z - I_{xz}^2) - I_{zx} \left[T_x + \dot{\phi} (I_{xy} \dot{\theta} + I_{yz} \dot{\phi}) \right] / (I_x I_z - I_{xz}^2) \quad (23)$$

where $T_x = T_{cpx} + T_{tpx} + T_{dfx} + T_{tx} \quad (24)$

- T_x - total torque on vehicle x-axis
- T_{cpx} - cushion pressure torque on vehicle x-axis
- T_{tpx} - contact torque on vehicle x-axis
- T_{dfx} - torque due to aerodynamic force on x-axis
- T_{tx} - torque due to trunk damping force on vehicle x-axis

- (f) By applying the moment of momentum theorem about the vehicle roll axis [Eqn (4) with $\dot{\psi} = \ddot{\psi} = 0$ and $T_y = 0$]

$$\ddot{\theta} = I_z \left[T_x + \dot{\phi} (I_{xy} \dot{\theta} + I_{yz} \dot{\phi}) \right] / (I_z I_x - I_{zx}^2) - I_{zx} \left[T_z - \dot{\theta} (I_{xy} \dot{\theta} + I_{yz} \dot{\phi}) \right] / (I_z I_x - I_{zx}^2) \quad (25)$$

where T_z is the total torque on the vehicle z axis whose components are defined analogous to those of T_x in (e) above.

- (g) By carrying out a coordinate transformation and expressing the vehicle frame velocity and acceleration components in terms of Euler angles and their derivatives as discussed earlier.

$$\dot{\theta} = \dot{\psi}_e \sin \phi_e \cos \theta_e + \dot{\theta}_e \cos \phi_e \quad (5)$$

$$\dot{\psi} = \dot{\psi}_e \cos \phi_e \cos \theta_e - \dot{\theta}_e \sin \phi_e \quad (6)$$

$$\dot{\phi} = \dot{\phi}_e - \dot{\psi}_e \sin \theta_e \quad (7)$$

- (h) By applying Newton's Law to the pressure relief valve which is modeled as a second-order mass-spring-dashpot system with preload and nonlinear stops. The valve displacement is given by:

$$m_v \ddot{x}_v + z_v \dot{x}_v + k_v x_v = (P_p - P_{pb}) A_v \quad (26)$$

subject to the constraint that limits valve motion within the range $0 \leq x_v \leq x_a$.

where

m_v	-	relief valve mass
z_v	-	valve damping constant
k_v	-	valve spring stiffness

x_v	- valve motion
P_p	- plenum pressure
P_{pb}	- valve preload pressure (cracking pressure)
A_v	- valve area

The valve outlet diameter and discharge coefficient form external inputs to the model.

Subsystem Models

The Fan Model

Almost all the work in the past has treated the fan as a static element, i.e., as a flow source whose output depends only on the instantaneous value of the backpressure. While this model is adequate for slowly changing pressures, it leads to unrealistically fast flow changes when the ACLS experiences touchdown. Clearly, during touchdown and other rapidly changing conditions, dynamic phenomena that introduce lags in the fan flow response become important, and must therefore be included in the fan model.

There are several levels of fan models that can be developed to characterize dynamic fan flow. In this work, a lumped parameter model has been formulated, which characterizes the fan as a static pressure rise element in series with an inertance and capacitance as shown in Figure 9a. Flow from the atmosphere goes through an inlet orifice and then experiences a pressure rise in the static element as set by the steady-state fan characteristics. In dynamic operation, the flow must also experience a pressure change due to the air mass that has to be accelerated. This is modeled by the stream tube inertance. Finally the compressibility of the air changes the air mass contained in the fan passages, and thus affects

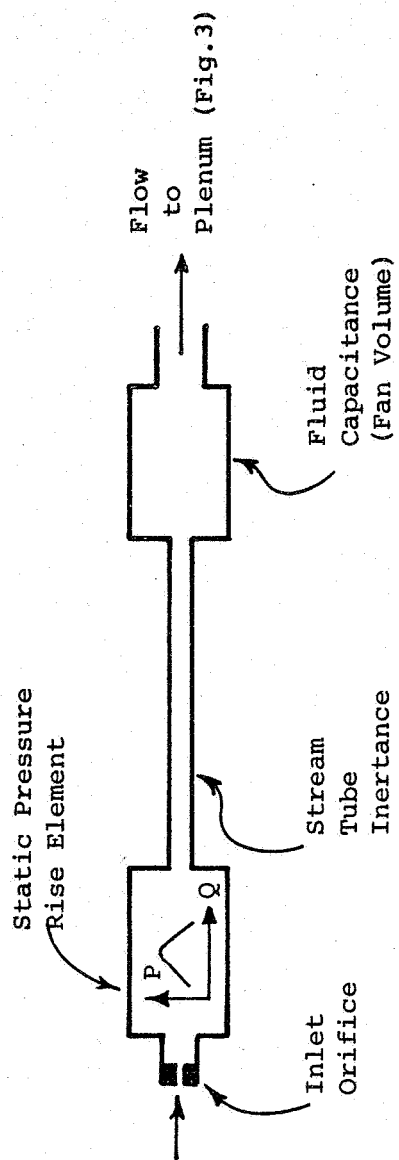
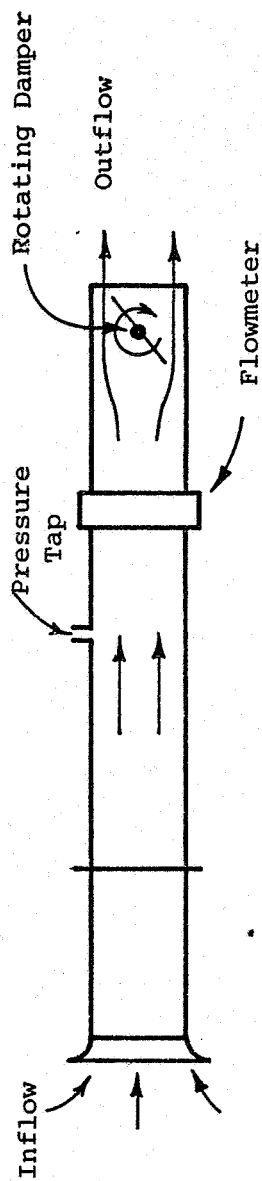
(a) Dynamic Model(b) Test Setup

Figure 9. Fan Model Development

the output flow. This characteristic is modeled by the volume (capacitance) of the fan passages. Thus, during static operation or when the pressure is changing very slowly, the output flow equals that found from the static fan curve. However, when the pressure changes suddenly, the air mass and compressibility introduce lags in the system and prevent instantaneous flow changes from taking place.

Two simplifications that can be carried out with this model are to add the fan volume (capacitance) to the plenum volume, and to increase the stream tube inertance to take into account any long ducts connecting the fan to the cushion. With these changes, the fan flow into the plenum is given by

$$I_f \left(\frac{dQ_{fx}}{dt} \right) = P_{af} + P_f + P_p \quad (18)$$

where Q_{fx} is the fan flow
 P_{af} is the pressure drop across the upstream orifice
 P_f is the static fan pressure rise
 P_p is the plenum pressure
 and I_f is the inertance of the fan and connecting ducts.

The drop across the upstream orifice (if present) is given by the conventional orifice flow equation

$$P_{af} = \rho \left(Q_{fx} / A_u C_{du} \right)^2 / 2 \quad (27)$$

where A_u is the orifice area
 ρ is the air density
 and C_{du} is the discharge coefficient

The static pressure rise P_f is found from the fan curve, which can be represented analytically by a polynomial fit of the form

$$Q_{fx} = \alpha_0 + \alpha_1 P_f + \alpha_2 P_f^2 + \alpha_3 P_f^3 + \alpha_4 P_f^4 \quad (28)$$

The inertance I_f is given by

$$I_f = \rho \left(\frac{\ell_{df}}{A_{df}} + \frac{\ell_{dd}}{A_{dd}} \right) \quad (29)$$

where ℓ_{df} and ℓ_{dd} are the lengths of the fan flow passages and the fan-to-plenum duct respectively, and A_{df} and A_{dd} are their corresponding cross-sectional areas.

The above model is set up so that it can represent a variety of fans by using the appropriate characteristic for the static pressure rise. No other test data or empirical relationships are needed to quantify the model, because the inertance (and capacitance) are determined exclusively from fan geometry.

In parallel with the analytical development, dynamic fan tests were carried out by NASA on a $1 \text{ m}^3/\text{s}$ (2000 cfm) 5 kPa (100 psf) Joy axial flow fan (ref. 35). This fan was chosen because it powers the prototype cushion subsequently tested to verify the complete model. The test setup is shown in Figure 9b. It consists of the fan attached to a duct with a rotating damper (variable orifice) at the other end. A pressure tap and flowmeter are included to measure

the dynamic pressure-flow characteristic as the damper rotates at various speeds. Figure 10 shows the test data obtained when the damper opening was changed in increments. The high scatter in the left half of the curve occurs because flow stability in this region is low, and pressure surges do not readily damp out. The test characteristic however is essentially the same as that obtained from the manufacturer. The figure also shows the polynomial fit (Eqn (28)) used to characterize the static element of the model. The negative flow characteristic was estimated by determining the cross-sectional area of the flow passages and assuming that during pressure reversal the fan passages behave as orifices with a linear pressure drop characteristic. Figure 11a shows the results as the damper is rotated continuously at various speeds. The solid line represents damper closing and the broken line damper opening. Perturbation frequencies (which correspond to twice the damper speed) of 1 Hz and 5 Hz were used because they lie within the normal range of ACLS operation. The curves show a departure from the static characteristics, particularly at the higher frequency. The fan outlet pressure now depends both on the magnitude of the flow and its sense (i.e., increasing or decreasing). Increasing flows result in a lower pressure rise than decreasing flows because in the former case, part of the static pressure rise is taken up in accelerating the air mass in the fan passages, while in the latter case, the air mass is being decelerated, and so gives up its kinetic energy to increase the pressure rise. Previous fan models have been unable to account for this behavior. The model developed here overcomes this drawback. Simulation results using actual values of inertance and capacitance (as found from the fan and test fixture drawings) are shown in Figure 11b.

As can be seen, the model predicts the right trends, and should therefore result in an improved simulation of touchdown and other rapidly changing situations.

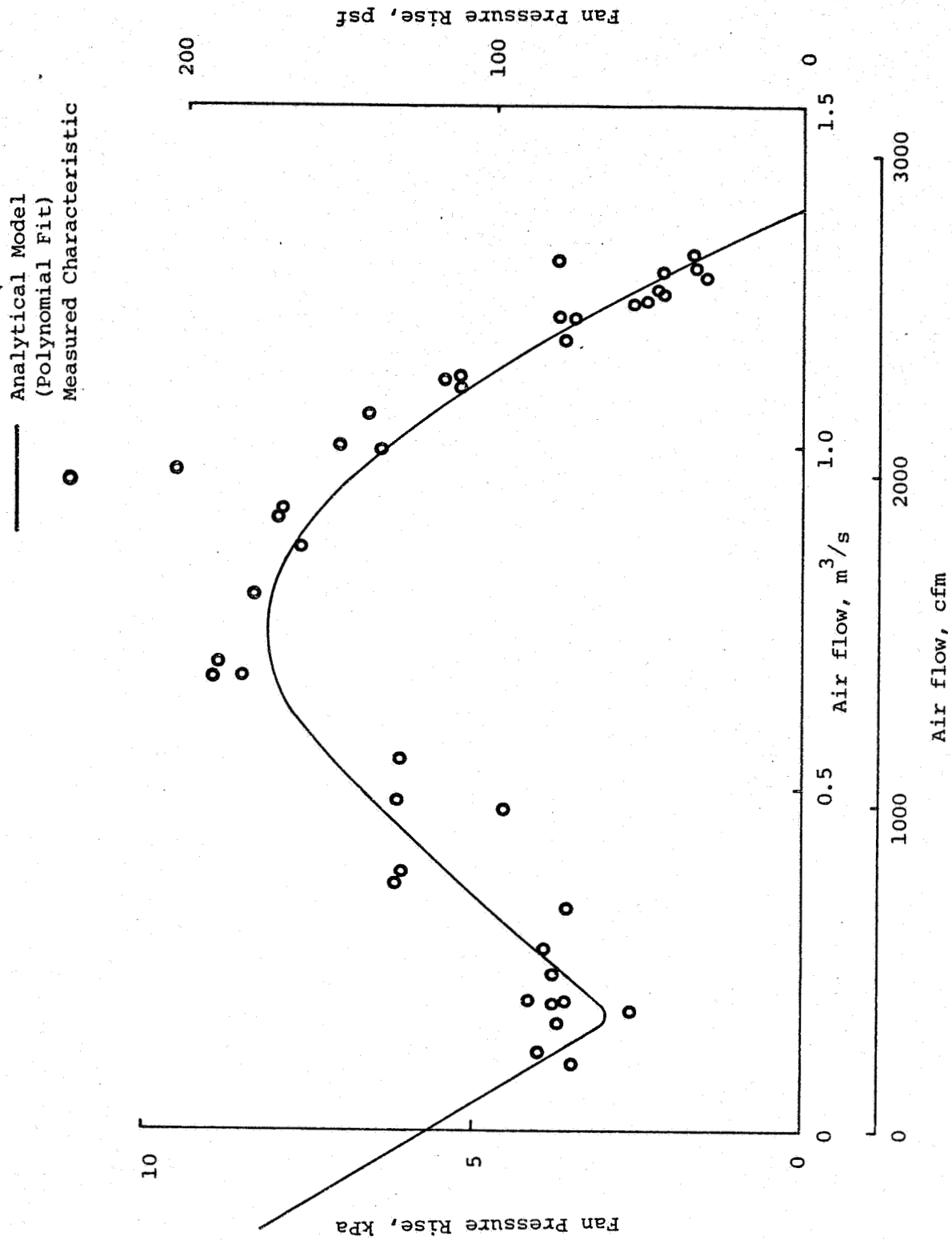


Figure 10. Static Fan Curve -- Measurement and Analytical Model

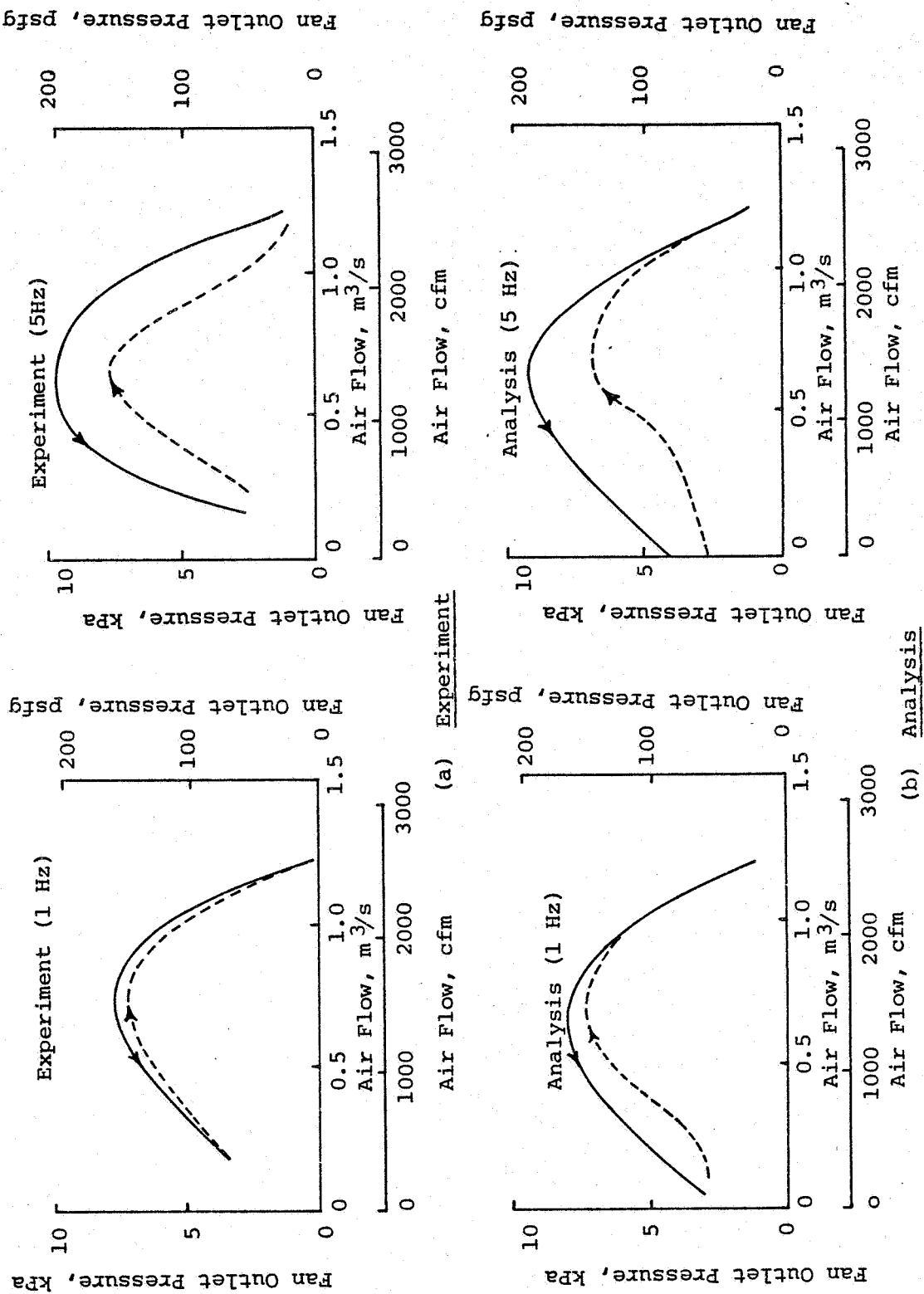


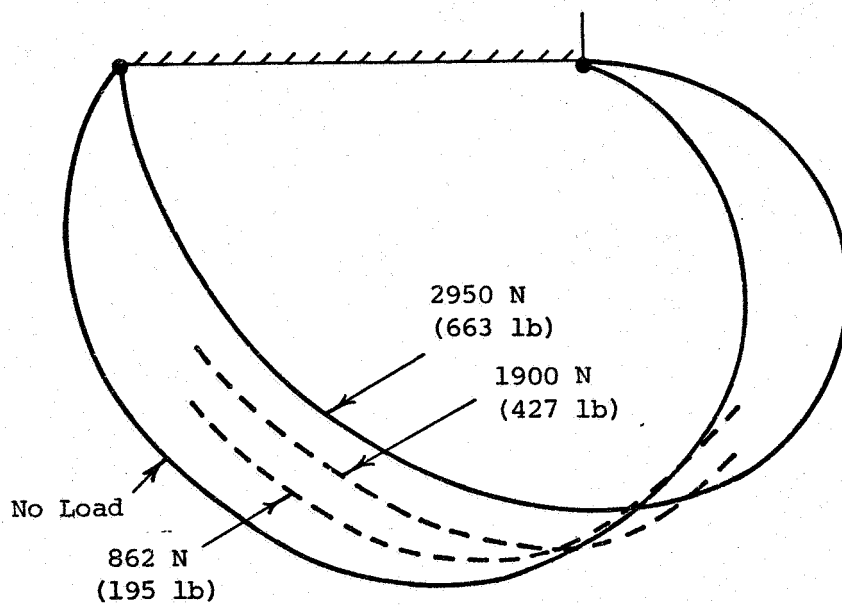
Figure 11. Comparison of Fan Analysis with Experiment

The Trunk Model

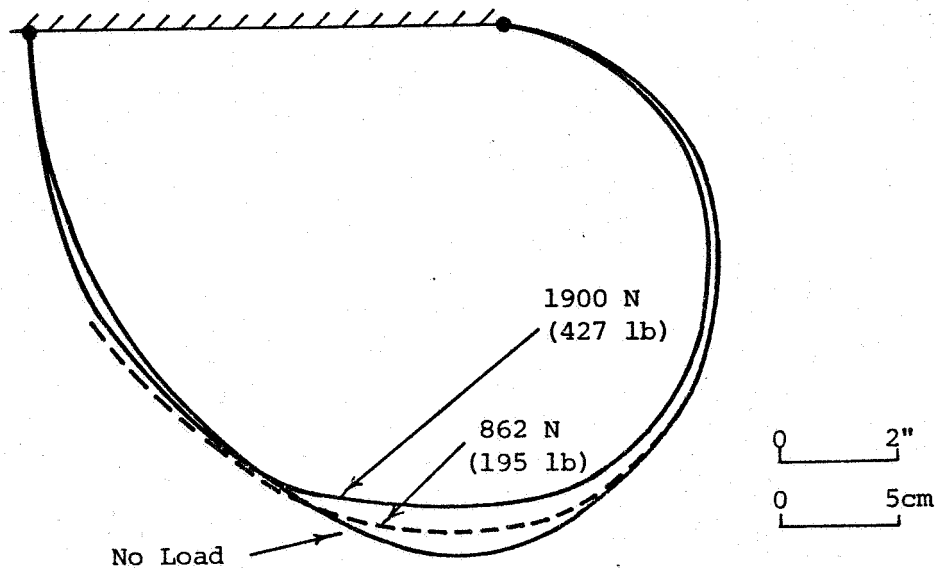
The trunk model determines the trunk shape parameters (volume, and orifice and contact areas), contact pressure distribution and damping that form inputs to the ACLS flow and force systems.

Trunk Shape. - In past work, two analytical models have been developed for the trunk shape: The Membrane Trunk Model (ref. 11) and the Frozen Trunk Model (ref. 26). (The model of Coles is essentially a membrane model.) The shortcoming of both these analyses was that they modeled the side and end segments of the trunk in the same way while test data now confirm that the shorter curved end segments (front and rear) behave very differently from the longer, straight side segments. Figure 12 shows the trunk cross section measured at the center of the side and end segments as the load on the cushion is increased. The entire side segment tends to bow outward and avoid ground contact, while the end segment remains virtually fixed, except for a flattening in the region that actually touches the ground. This difference in behavior occurs because the front segment is much smaller than the side segment and is curved. When the cushion pressure increases due to an increase in the load, the radially outward force causes the oval trunk planform to become more circular, as shown in Figure 13. This causes a hoop tension force T to act around the trunk periphery. In the side segments, this force acts substantially normal to the side excursion δ_s so that its component resisting the motion is negligible and the side segment can thus bow outwards relatively unrestrained. In the end segments the situation is different, since the curvature of the segment causes the hoop tension to have a much higher component opposing the motion, so that outward motion of the trunk ends is very much smaller.

Since hoop tension has very little effect on side trunk motion, the side segments can be considered as simple two-dimensional membranes, as done in the Membrane Trunk Model. On the other



(a) Side Segment



(b) End Segment

Figure 12. Measured Trunk Profile

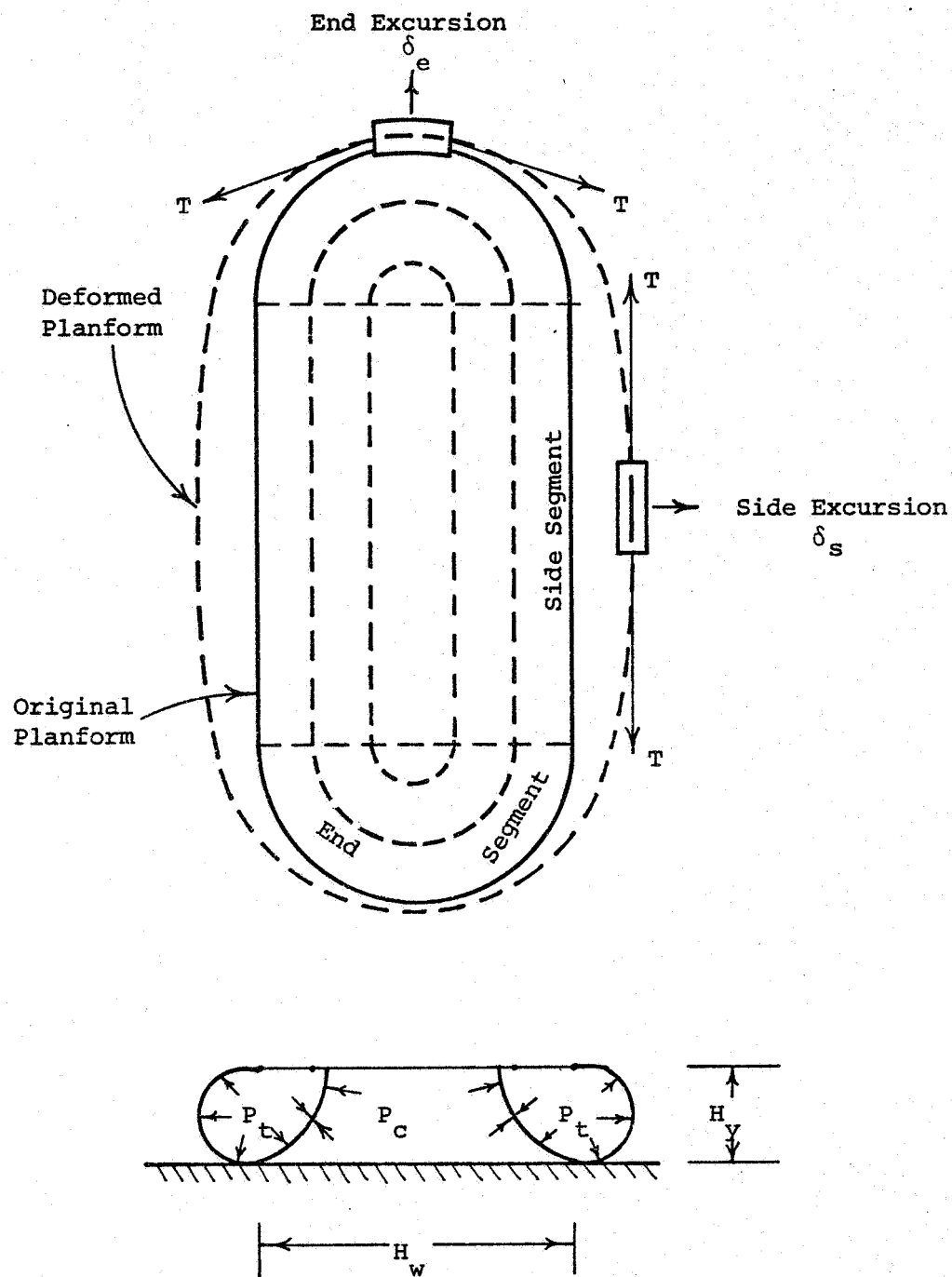


Figure 13. Outward Excursion of Trunk Segments

hand, the fact that hoop tension restrains ("freezes") the trunk ends suggests that these segments be modeled by the Frozen Trunk Model: Thus the logical step in trunk model improvement is to combine the two existing models and form the Hybrid Trunk Model, in which the sides are represented by the Membrane Model and the ends by the Frozen Model.

In static heave operation, as the load on the cushion increases, the trunk ends contact the ground while the sides bulge outwards (as shown in Figure 12) to maintain the cushion air gap that allows the inflow from the trunk to exhaust to the atmosphere. The amount of side trunk bulge (and hence cushion-to-atmosphere air gap) adjusts itself such that the resulting cushion pressure and cushion-to-trunk pressure ratio satisfies the conditions for free (non-contacting) trunk membrane equilibrium and cushion flow continuity. In dynamic operation (or in static pitch and roll) a situation can exist when the ground clearance is too small for the free trunk membrane equilibrium conditions to be satisfied. In this situation, the trunk must touch the ground and flatten. When modeling this case, only the trunk in the contact zone is considered to deform, since trunk-ground friction will tend to prevent lateral trunk movement.

The Hybrid Trunk Model is essentially a limiting case analysis of trunk deflection. In general, best results will be obtained at the middle of the respective segments, i.e., at the center of the side segments, where the trunk behaves very much like an ideal membrane, and at the center of the end segments, where the trunk shape is truly fixed. In the transition region (at and near where the segments meet) the trunk will behave somewhere between the membrane and frozen trunk approximations. Although an additional refinement to model the transition region could be developed, it is appropriate first to check the results obtained with the basic hybrid model, to see whether transition effects are in fact important. With this view in mind the overall cushion geometry (height H_y and width H_w) as predicted by the Hybrid Trunk Model has been

compared with test data obtained with the prototype cushion. The results are shown in Figure 14 as a function of the cushion-to-trunk pressure ratio P_c/P_t . As the pressure ratio increases, corresponding to an increased load, the cushion height (which is practically equal to the trunk height) reduces, because the side trunk lobes move outward, and the end trunk is flattened. When the side lobes move out, the cushion width, which is the distance between the lowest points on the side trunk segments, increases. Because the end trunk is restrained from moving outwards, the cushion length remains virtually unchanged. Since the Hybrid Trunk Model predicts the actual cushion height and width within 10 percent, there is little justification at this point for including transition region effects in the model.

Contact Pressure. - In addition to trunk and cushion shape the trunk model also determines the pressure distribution in the ground contact zone. The analysis for pressure distribution is complicated by the fact that two separate effects must be considered: direct trunk-ground contact caused by the trunk pressure forcing the trunk against the ground, and airflow through the trunk holes into the interstices that remain in the contact zone. These two effects are first discussed separately and then combined into a single model for trunk contact pressure.

When two bodies in contact are acted upon by a force F , the actual contact occurs at a number of discrete regions rather than over the whole area, due to the inherent roughness of the contacting surfaces. This is illustrated in Figure 15a where the actual contact regions (area $A_1, A_2 \dots A_n$) are spread over the nominal contact area A . The actual pressure distribution (Figure 15b) shows high pressure peaks $P_1, P_2 \dots P_n$ in the contact regions and no pressure in the voids. Because the number of contact regions is large, it is conventional for purposes of a force balance to define an average contact pressure $P_{av} = F/A$ acting as though the bodies were touching uniformly over the entire area A , as shown

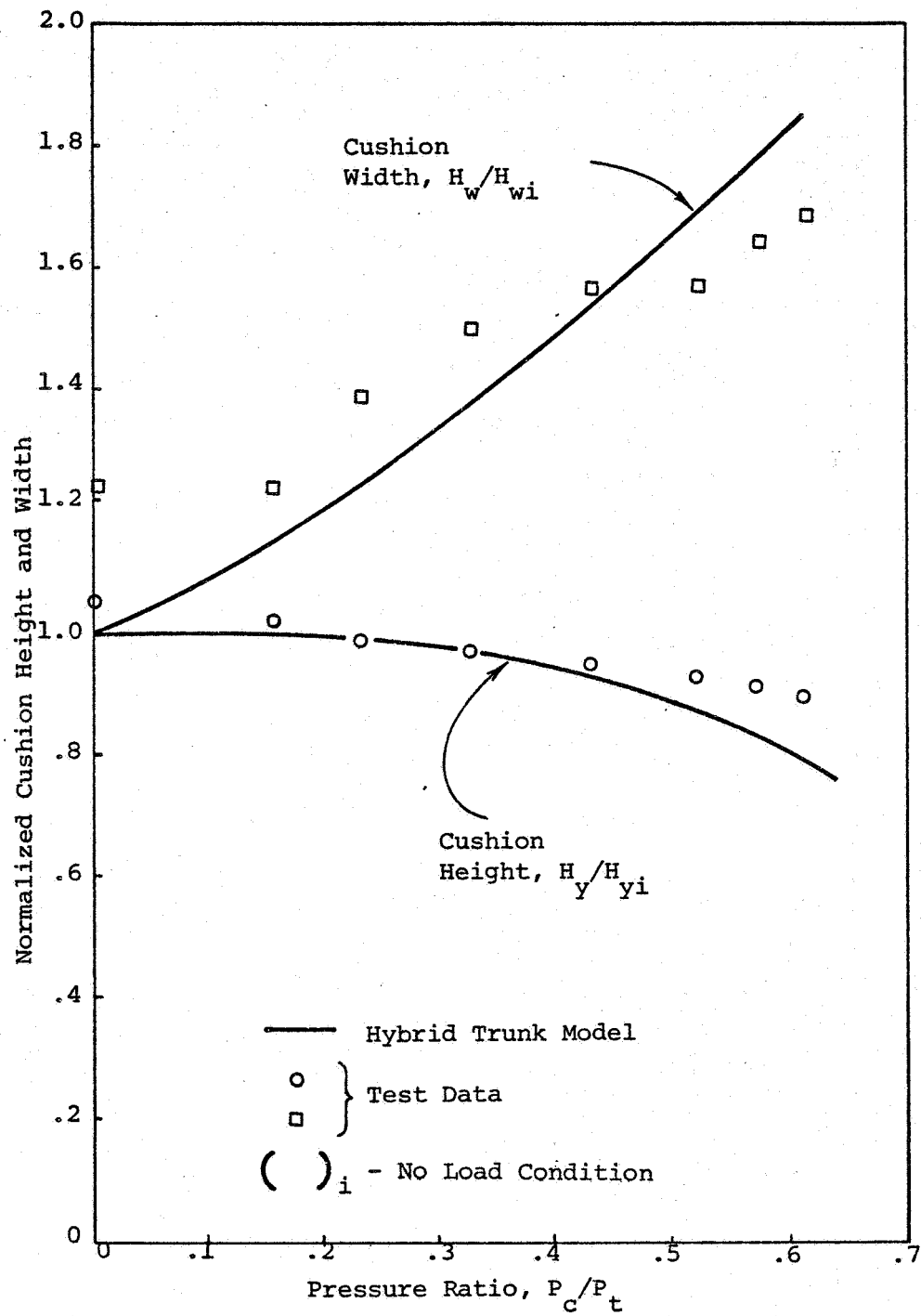


Figure 14. Trunk Model Evaluation - Cushion Height and Width

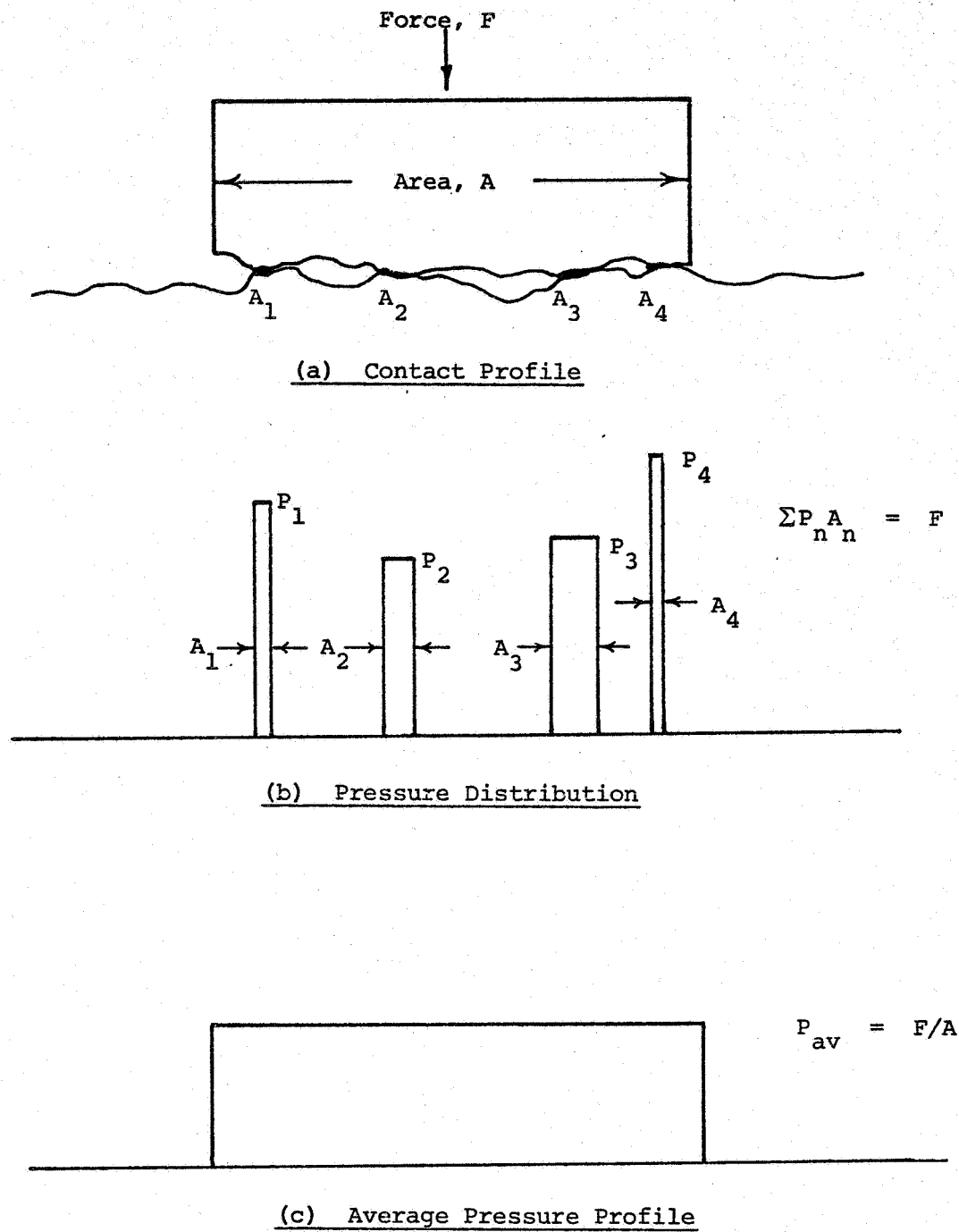
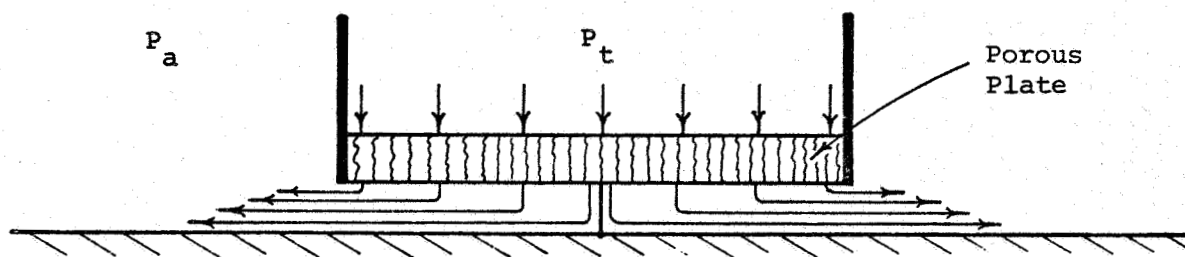


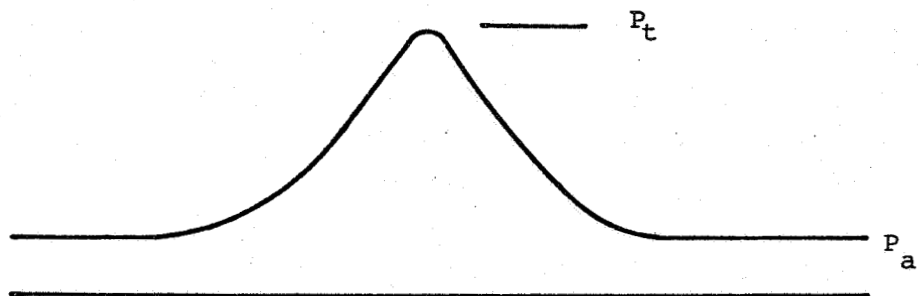
Figure 15. Pressure Distribution between Bodies in Contact

in Figure 15c. In the event however that one of the bodies is porous, flow seepage can still take place through the voids in the contact zone, although of course as the average contact pressure increases, the void region and hence the flow will decrease. To help model this flow phenomenon, consider the flow through a porous plate held close to, but not touching the ground, as shown in Figure 16a. By symmetry, there is a stagnation point at the center in which the pressure rises to its original value P_t . Moving away from the center, the pressure decreases continuously until it reaches the ambient pressure P_a at the edges of the plate, as shown in Figure 16b. Thus the driving pressure for flow through the plate at any point is given by the difference between the upstream pressure P_t and the pressure in the gap at that point.

For a trunk in ground contact, both discrete contact regions and flow through the voids will exist, and a combined force/flow model as shown in Figure 17 will be required. This model combines the features of the discrete contact and porous plate models described above. The pressure distribution under the trunk in the ground contact zone is assumed to be made up of two components: discrete pressure peaks where actual trunk-ground contact takes place, and a continuous pressure profile caused by trunk outflow through the voids. The assumed profile is shown in Figure 17b. For purposes of the force balance, a mean contact pressure acting over the nominal contact area can be defined as shown. This mean pressure, which is actually the integrated value of the pressure profile (including peaks), can be found very simply by considering the equilibrium of a flat segment of trunk in nominal ground contact (Figure 18). Isolating a short segment of trunk (area dA), the mean ground pressure is found to equal the trunk pressure, since any force T in the trunk itself cannot have a component in the vertical direction. Of course, at the very edge of the contact zone, the change in trunk angle will introduce other terms in

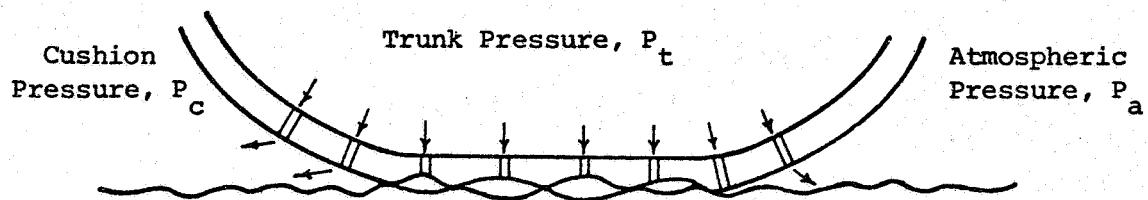


(a) Flow Geometry

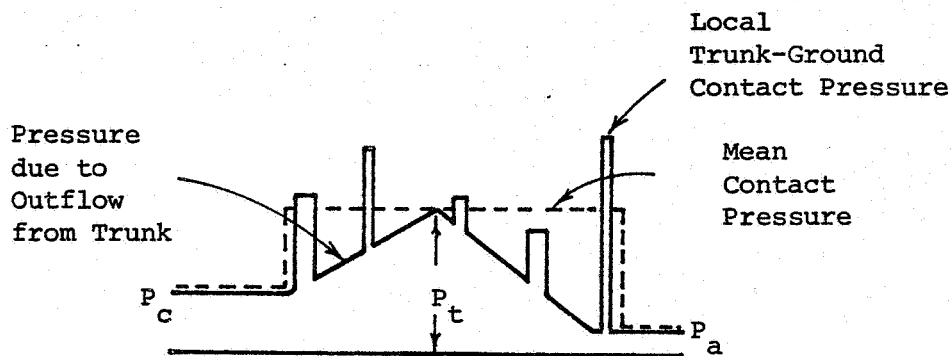


(b) Pressure Profile

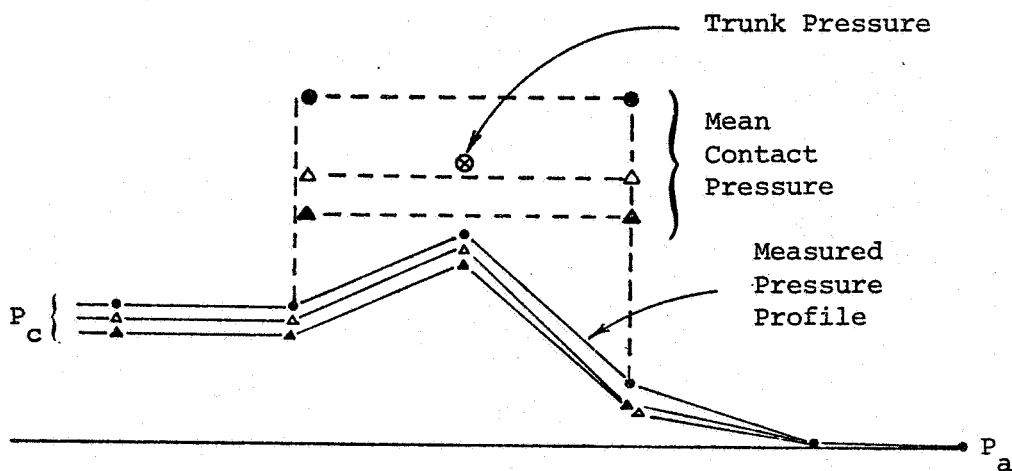
Figure 16. Flow through Porous Plate



(a) Contact Geometry

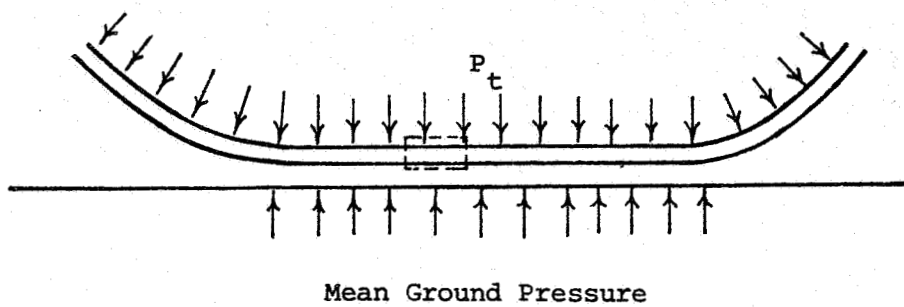


(b) Theoretical Pressure Profile

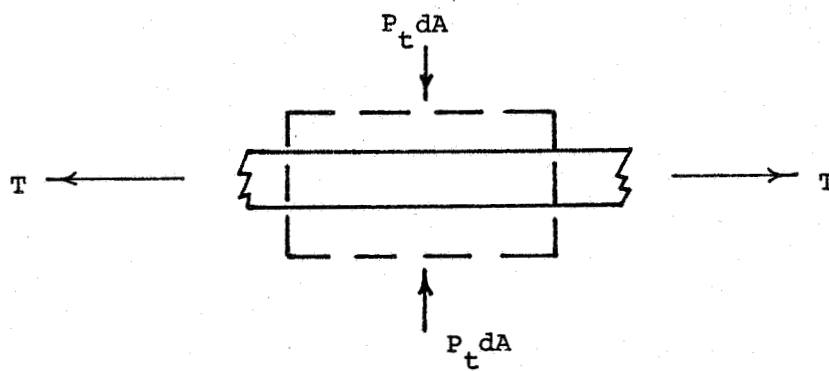


(c) Observed Pressure Distribution

Figure 17. Pressure Distribution in Trunk Contact Zone



(a) Configuration



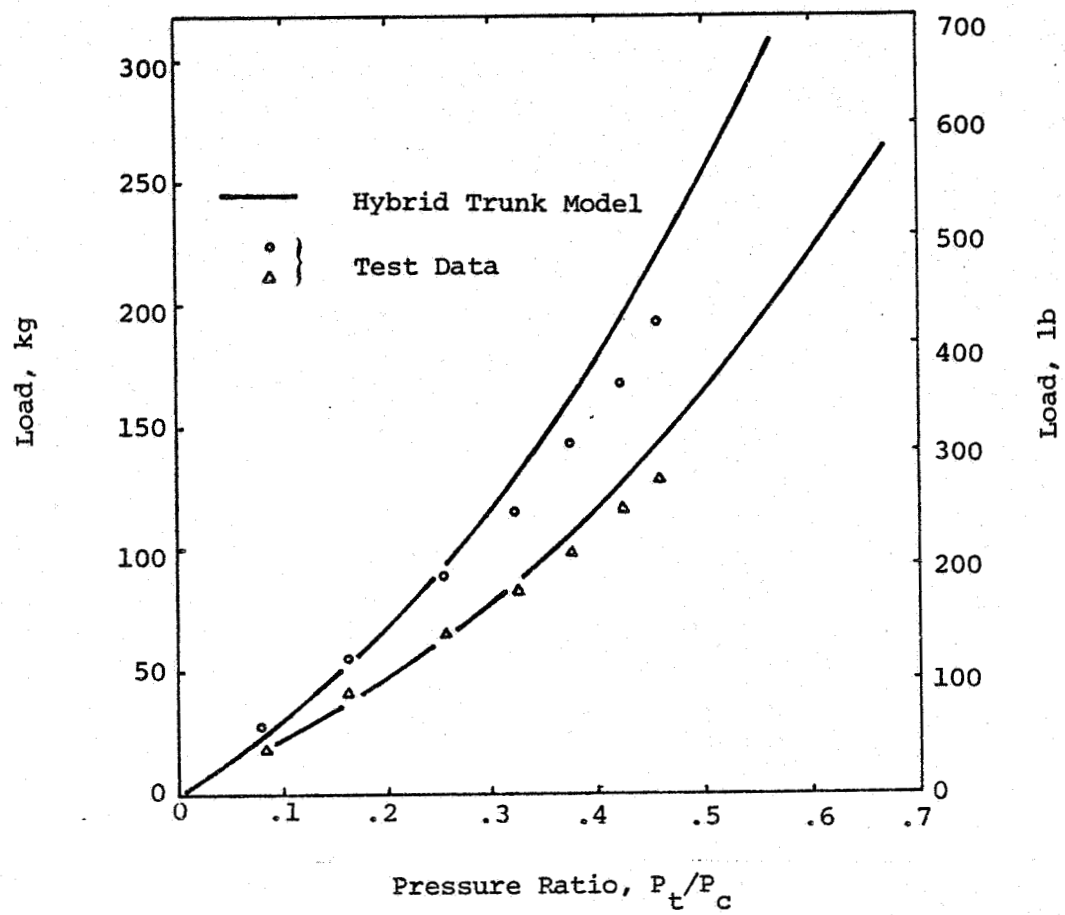
(b) Free Body Equilibrium

Figure 18. Trunk Element Force Balance

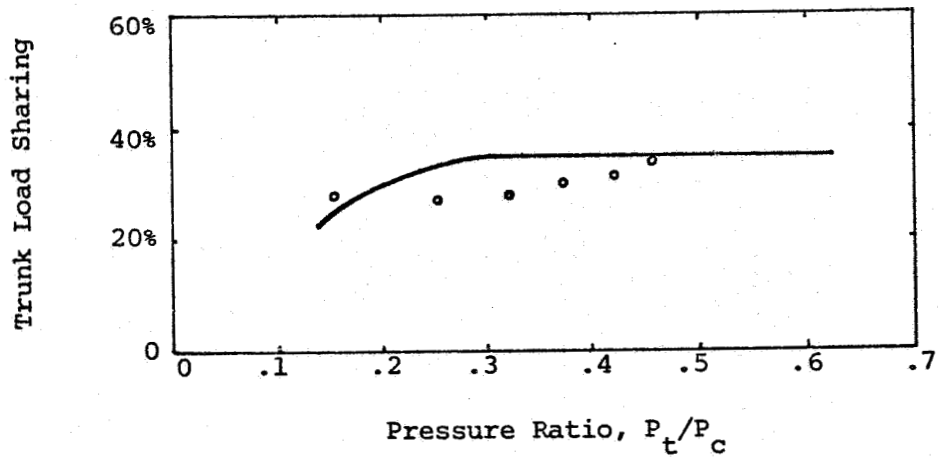
the force balance, but, since this is a localized effect, its influence on the mean pressure distribution is negligible. Thus, in Figure 17b the mean contact pressure is shown equal to the trunk pressure, so that the contact force on the trunk is given by the product of the trunk pressure and the nominal contact area.

For purposes of trunk outflow calculation, the pressure profile in the non-contacting regions is approximated by a linearly decreasing relationship as shown in Figure 17b. The driving pressure for flow through any trunk hole is thus given by the difference between the trunk pressure and the gap pressure at that location.

As a check of the above hypothesis, tests were carried out to measure the base pressure distribution and reaction force of the trunk in ground contact. The observed pressure profile, measured with manometers at various points in the contact zone, is shown in Figure 17c for different loads. Since the manometers only measure the fluid pressure and not the local contact pressure, only the outflow pressure component is observed. As predicted by the theory, this component rises from the cushion pressure at the inner edge, to a maximum at the center of the contact zone and then drops down to ambient pressure at the outer edge of the contact zone. The mean pressure, also shown in Figure 17c, has been found by dividing the load supported by the trunk by the nominal contact area. The trunk load contribution was obtained by taking the total load and subtracting the cushion load component found from the product of the measured cushion pressure and area. As a final check, the load supported by the trunk and cushion as a function of the cushion-to-trunk pressure ratio is shown in Figure 19. The results comparing the Hybrid Trunk Model with test data show that the theory predicts the actual loads and load sharing between the trunk and cushion quite accurately (within about 10 percent), so that the contact pressure distribution model does not need further refinement at this time.



(a) Total Load



(b) Trunk Load Sharing

Figure 19. Trunk Model Evaluation -- Total Load and Load Sharing

Trunk Damping. - In dynamic operation, the trunk is deformed cyclically both in tension and flexure, and energy dissipation in the trunk material gives rise to a damping force which opposes the strain rate. Because the present trunk analysis does not solve for strain (and hence strain rate), a damping model that links trunk material properties directly to trunk damping forces cannot be developed. An alternate approach, in which the damping characteristics are modeled by dimensional analysis (similarity) based on test data thus appears more appropriate. In keeping with the method of approach outlined earlier, the trunk is divided into segments (Figure 20) and a series of dashpots -- one for each segment -- is included in the model such that the segment damping force F_{ct} is proportional to the vertical velocity V_t of the trunk segment.

Each dashpot B_e models the energy dissipation characteristic of the trunk segment. Although all parts of the trunk dissipate energy, the major contributions will come from those parts that undergo high stress reversals, since the strain rate is highest in these sections. Observations of a trunk in dynamic operation suggest that the high stress reversal regions lie along the periphery of the trunk-ground contact zone, because it is here that the rate of change of trunk slope (and hence stress) is high and constantly changing with the time as the contact area changes. As a first order approximation, the damping model derived here assumes that all the energy dissipation in the trunk is concentrated along the trunk-ground contact periphery so that the damping coefficient of each dashpot B_e depends on the perimeter of the ground contact zone. This means that when a segment is not contacting the ground it has zero damping, and when it is contacting the ground it has a damping coefficient proportional to the contact perimeter. Thus, the damping coefficient of the dashpot associated with the i^{th} trunk segment is

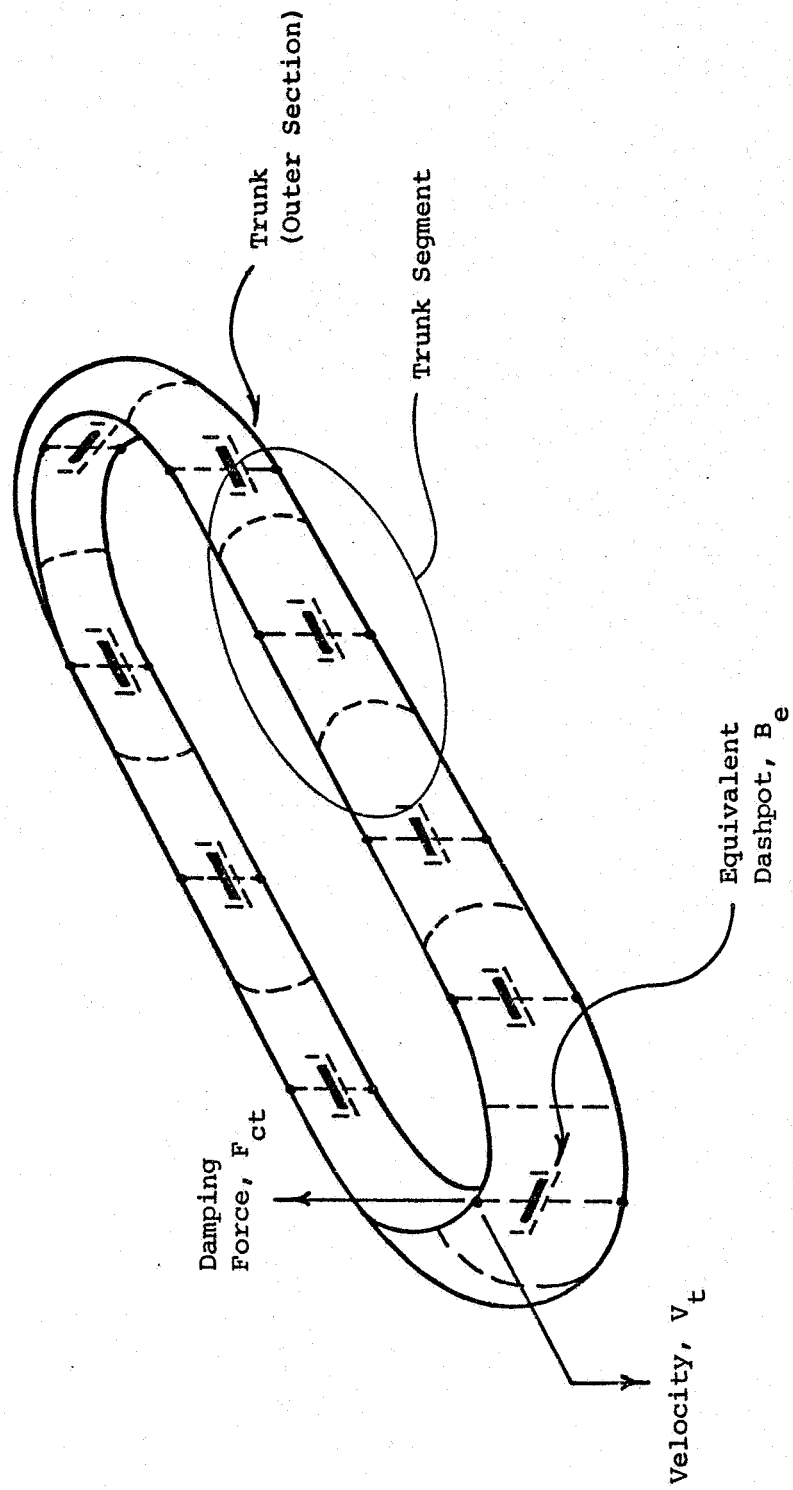


Figure 20. The Trunk Damping Model

$$B_e(i) = D_c \ell_c(i) \quad (30)$$

where D_c is a characteristic damping constant for the trunk,

and $\ell_c(i)$ is the perimeter of the ground contact zone for the i^{th} segment.

The value of the damping constant D_c will depend primarily on the material properties of the trunk, and correlation of existing test data will provide an estimate of its value for the various types of trunks of interest. Although, at present, only limited data is available, the values of D_c thus far obtained (see subsequent section on Parameter Evaluation) provide an initial guide to the selection of this parameter.

The damping forces and torques required to evaluate Eqns (22), (23) and (25) are given by

$$F_{ct} = - \sum_i B_e(i) V_t(i) \quad (31)$$

$$T_{tx} = - \sum_i B_e(i) V_t(i) X_{cx}(i) \quad (32)$$

$$T_{tz} = - \sum_i B_e(i) V_t(i) Z_{cx}(i) \quad (33)$$

where X_{cx} and Z_{cx} are the moment arms in pitch and roll, and the minus sign is included because damping forces and torques oppose the velocity.

Model Synopsis

The Flow System (Figure 7)

- (a) The fan is characterized by a static pressure rise element for forward and back flow in series with an inertance (duct) and a capacitance (volume).
- (b) The trunk and cushion volume are found from the Hybrid Trunk Model, which characterizes the side trunk segment as an ideal two-dimensional membrane and the end segment as a "frozen" trunk.
- (c) The orifice areas between the trunk and cushion, trunk and atmosphere and cushion and atmosphere are found from the trunk shape as predicted by the Hybrid Trunk Model, along with the cushion orientation and ground profile.
- (d) The pressure within the cushion, trunk and plenum is considered to be uniform.
- (e) The pressure in the trunk/ground contact zone is found from the triangular profile given by the Hybrid Trunk Model.
- (f) The flow through the plenum, trunk and cushion is governed by the unsteady state flow continuity equation in which the air is assumed to behave like a perfect gas and follow a polytropic expansion relationship.
- (g) The flow through all orifices is found from the incompressible flow square-law orifice equation.
- (h) The pressure relief valve is modeled as a second order mass-spring-dashpot system with nonlinear stops.

The Force System (Figure 8)

- (a) The mean contact pressure in the trunk/ground contact zone is equal to the trunk pressure.
- (b) The trunk contact area and location relative to the aircraft CG is found from the trunk shape predicted by the Hybrid Trunk Model.
- (c) The cushion area and location relative to the aircraft CG is found from the Hybrid Trunk Model. In width, the cushion extends between the lowest (ground tangent) points of the side trunk segments. In length, it extends between the ground tangent points of the end trunk segments, or, if in ground contact, between the inner edges of the contact zone.
- (d) The total forces and moments acting on the aircraft occur due to the mean trunk contact pressure acting over the contact area, the cushion pressure acting over the cushion area, aerodynamic drag and trunk damping losses caused by aircraft heave motion, and trunk-ground friction.
- (e) The forces and moments are found by dividing the cushion (and trunk) into segments, approximating the actual ground profile underneath the cushion by a similar set of segments parallel to the cushion, computing the cushion and contact pressure forces and moments for each segment, and then summing them to determine the total force and moment about the aircraft CG.
- (f) The heave motion of the aircraft is found by applying Newton's law in the vertical direction to the aircraft CG.

- (g) Angular accelerations in pitch and roll are obtained by applying the theorem of moment of momentum about the aircraft pitch and roll axes.
- (h) A coordinate transformation is carried out to express vehicle frame velocities and accelerations in terms of Euler angles and their derivatives.
- (i) The moment of momentum equations, expressed in terms of Euler angles are integrated to give the angular position of the aircraft as a function of time.

TESTING

Test Objectives and Plan

The object of the testing was to obtain data on the operation of a prototype cushion to help develop and verify the analytical model. To minimize hardware costs, it was decided at the outset to use an existing cushion available from NASA rather than build a new one. The test prototype selected was a unit built by Boeing under an earlier Navy contract. The main reasons for choosing this cushion for detailed study were that it was of a size suitable for laboratory testing, and had a very uniform molded plastic trunk free of seams, stitching or other anomalies.

A test plan was drawn up with the following objectives in mind.

1. Parameter Evaluation

- Trunk orifice discharge coefficient
- Trunk damping constant

2. Subsystem Model Development

- Trunk shape in the side and end segments
- Mean trunk-ground contact pressure and pressure distribution

3. Overall Model Verification

- Static heave, pitch and roll stiffness
- Peak values of pressures, displacement and acceleration in dynamic operation

The test plan is summarized in Table III.* The tests included static tests, heave drop tests and pitch and roll moment release tests. The static tests provided key steady-state data, such as contact pressure distribution and trunk shape, needed to develop the trunk model. The dynamic tests provided time histories and peak values of pressures, displacement and acceleration which were used to verify the overall ACLS analysis. A key feature of the tests is that the modes are excited independently, so that coupling effects do not obscure the basic natural mode characteristics. A test rig was designed to carry out this plan by locking out various modes and thus allowing the cushion to be tested in pure heave, pitch and roll independently. A view of the test rig is shown in Figure 21. Details of the test hardware are given in the section that follows.

*The test parameters are actual test values.

TABLE III

THE TEST PLAN

Test Description			Cushion Orientation			Variables Measured										Test Loading	
No.	Type	Mode				Pressure			Displacement		Acceleration			Trunk Shape	Base Pressure Profile		
			CG Height	Pitch Angle	Roll Angle	Fan Inlet	Plenum	Trunk	Cushion	Vertical	Pitch Angle	Roll Angle	Vertical	Angular Pitch	Angular Roll		
<u>Static Tests</u>																	
1.1	Static Heave	Pure Heave		0°	0°	x	x	x	x	x						x	0 - 2960 N (0-663 lbs.)
1.2	Static Pitch	Pure Pitch	.402m (1.32')		0°	x	x	x	x		x					x	0 - 361 N.m (0-265 ft-lbs.)
1.3	Static Roll	Pure Roll	.402m (1.32')	0°		x	x	x	x			x				x	0-132 N.m (0-97 ft-lbs.)
<u>Dynamic Tests</u>																	
2.1	Heave Drop	Pure Heave		0°	0°	x	x	x	x	x			x				Release from 2.5 cm (1") to 30.6cm(12")
2.2	Pitch Release	Pure Pitch	.402m (1.32')	4.5°	0°	x	x	x	x		x			x			Release from 10.5 mr - 62.7 mr (0.6 - 3.6°)
2.3	Roll Release	Pure Roll	.396m .402m .408m	0°		x	x	x	x			x			x		Release from 10.5 mr - 87 mr (0.6° - 5.0°)
2.4	Startup Test	Coupled Heave-Pitch			0°	x	x	x	x	x	x						Startup from ground zero

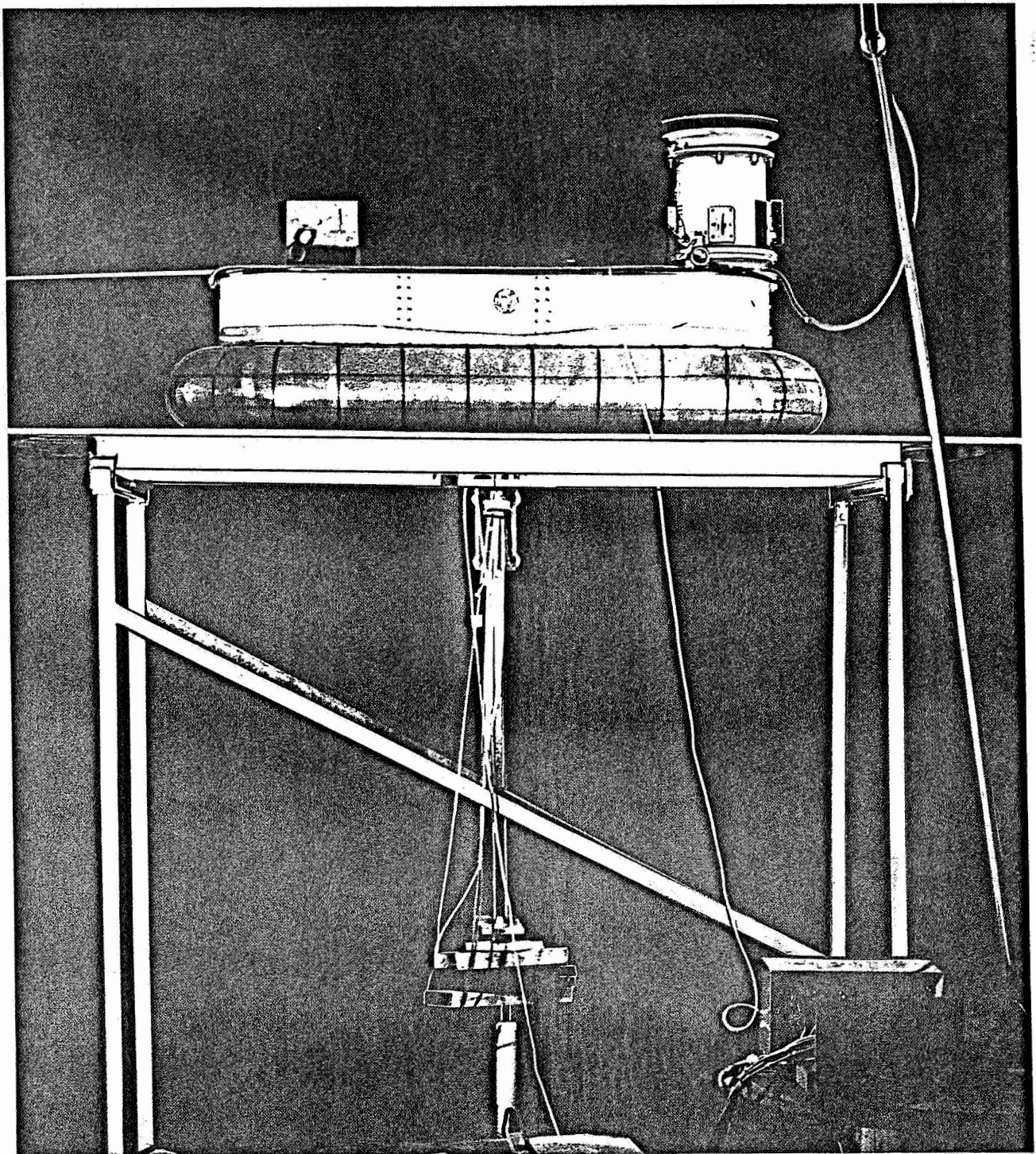


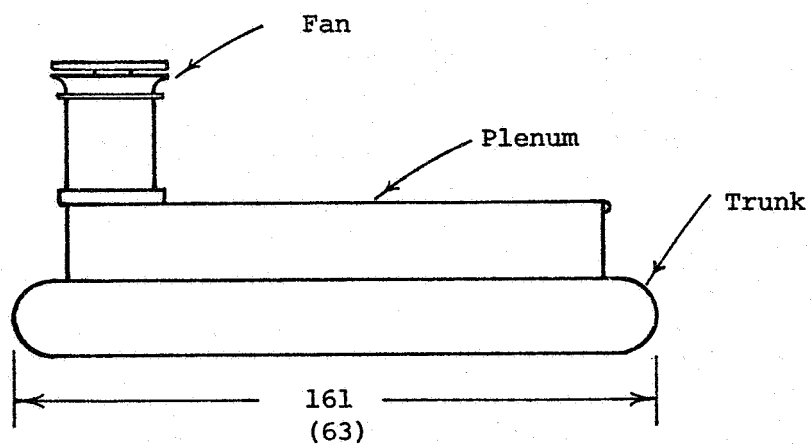
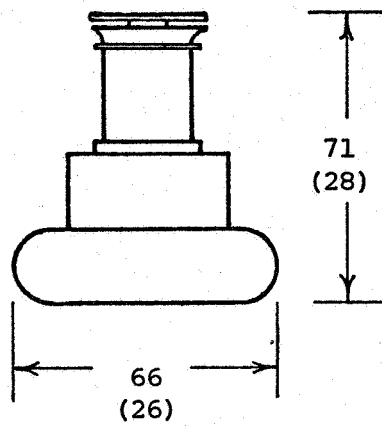
Figure 21. The Test Rig

Test Hardware

The Prototype Cushion

The prototype ACLS selected for testing was a unit developed earlier by Boeing as part of a Navy contract (ref. 28). A diagram of the ACLS including details of the trunk and fan are shown in Figure 22. The unit consists of an aluminum frame which forms the plenum and provides the attachment points for the trunk. The fan is mounted directly on the plenum at one end. The trunk, which is made of fabric reinforced molded polyurethane, is attached at the inner and outer periphery by means of metal retaining strips bolted to the plenum, and was designed for easy removal and replacement. This turned out to be a very useful feature since the original trunk appeared to have been weakened through prolonged storage in the creased condition and ruptured repeatedly during the static pitch tests. The initial failures were repaired successfully using a commercially available two part polyurethane casting resin. Later, however, a major rupture developed in the inner attachment zone and the trunk had to be replaced. Fortunately, a back-up trunk was available. Static tests repeated with the second trunk gave results virtually identical to those obtained with the first trunk. Apparently due to better storage, the backup trunk survived all static and dynamic tests without rupture.

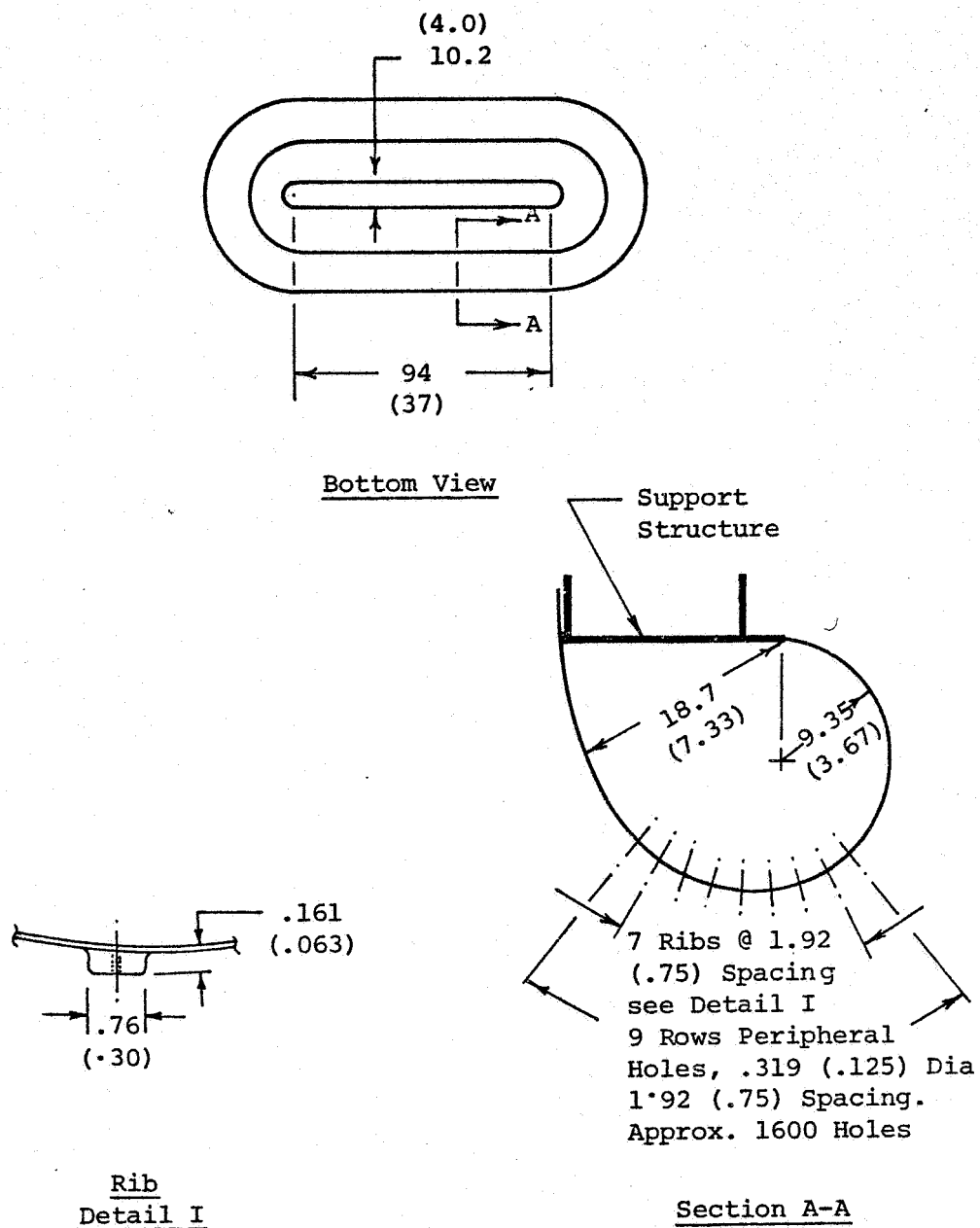
The ACLS (with fan) weighed about 61 kg (135 lbs.). However, during testing a counterweight was added to balance the off-center weight of the fan and set the nominal pitch moment to zero. This counterweight along with the constraint mechanism of the test fixture increased the total weight to 89 kg (195 lbs.). The rotational inertias of the system about the CG, calculated from measurements of its angular acceleration as a compound pendulum, were



Dimensions in cm (in)

(a) Overall View

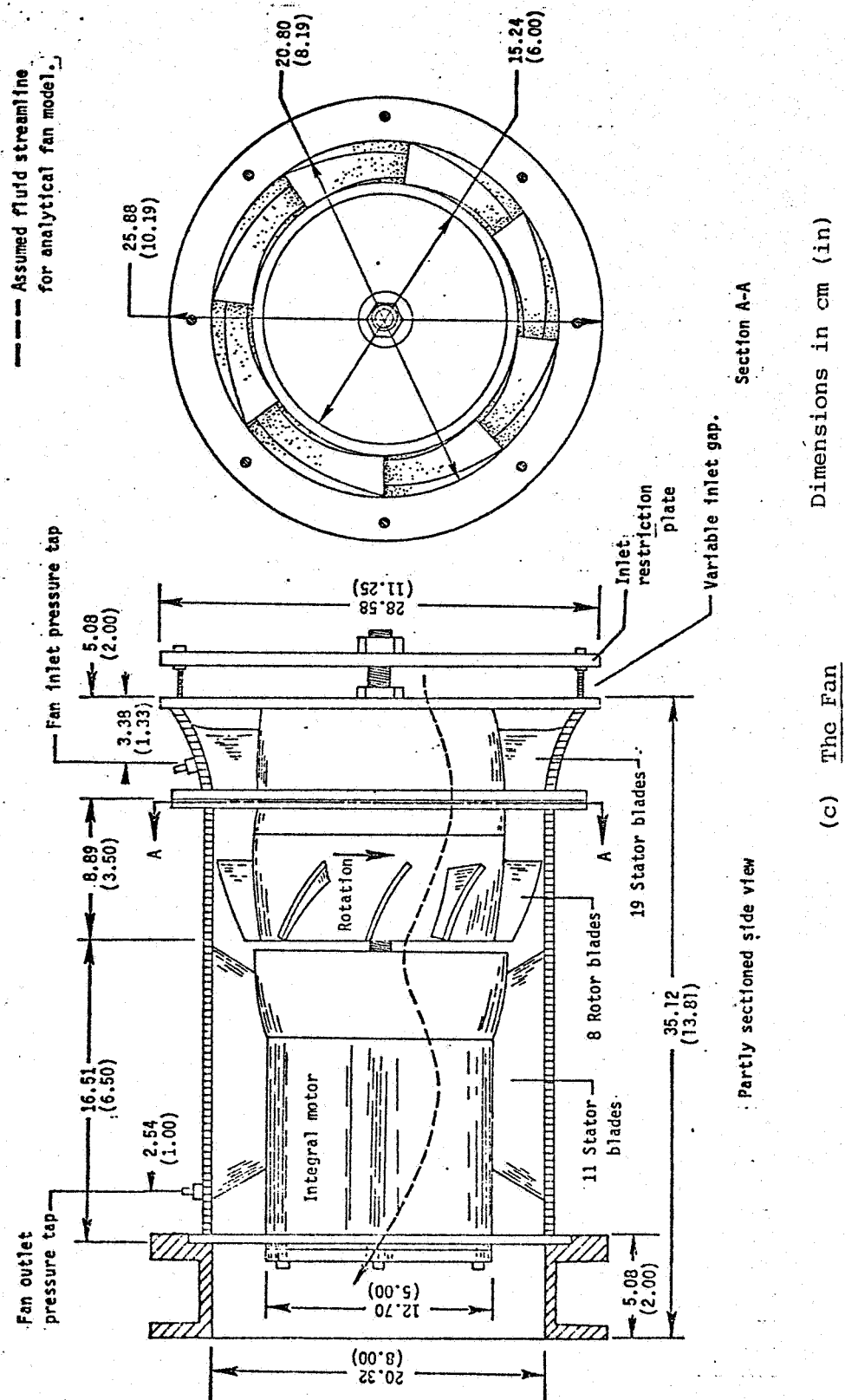
Figure 22. The Test Cushion



Dimensions in cm (in)

(b) The Trunk

Figure 22 (continued). The Test Cushion

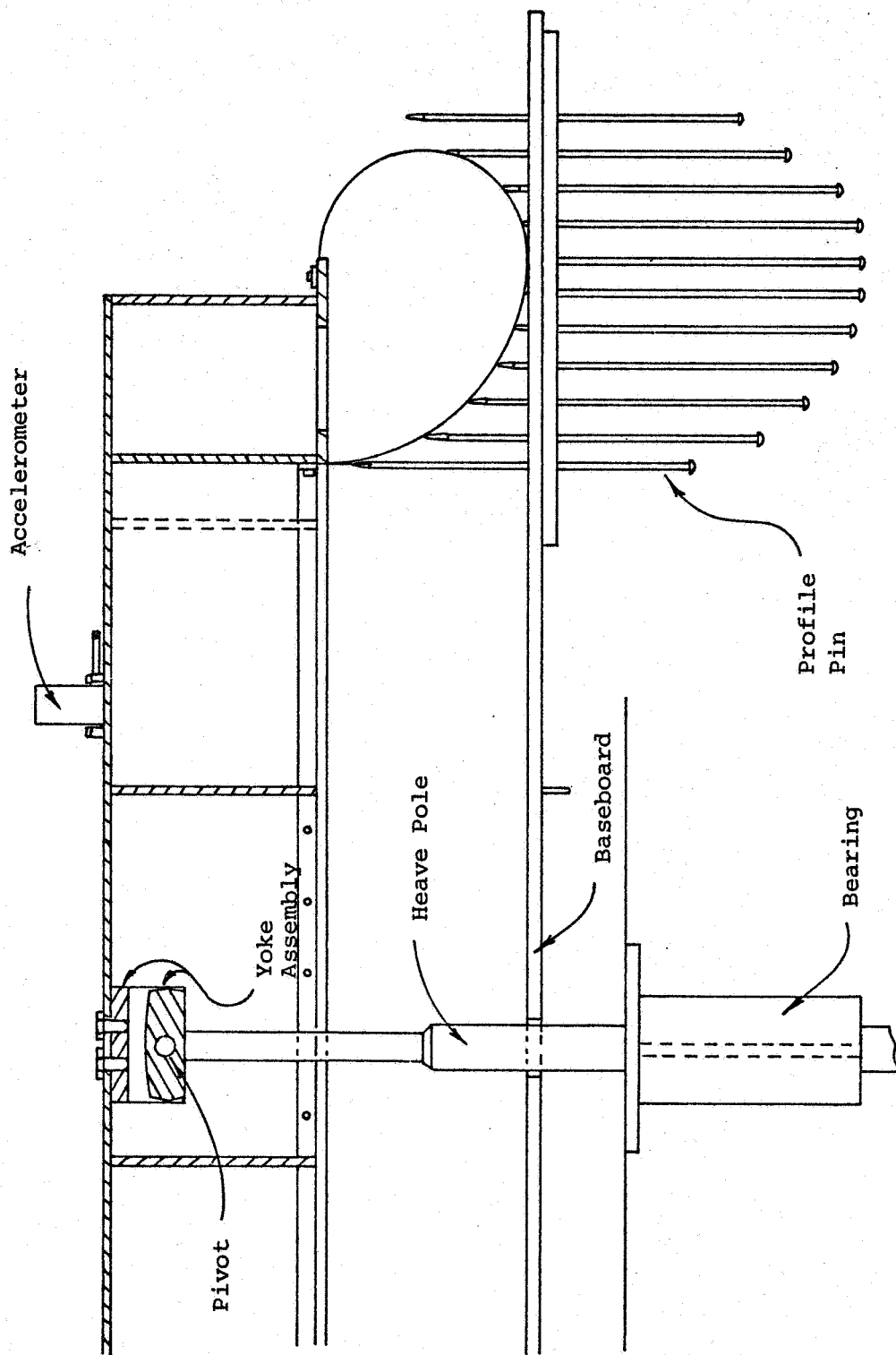


found to be 15.4 kg-m^2 (11.38 slug-ft^2) in pitch and 4.53 kg-m^2 (3.35 slug-ft^2) in roll. The fan, which requires a 200V, 400 Hz, 3 ϕ , 35 KVA power supply was powered by a motor-generator set.

The Test Rig

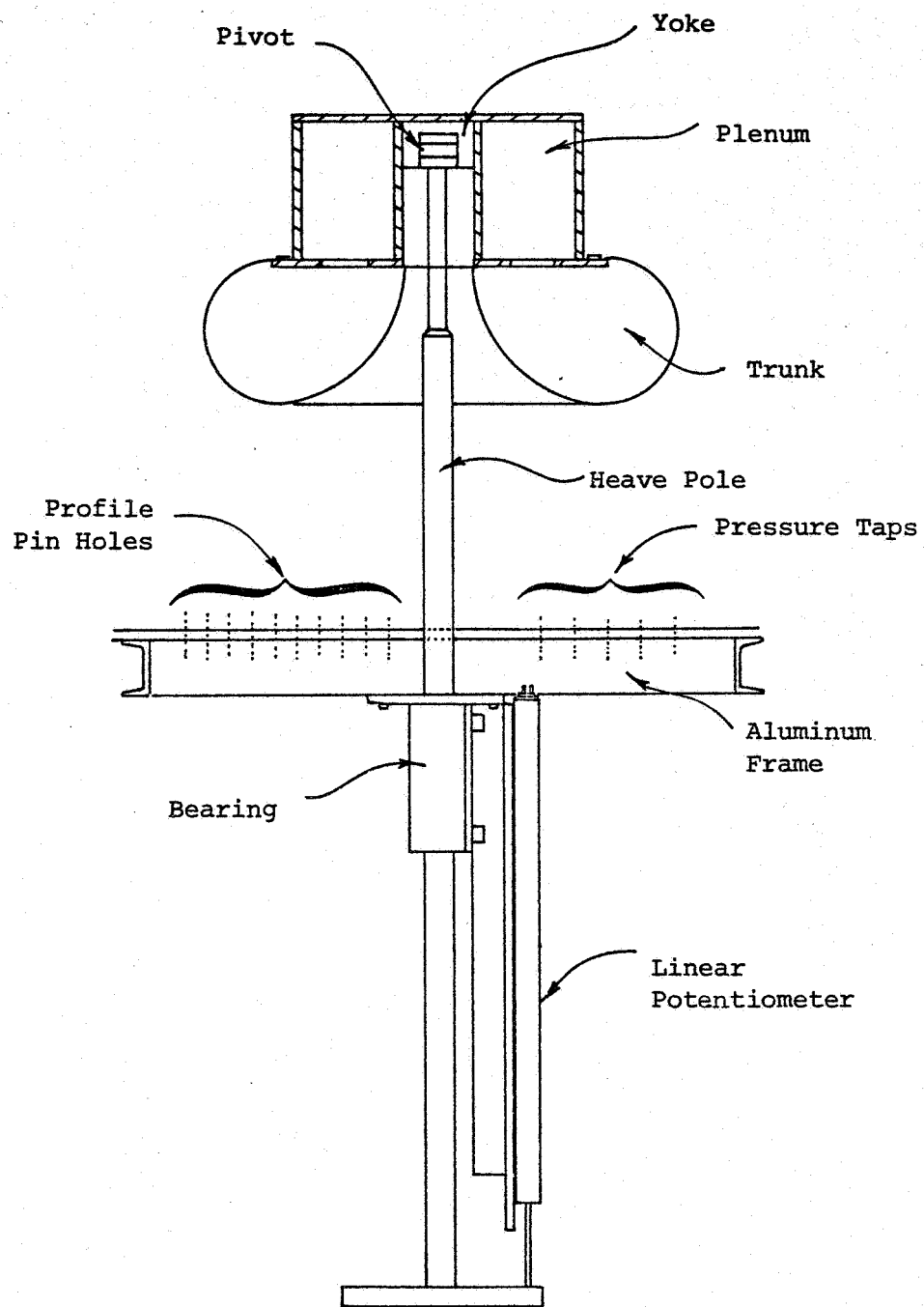
The test rig was designed to carry out static and dynamic testing of the ACLS both in the individual isolated modes (heave, pitch or roll) and in the coupled modes (heave-pitch or heave-roll). An overall view of the test rig is shown in Figure 23. It consists of a stand made of Unistrut channels reinforced by cross members, and supporting an aluminum frame to which is attached a transparent plastic (Plexiglas) baseboard at eye-level. A non-rotating linear bearing is fastened to the frame at the center of the baseboard, and a steel shaft (heave pole) which slides through the bearing is attached at its upper end to the cushion via a pivot and yoke assembly. The system was designed so that the pivot axis passes through the CG of the cushion. The function of the yoke is to allow the natural modes of motion to be isolated as follows:

- (a) Pure Heave. When the lower part of the yoke is bolted directly to the top plate of the cushion (Figure 24a), the pivot is constrained from rotating, and the cushion can only move in heave as the heave pole slides through the linear bearing. Any desired pitch or roll angle for the cushion can be set by introducing an appropriate shim or wedge between the yoke and top plate. In this mode, the cushion is raised or lowered by a hydraulic jack acting on the lower end of the heave pole.
- (b) Pure Roll. When the bolts fastening the lower yoke to the top plate of the cushion are removed, the cushion is free to rotate in roll about the pivot (Figure 24b).



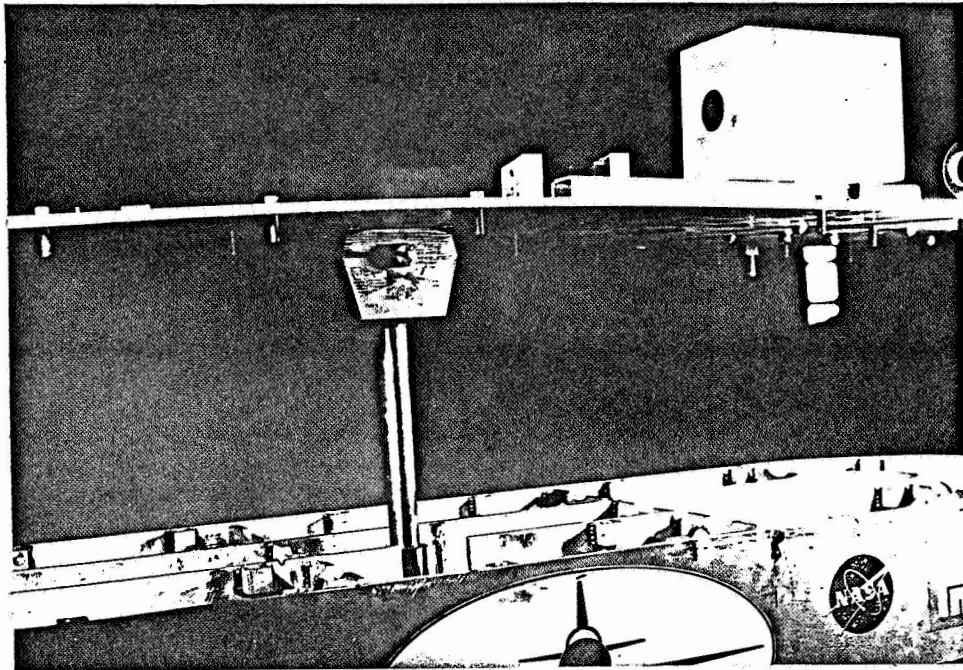
(a) Side View (Section)

Figure 23. The Test Rig

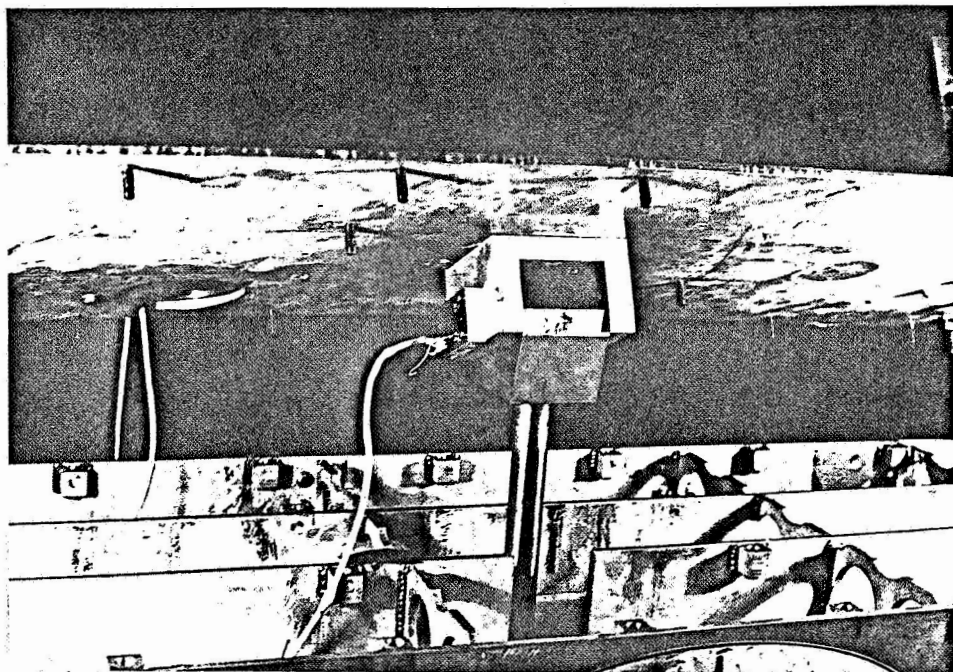


(b) End View (Section)

Figure 23 (concluded). The Test Rig



(a) Pure Heave



(b) Pure Roll

Figure 24 The Yoke Assembly

In this mode, a collar clamped onto the heave pole just above the bearing sets the height of the cushion and prevents vertical motion.

- (c) Pure Pitch. When the yoke assembly is unfastened, rotated 90° , and then reattached, the pivot orientation then allows the cushion to rotate freely in pitch.
- (d) Coupled Motion. Coupled heave-pitch or heave-roll motion is achieved by setting up the system in the pitch or roll mode and removing the collar clamped onto the heave pole to allow it to slide through the bearing.

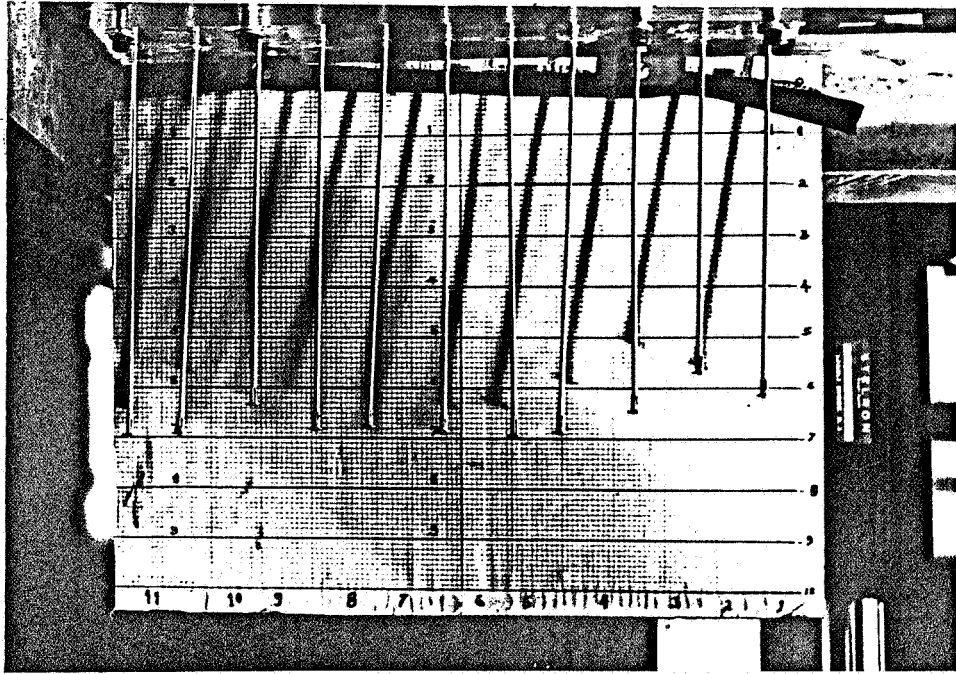
The Instrumentation

The instrumentation used for the static and dynamic tests is summarized in Table IV and discussed below.

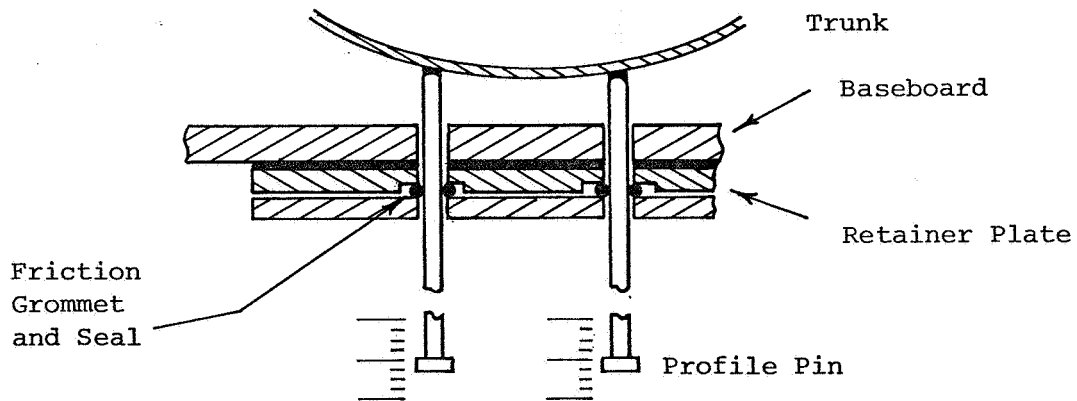
Static Test Instrumentation. - In the static tests, pressures were measured with conventional U-tube manometers. In addition to measuring fan inlet and outlet pressure, plenum, trunk and cushion pressure, base pressure at five locations in the side and end trunk contact zone were also measured (see Figure 23b). Displacements were measured with a scale: directly for linear motion and indirectly (by measuring the excursion of a radial arm) for angular motion. The load on the cushion (including its self-weight) was found by allowing the lower end of the heave pole to rest on a spring scale. The trunk shape was determined by measuring the height of the trunk above the baseboard at discrete points. This was done by means of the eleven profile pins (knitting needles) spaced 3.2 cm (1.25") apart along the baseboard under the trunk as shown in Figure 23a. Details of the profile measurement scheme are shown in Figure 25. The pins can be moved up or down to touch the

TABLE IV
SUMMARY OF INSTRUMENTATION

<u>Sensor No.</u>	<u>Variable Measured</u>	<u>Static Instrumentation</u>	<u>Dynamic Instrumentation</u>
1	Trunk Shape	Profile Pins	---
2	Trunk Contact Pressure	Manometer	---
3	Fan Inlet Pressure	Manometer	Pressure Transducer
4	Fan Exit Pressure	Manometer	---
5	Plenum Pressure	Manometer	Pressure Transducer
6	Trunk Pressure	Manometer	Pressure Transducer
7	Cushion Pressure	Manometer	Pressure Transducer
8	Heave Displacement	Scale (Ruler)	Linear Potentiometer
9	Pitch Angle	Scale (Ruler)	Rotary Potentiometer
10	Roll Angle	Scale (Ruler)	Rotary Potentiometer
11	Cushion Load	Spring Scale	---
12	Heave Acceleration	---	Accelerometer
13	Pitch Acceleration	---	Accelerometer
14	Roll Acceleration	---	Accelerometer



(a) Front View



(b) Sectional View

Figure 25. Trunk Profile Measurement

trunk, and are held in place by friction grommets. The positions of the lower end (head) of the pins, which are equivalent to the trunk height coordinates, are read off on a scale. The profile pin assembly is detachable, and can be positioned either under the side or end trunk segments.

Dynamic Test Instrumentation. - A schematic diagram of the dynamic instrumentation system is shown in Figure 26. Signals from the transducers pass through signal processors and are recorded on an eight channel strip chart recorder. Each signal processor consists of an amplification stage followed by a low-pass Butterworth filter to cut out noise (Figure 27). Two types of processors were used depending on the strength of the transducer output signal. The pressure transducers and accelerometer, which have a low output, were connected to high gain processors (gain of 100). The linear and rotary potentiometers, which have higher outputs, were used with low gain processors (gain from 1 to 10).

The instrumentation specifications are given in Table V. Strain gage pressure transducers were used to measure system pressures and communicated with the plenum, trunk, cushion, etc. through short plastic tubes. Acceleration was measured with a moving mass linear accelerometer. To measure angular acceleration, this unit was mounted a known distance away from the center of rotation so that the output could be converted to angular acceleration by dividing by the moment arm. The linear potentiometer, which measures the heave displacement of the cushion was attached vertically to the aluminium frame, with the moving arm (wiper) attached to the lower end of the heave pole (see Figure 23). The rotary potentiometer, used to measure roll and pitch motion, was attached to a bracket on the yoke and connected to an extension of the pivot (see Figure 24b).

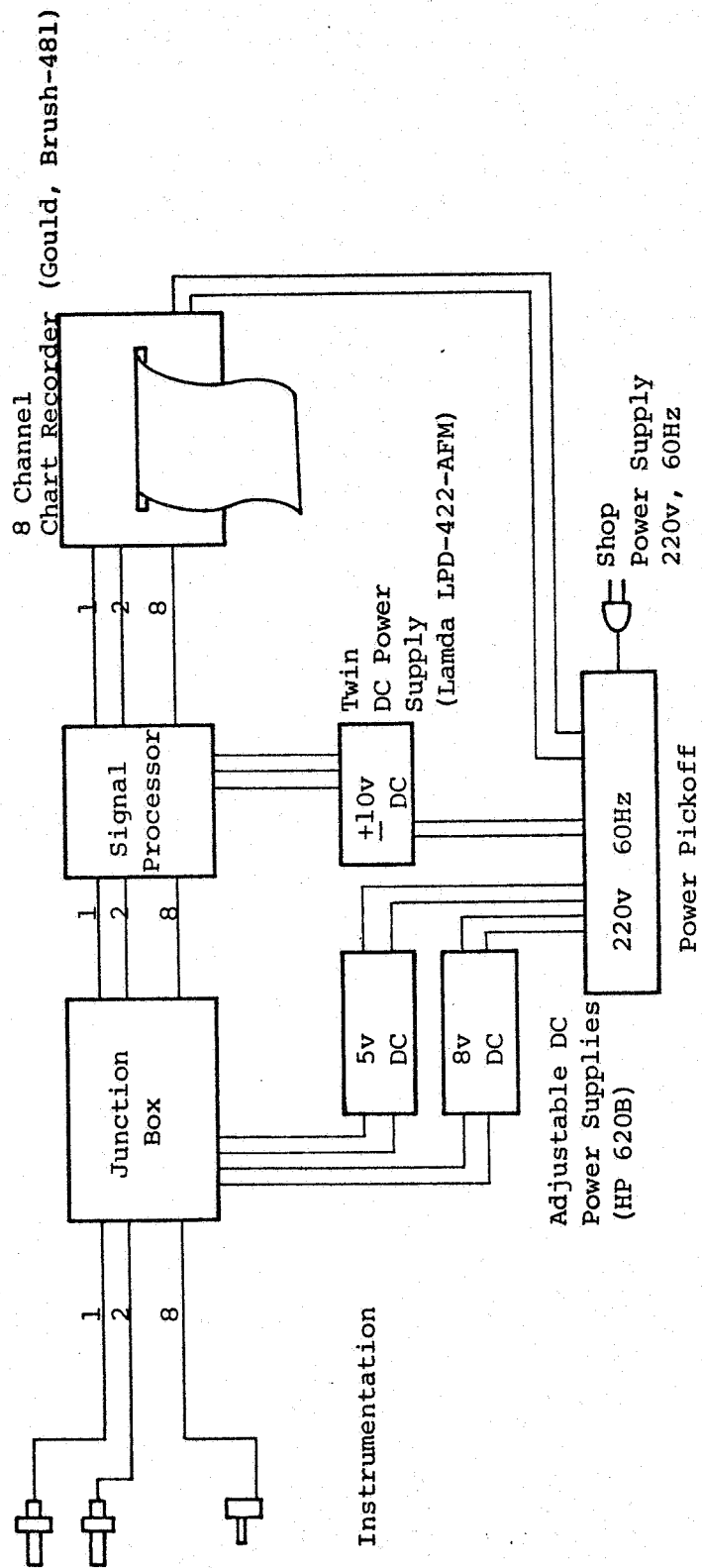
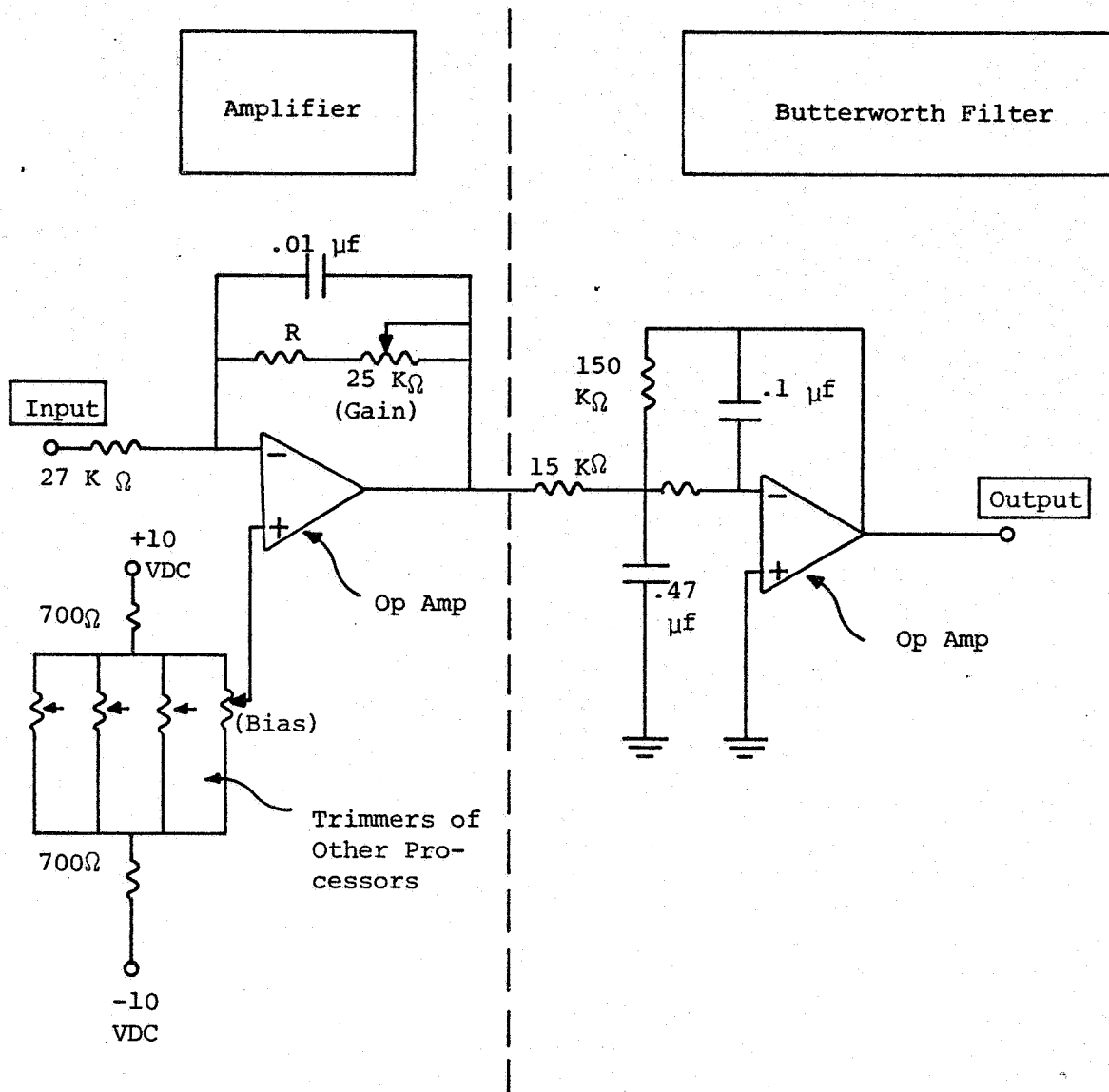


Figure 26. Instrumentation System Schematic (Dynamic Tests)



Specs:

DC Gain		
R=270 K Ω	100	
R= 15 K Ω	1-10	
Max. Input Signal		
R=270 K Ω	+0.1V	
R= 15 K Ω	+1V	
Supply Voltage	+10VDC	
Input Impedence	27 K Ω	
Roll-off Frequency	10 Hz	

Figure 27. The Signal Processor

Table V
Dynamic Instrumentation Characteristics

SENSOR	VARIABLE MEASURED	MANUFACTURER	SPECIFICATIONS
Pressure Transducers (Four)	Fan Inlet, Plenum, Trunk & Cushion Pressure	Statham Instruments, Oxnard, California	PM 131 TC \pm 2.5-350 Range: \pm 2.5 psi diff.
Accelerometer	Heave, Pitch and Roll Accel.	Statham Instruments, Oxnard, California	G312, A5a-5-350 Range: \pm 5g.
Linear Potentiometer	Heave Motion	Waters Manufacturing, Wayland, Massachusetts	LF-24 Range: 24"
Rotary Potentiometer	Pitch & Roll Angle	Waters Manufacturing, Wayland, Massachusetts	WP 7/8 M

All signal leads were shielded. However, the presence of high-current, high-frequency power cables going to the fan made it apparent that a low-pass filter stage was needed before the signals could be recorded. Trunk flutter also induced noise in the signals. For these reasons, a Butterworth filter was included in the signal processor. The frequency response of the filter is shown in Figure 28. Its roll-off frequency (3 db bandwidth) was set at 10 Hz, since this is about the upper limit of the dominant ACLS frequencies of interest.

Test Procedure

The procedure followed to carry out the static and dynamic tests of Table III is given below.

Static Tests

- (a) Adjust yoke to set appropriate mode (heave, pitch or roll), and angle of attack (heave test only).
- (b) Raise cushion with hydraulic jack under heave pole.
- (c) Turn on power to fan
- (d) Inspect trunk
- (e) Lower cushion slowly onto baseboard
- (f) Set CG height and lock heave collar (pitch and roll tests only)
- (g) Set cushion load (and moment) by adding (offset) weight.
- (h) Take trunk profile readings (side trunk) (Sensor #1)
- (i) Take base pressure readings under side trunk (Sensor #2)
- (j) Move profile pins and base pressure taps to end trunk location

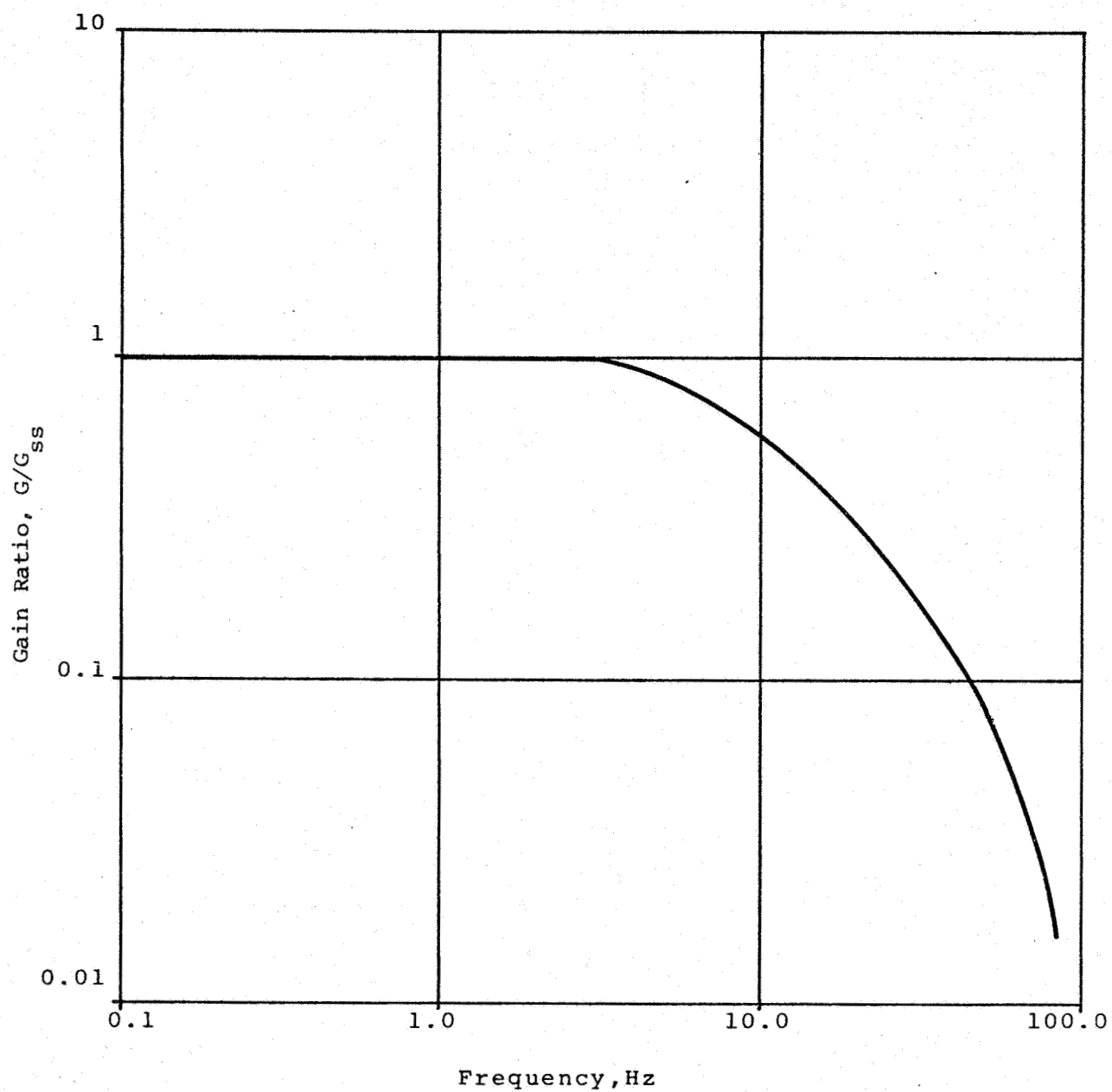


Figure 28. Frequency Response of the Signal Processor

- (k) Take trunk profile readings (end trunk) (Sensor #1)
- (l) Take base pressure readings under end trunk (Sensor #2)
- (m) Read fan inlet and outlet pressure and plenum, trunk and cushion pressure (Sensor #s 3-7)
- (n) Measure vertical position or angle (Sensor #8, 9 or 10)
- (o) Remove cushion load
- (p) Unlock heave collar (pitch and roll tests only)
- (q) Raise cushion
- (r) Inspect trunk
- (s) Turn off power to fan.

Dynamic Tests

- (a) Adjust yoke to set appropriate mode and angle of attack
- (b) Raise cushion to drop height with hydraulic jack (heave test) or set CG height and lock heave collar (pitch and roll test)
- (c) Turn on power to fan
- (d) Inspect trunk
- (e) Activate instrumentation and recording system
- (f) Add unbalanced weight to cushion (pitch and roll tests only)
- (g) Release jack (heave test) or unbalanced weight (pitch and roll test) and allow oscillations to die down
- (h) Turn off instrumentation system
- (i) Unlock heave collar (pitch and roll tests only)

- (j) Raise cushion
- (k) Inspect trunk
- (l) Turn off power to fan

Test Results

Parameter Evaluation

Discharge Coefficient. - The discharge coefficient for the trunk holes can be easily found from the fan characteristic and the measured plenum and trunk pressures. When the cushion is high up off the ground, all the trunk holes discharge to the atmosphere. From the orifice equation, the discharge coefficient is given by

$$C_d = \frac{Q}{A \sqrt{2 (P_t - P_a) / \rho}} \quad (34)$$

where Q is the total flow
 A is the total trunk hole area
 ρ is the air density
 and $(P_t - P_a)$ is the pressure drop across the trunk orifices

The flow Q which is a function of the plenum pressure P_p can be estimated from the static fan characteristic shown in Figure 10. Solving Eqn (34) for the high up test condition gives a trunk hole discharge coefficient of 0.76.

The discharge coefficient for cushion outflow through the clearance gap, however, cannot be found from the tests, because the gap area is unknown. However, since the trunk profile in the

cushion gap region is very similar to a two-dimensional converging nozzle, the discharge coefficient for cushion outflow will be close to unity. Thus, when quantifying the analytical model, discharge coefficients of 0.76 and 1 have been used for the trunk and cushion gap orifices respectively.

Trunk Damping Constant. - There are three damping mechanisms in ACLS: (a) backflow losses in the fan, (b) stagnation pressure losses due to cyclic flow through the orifices, and (c) energy losses due to cyclic deformation of the trunk*. When analyzing test data to evaluate the trunk damping constant D_c (see Eqn. (30)), it is important to consider only those test modes where the first two components are negligible, so that the results quantify the damping contribution of the trunk and not that of the total system. In heave vibration, all three damping components are present, because the fan can stall and the flow through the plenum and trunk orifices is changing. In pitch and roll, however, (as is shown later in Figure 36) the fan flow and plenum and trunk pressures remain constant, so that only the trunk damping component is present in these modes. Because the contact periphery in pitch is larger, it is more convenient to use the pitch test data to evaluate the trunk damping constant D_c . This was carried out by solving Eqns (30) and (32) to match the cyclic attenuation in pitch angle response (Test No. 2.2, Table III), which gave a trunk damping constant D_c of 0.15 kPa·s (3.2 lb · sec/ft²). This value is for a fabric reinforced polyurethane trunk, which is non-stretching in tension, but very flexible in bending. Pitch data of another trunk (the Buffalo) were also analyzed to give a trunk damping constant of 8.4 kPa·s (176 lb · sec/ft²). This value is for a Nylon ply reinforced rubber trunk

* If present, relief valve flow losses will be a fourth damping mechanism.

made of two-way stretch material that is also flexible in bending.* Although additional trunk data is needed before the form of the damping model can be verified, the two initial results show the right trend, because the more stretchable Buffalo trunk probably dissipates more internal energy and hence gives a higher value for the trunk damping constant.

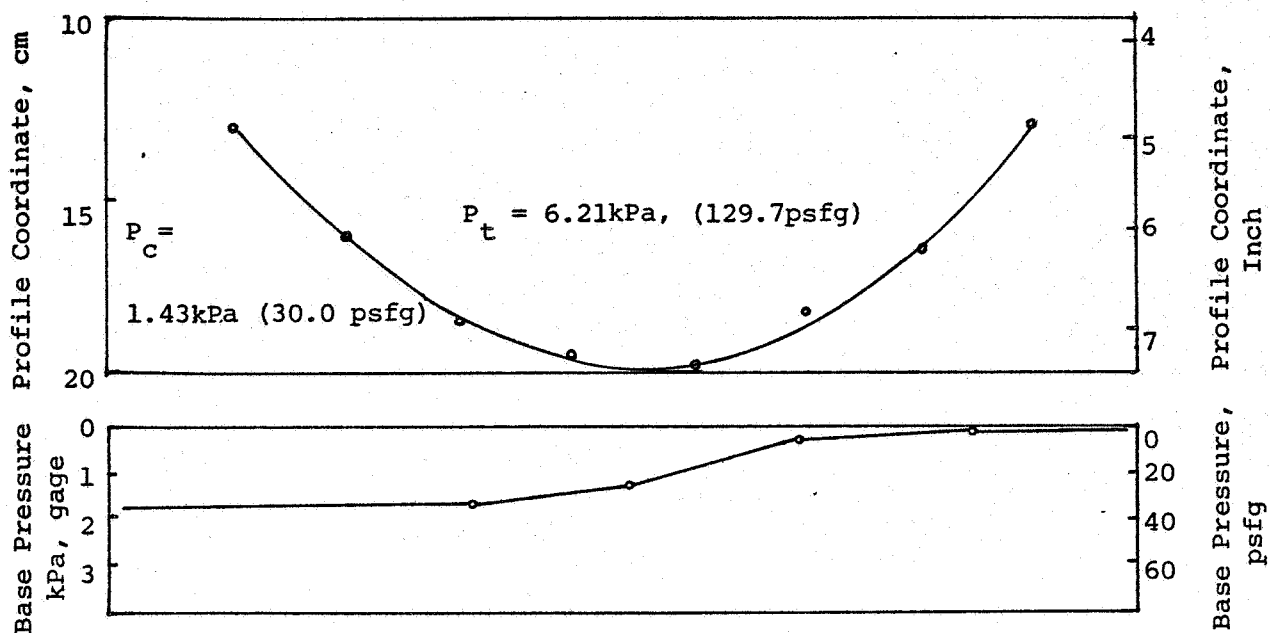
Trunk Shape and Base Pressure

The test data confirmed that the trunk side segments behave differently from the end segments. As the cushion loading increases, the side segments bow outward while the end segments flatten (see Figure 12). The base pressure distribution under the segments is also different. For the side segment, the cushion pressure drops down to ambient pressure very close to the ground tangent point of the trunk, as shown in Figure 29. Thus, as mentioned earlier, the ground tangent points form the side edges of the cushion. For the end segments, however, the base pressure under the trunk first increases and then drops down to the ambient level (Figure 30). There is thus a ground contact region under the end segments which provides an additional force component. This type of trunk behavior has already been discussed, and, in fact, formed the basis for the Hybrid Trunk Model developed earlier.

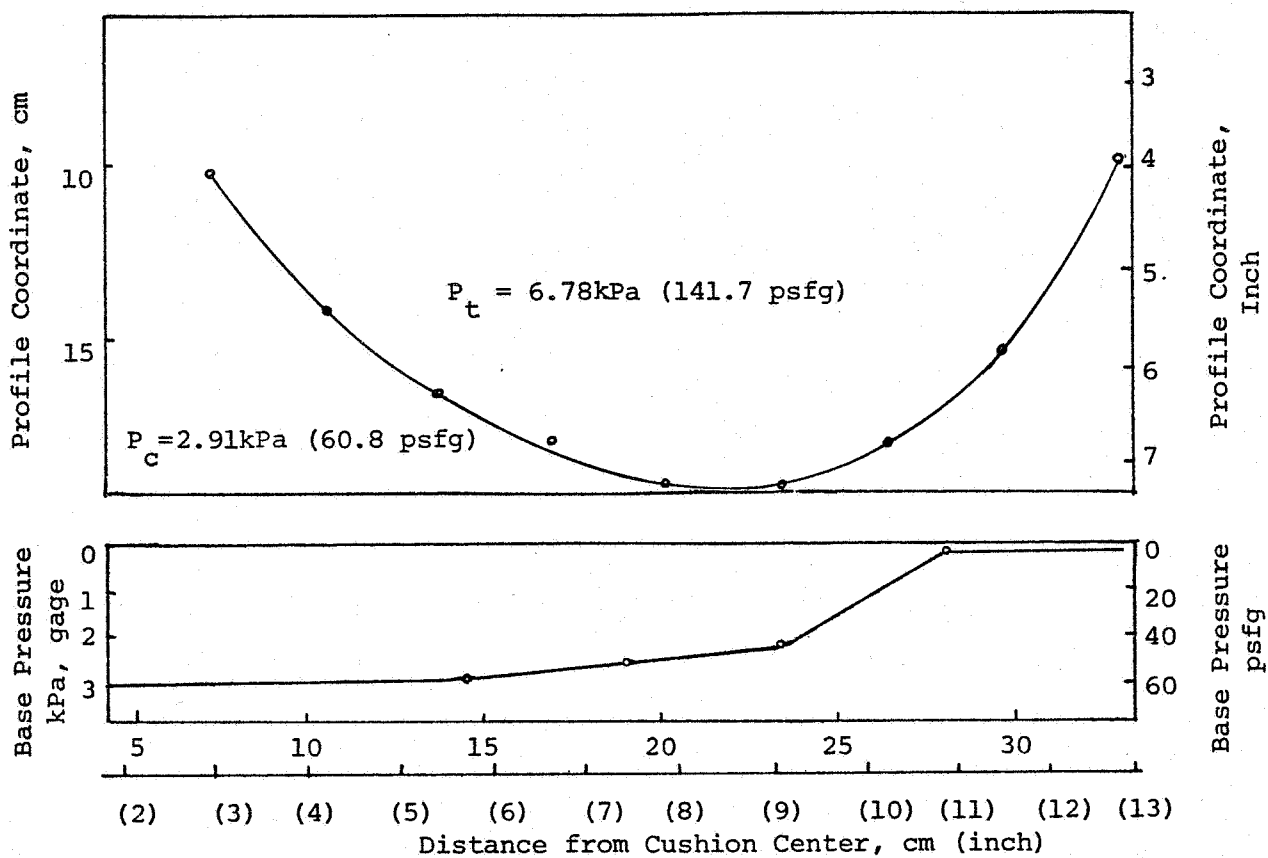
Static Characteristics

The static characteristics of the cushion are shown in Figures 31 to 33. Figure 31 shows the variation in cushion and trunk pressure as the load is increased. The cushion pressure,

* Unlike the trunk tested in this program, the Buffalo trunk is designed as an "elastic" trunk, which draws itself tight against the aircraft fuselage when not inflated.

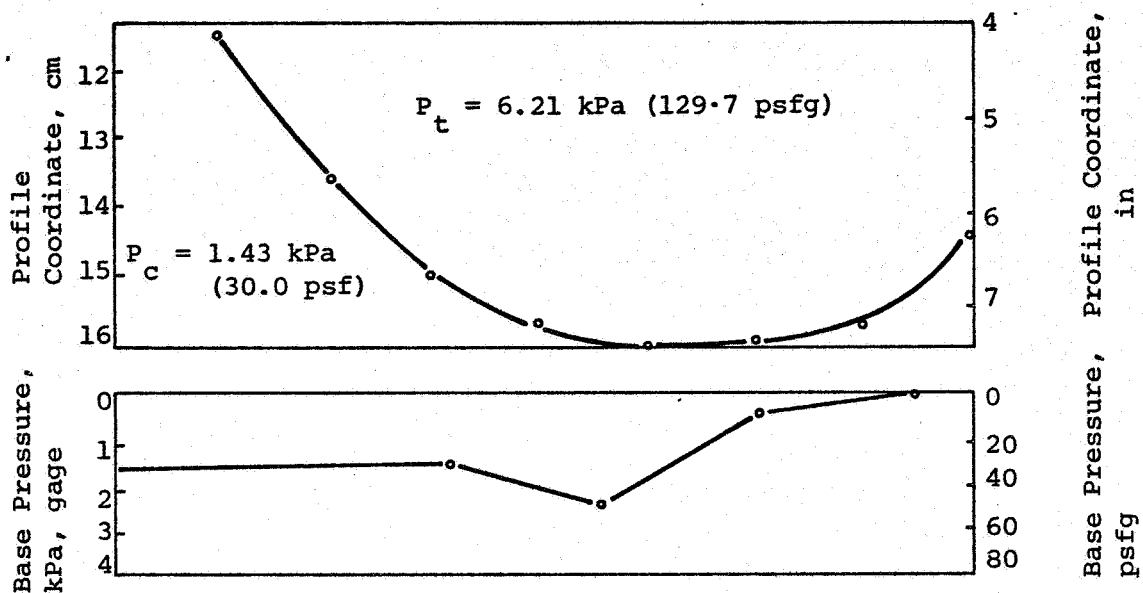


(a) Load 867 N (195 lb)

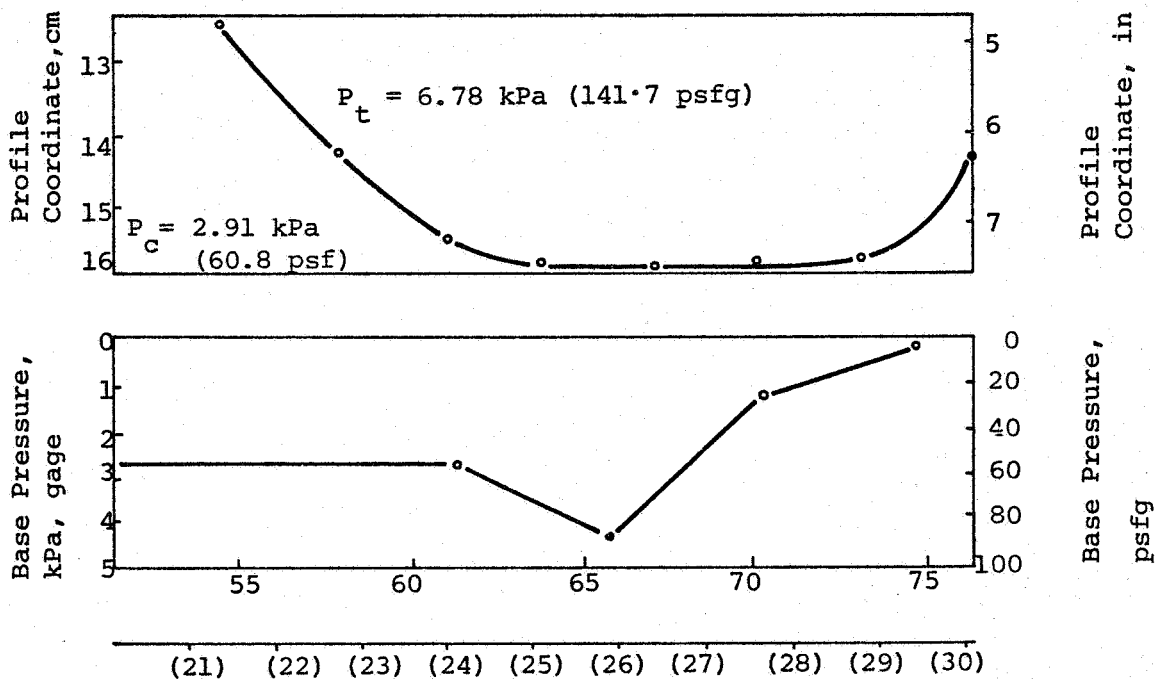


(b) Load 1900N (427 lb)

Figure 29. Trunk Profile and Base Pressure (Trunk Side) in Heave



(a) Load 867 N (195 lb)



Distance From Cushion Centre, cm (in)

(b) Load 1900 N (427 lb)

Figure 30. Trunk Profile and Base Pressure (Trunk End) in Heave

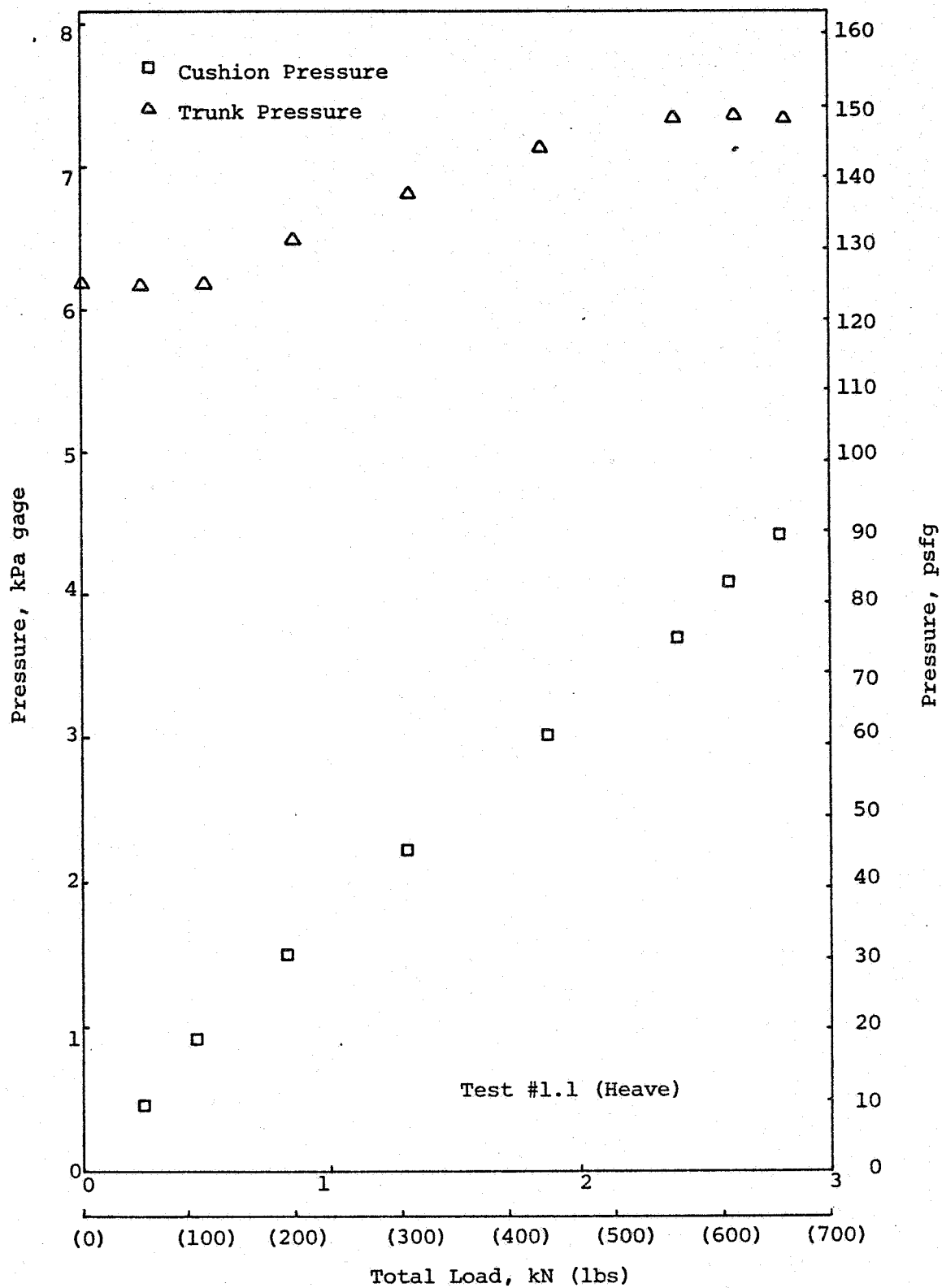


Figure 31. Pressure Variation with Load

which is zero at no load, increases almost linearly up to the maximum test load. This increase in cushion pressure occurs because the cushion-to-atmosphere gap area reduces as the load is increased, so that the cushion pressure must rise to expel the inflow coming from the trunk. The trunk pressure also rises but begins to level off at the higher loads. This happens because the fan is now operating near its maximum pressure point (see Figure 10) and large flow changes can take place without much change in pressure. It must be noted that although the cushion-to-trunk pressure ratio increases with load, the portion of the load carried by the trunk remains fairly constant at about 30 percent (see Figure 19). This happens because the trunk contact area increases rapidly with load, while the cushion area is substantially constant, so that the products of pressure and area increase at roughly the same rate.

In all tests, the plenum pressure was found to be equal to the trunk pressure because the plenum-to-trunk orifice is very large.

Figure 32 shows the hard surface clearance as a function of the load. In this case, the hard surface clearance is the distance between the trunk attachment points and the ground. The clearance decreases as the load increases due to compression of the trunk. The stiffness of the cushion, which is the inverse slope of the curve, starts initially at a low value and then increases as the trunk begins to stiffen.

Figure 33 shows the pitch and roll angle as a function of the applied moment. The tests were carried out first by increasing the moment up to its maximum value and then reducing it. The data shows a little hysteresis, probably due to nonuniform retraction of the trunk caused by friction in the contact zone. As expected, the cushion is much stiffer in pitch than in roll,

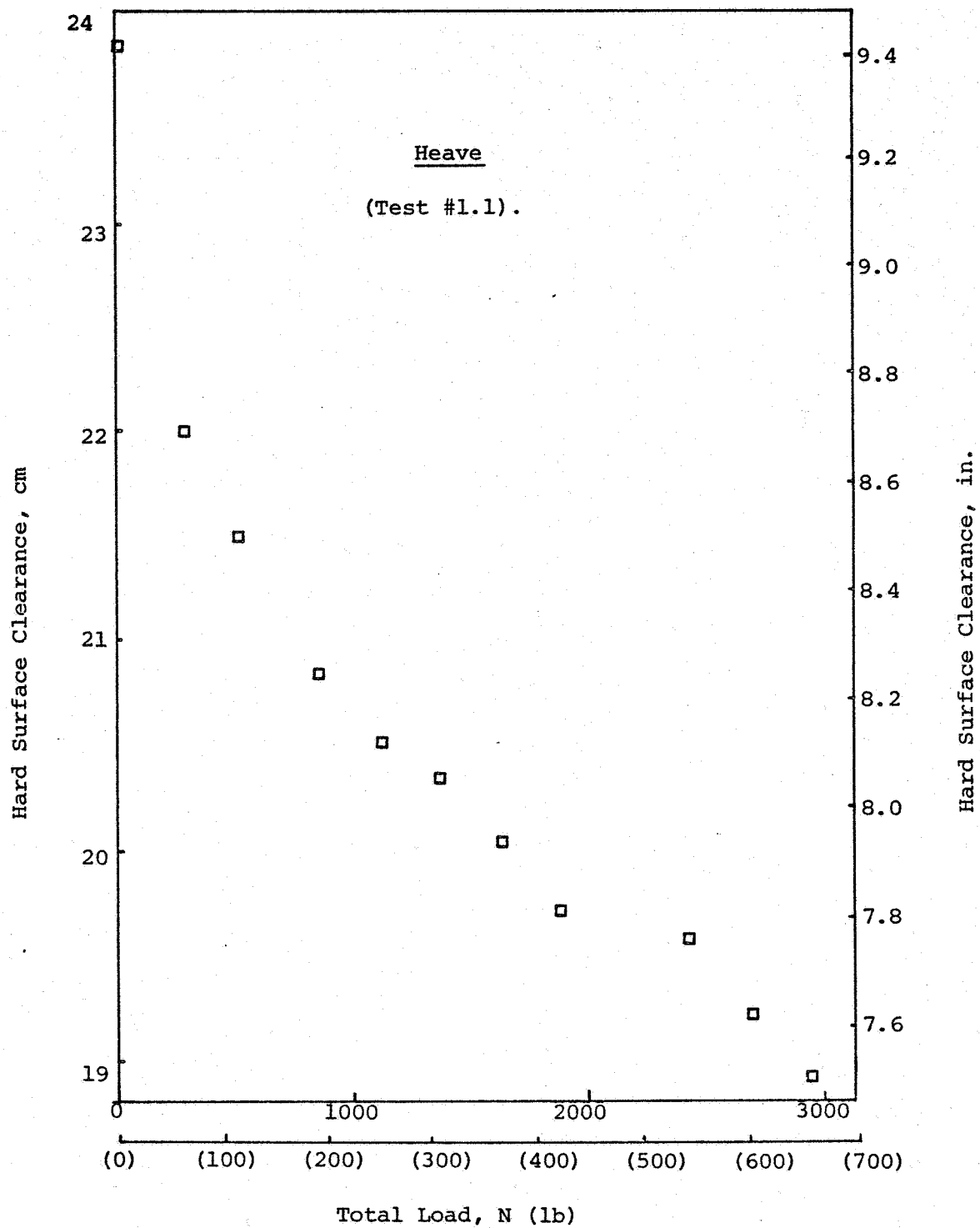


Figure 32. Hard Surface Clearance vs. Load

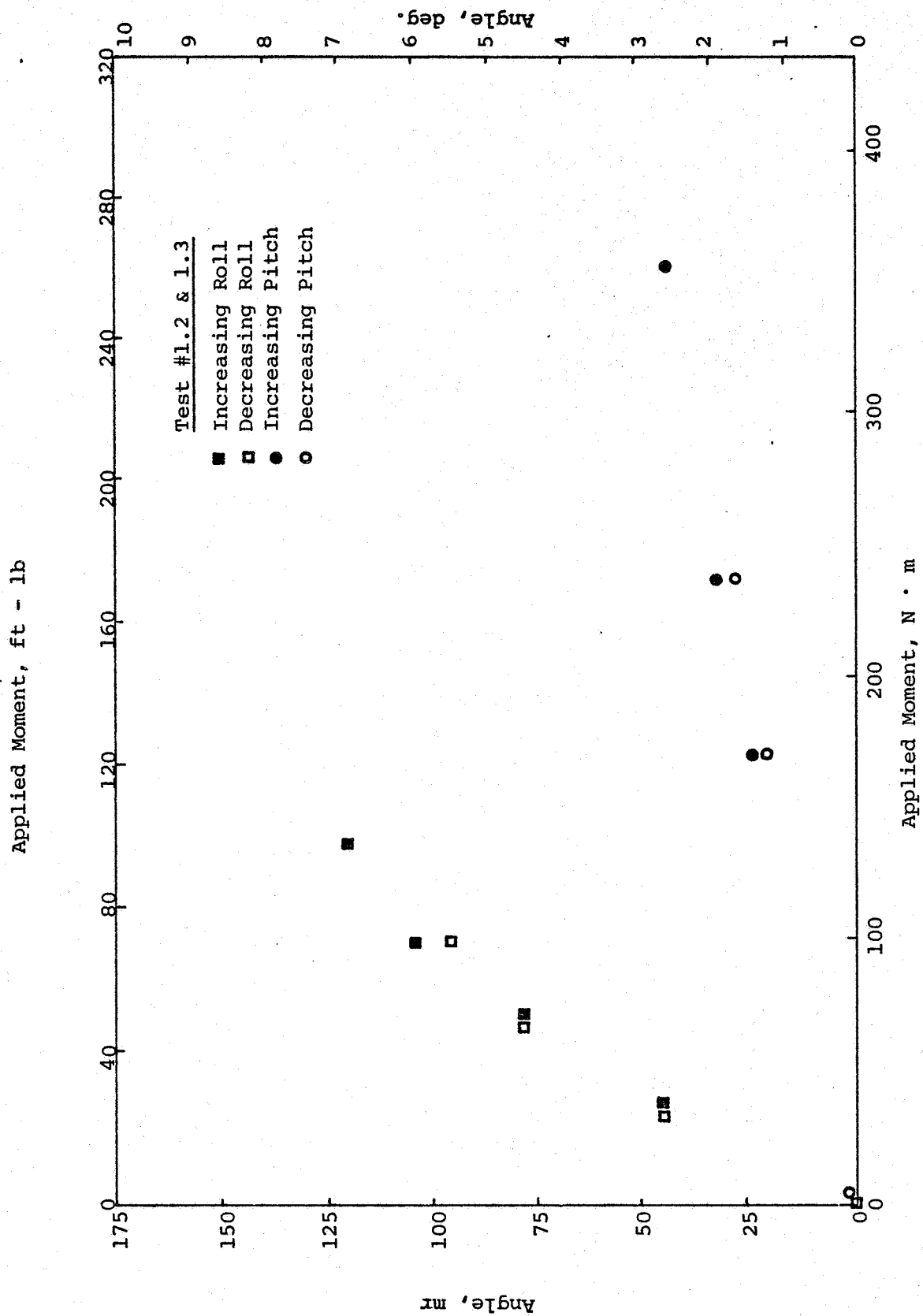


Figure 33. Angular Deflection vs Moment

primarily because the restoring forces in pitch have a much longer moment arm, because the cushion is four times longer than it is wide.

Dynamic Characteristics

The dynamic tests consisted essentially of heave drop tests and pitch and roll moment release tests. The chart recorder output for the 6" heave drop test is shown in Figure 34. The first observation on this data is that the first four cycles following the drop are different from the remainder of the vibration. This is because the initial impacts with the ground have sufficiently high kinetic energy to cause the fan to stall and delay the pressure rise. Each stall cycle however, dissipates a part of the impact energy, so that, after a few cycles, the remaining kinetic energy is below the fan stall threshold, so a non-stall vibration with faster pressure recovery takes place. Another conclusion reached from the data is that heave damping is very low and after the major perturbations have attenuated, the system exhibits a low amplitude limit cycle instability.

The stall behavior of the system can be explained with the help of Figure 35. In Figure 35a, the operating point of the fan starts from A on the static characteristic and moves along locus A B C as the trunk hits the ground and the flow is reduced. When the trunk starts moving upwards, after the impact, the flow increases and the fan operating point moves along locus C D E. The cushion has now bounced back up, and the flow returns to its initial value, A. Since the pressure drop between the fan outlet and trunk is small, the trunk pressure is practically equal to the fan outlet pressure. The trunk pressure variation can then be plotted as shown in Figure 35b, which is very similar to the observed trunk pressure variation shown in the insert. Thus the first trunk pressure peak B corresponds to the maximum pressure the fan can generate when the flow is reducing, and the second

Test #2.1 -- 6" Heave Drop

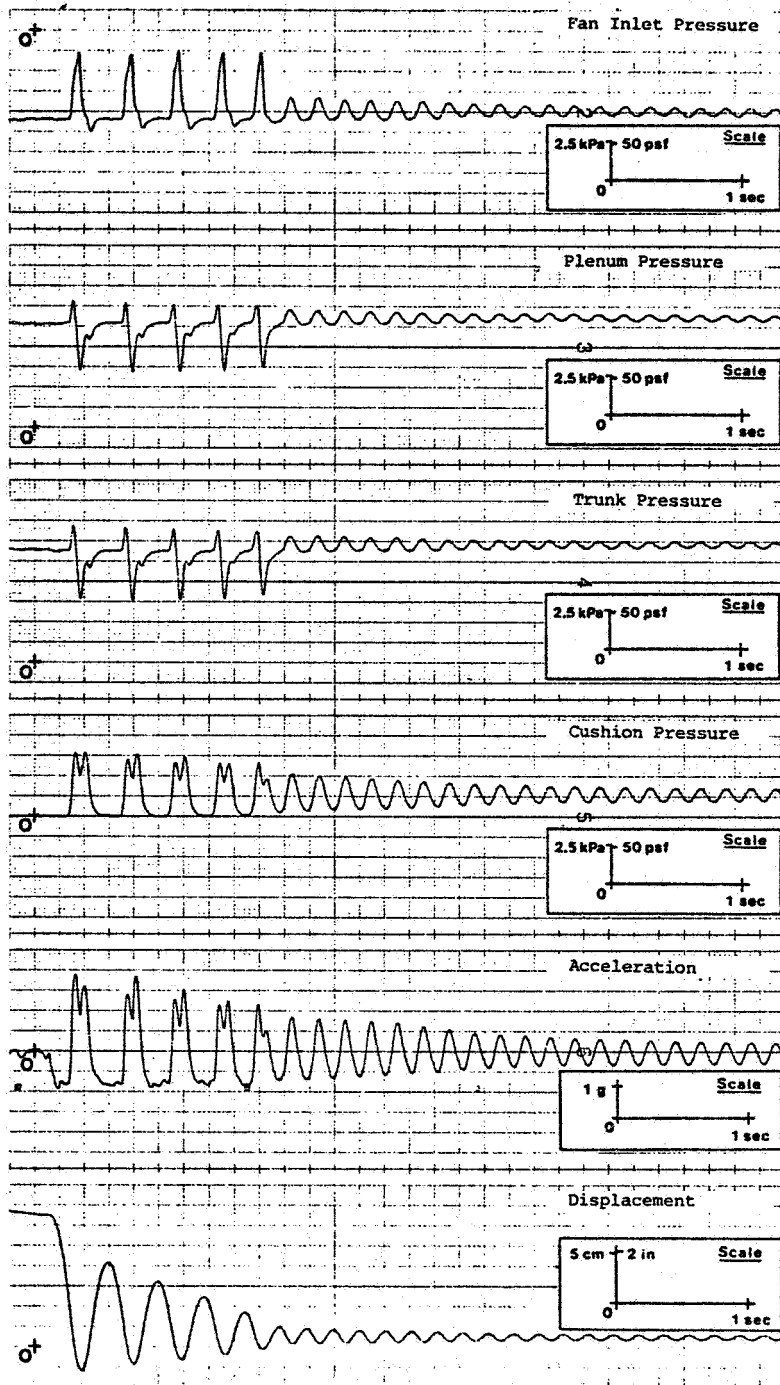
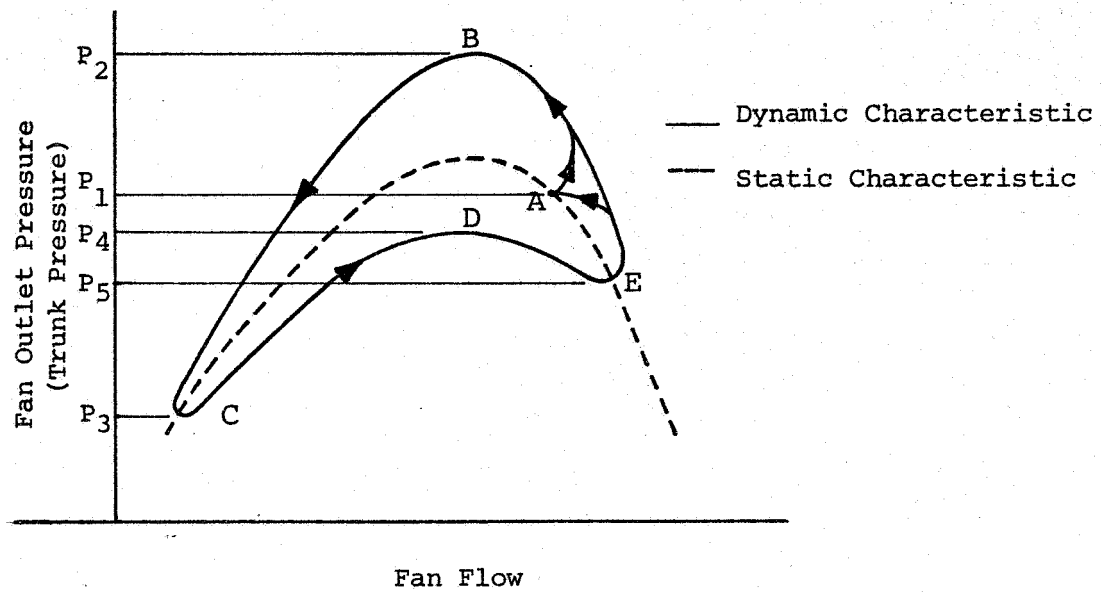
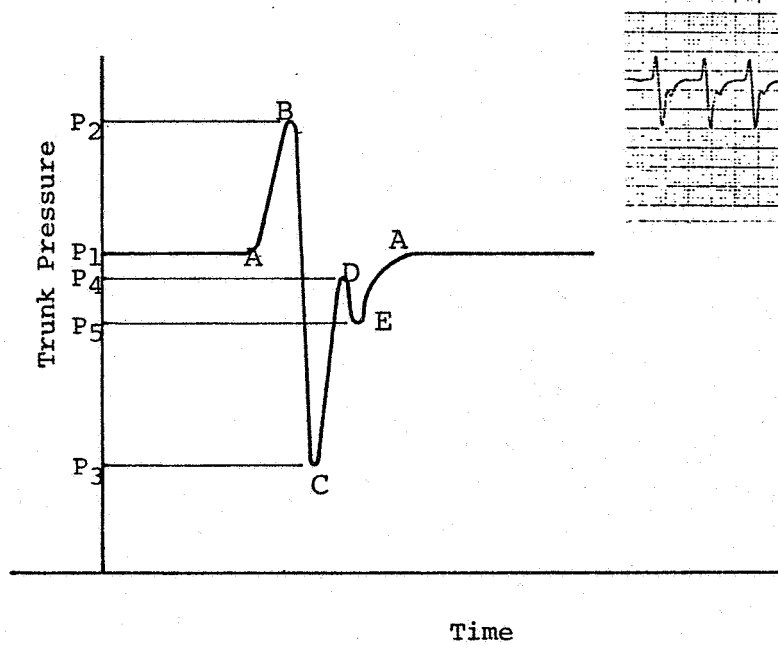


Figure 34. Dynamic Test Record (Heave)



a) Fan Operation During Impact



b) Trunk Pressure

Figure 35. The Stall Behavior of the Cushion

peak D corresponds to the maximum fan pressure when the flow is increasing. The fact that these two peaks have different magnitudes is because, in one case, part of the static fan pressure rise is taken up in accelerating the flow, while in the other, deceleration of the flow adds an extra component to the static pressure rise.

The trough C in the trunk pressure corresponds to the low flow point of the fan locus. This is verified by observing that the fan inlet pressure, which is a measure of the flow, has dropped sharply when the plenum pressure is at a minimum.

This behavior seen in the drop tests confirms the earlier fan test results that formed the basis for the dynamic fan model.

The stall behavior of the fan also causes the cushion pressure and acceleration during impact to have two peaks rather than one. As the cushion approaches the ground, the pressure and accelerating force begin to rise. Then, as the fan stalls, (locus B C, Figure 35a) the flow through the system reduces and the cushion pressure and accelerating force reduce. At point C on the fan curve, the pressure and acceleration reach a minimum, and then begin to rise as the fan recovers (locus C D). Finally, when the cushion bounces back up, the gap area increases and the cushion vents to the atmosphere, causing the cushion pressure to drop to zero, so that the system moves under gravity acceleration only. The heave displacement, however, does not show a double peak during stalled ground impact because the force variation takes place too quickly for the system to respond. There is however, a difference between the first four stall cycles and the remainder of the vibration; the difference being in the energy lost by damping. During each stall cycle, the system dissipates about 35 percent of its initial energy, as seen by comparing the successive heights of the rebound. This energy is dissipated through three mechanisms: hysteresis losses during fan stall, energy dissipation in the orifices, and flexural losses in the trunk. After about 80 percent of the drop energy is dissipated (in

about four cycles) fan stall does not occur, so one of the energy loss mechanisms is eliminated and system damping is reduced.

In fact, when fan stall is eliminated, the net damping is so low, that the system is only marginally stable, and can be excited to execute low amplitude limit cycle oscillations, as seen in the latter part of the drop test record.

Typical pitch and roll moment release tests are shown in Figure 36. The fan flow, as measured by the fan inlet pressure, remains constant, independent of angle, and so the plenum and trunk pressures also do not change. The cushion pressure, which starts out at zero because the cushion vents to the atmosphere when the pitch or roll angle exceeds a certain value, rises up to its equilibrium value as the moment is released and the cushion aligns itself parallel to the ground. The angular acceleration and displacement show a conventional damped vibratory response. System damping in pitch or roll is higher than in heave and a limit cycle instability does not occur.

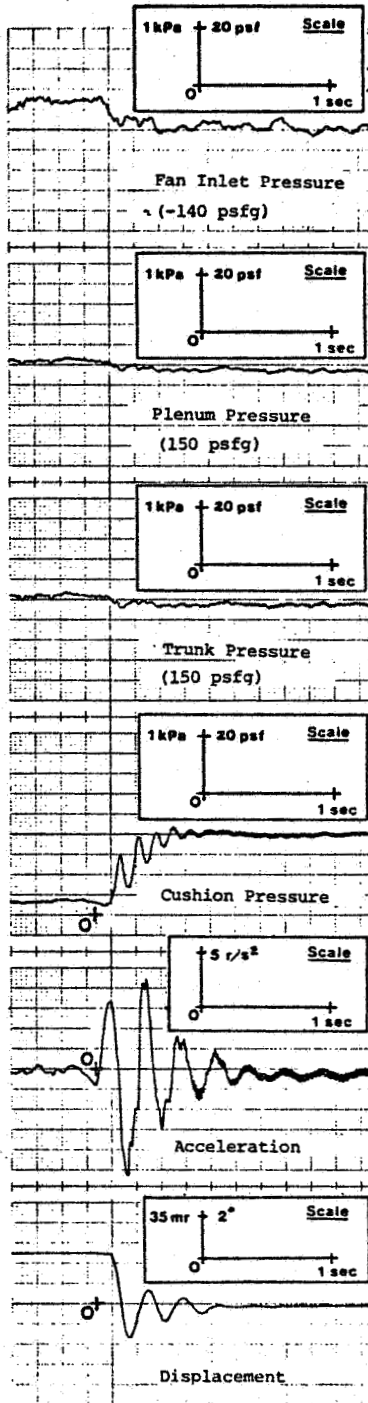
VERIFICATION OF ANALYSIS

Computer simulations of the principal test cases of Table III were carried out to check the validity of the analysis and identify the strengths and weaknesses of the analytical model. The results also give a rough idea of the accuracy that can be expected from the analytical predictions.

The Static Model

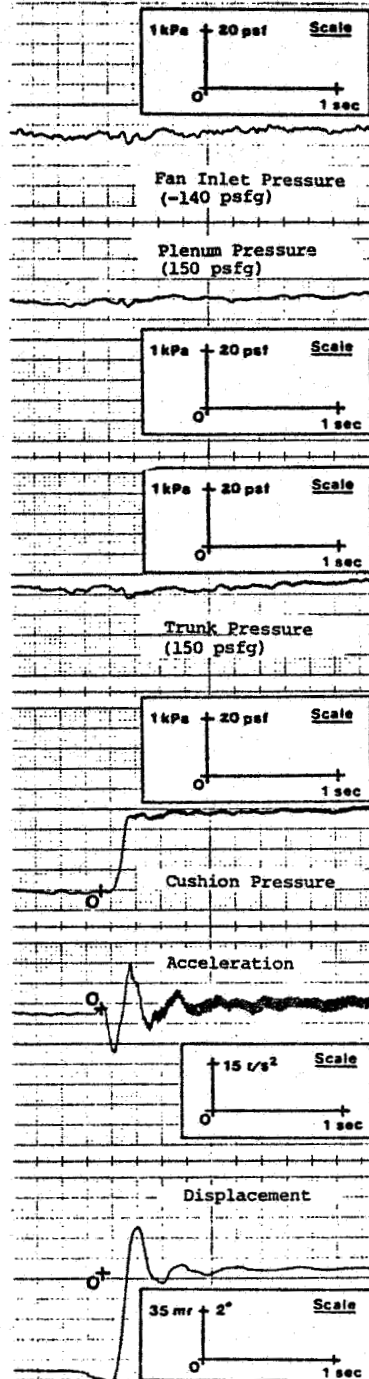
Figures 37 and 38 compare theory and experiment for the static loading of the system in heave. The first figure shows the variation in hard surface clearance, and the second figure

Test #2.2 --
41.4 mr (2.35°) Release



(a) Pitch Moment Release

Test #2.3 --
85.5 mr (4.89°) Release



(b) Roll Moment Release

Figure 36. Dynamic Test Record (Pitch and Roll)

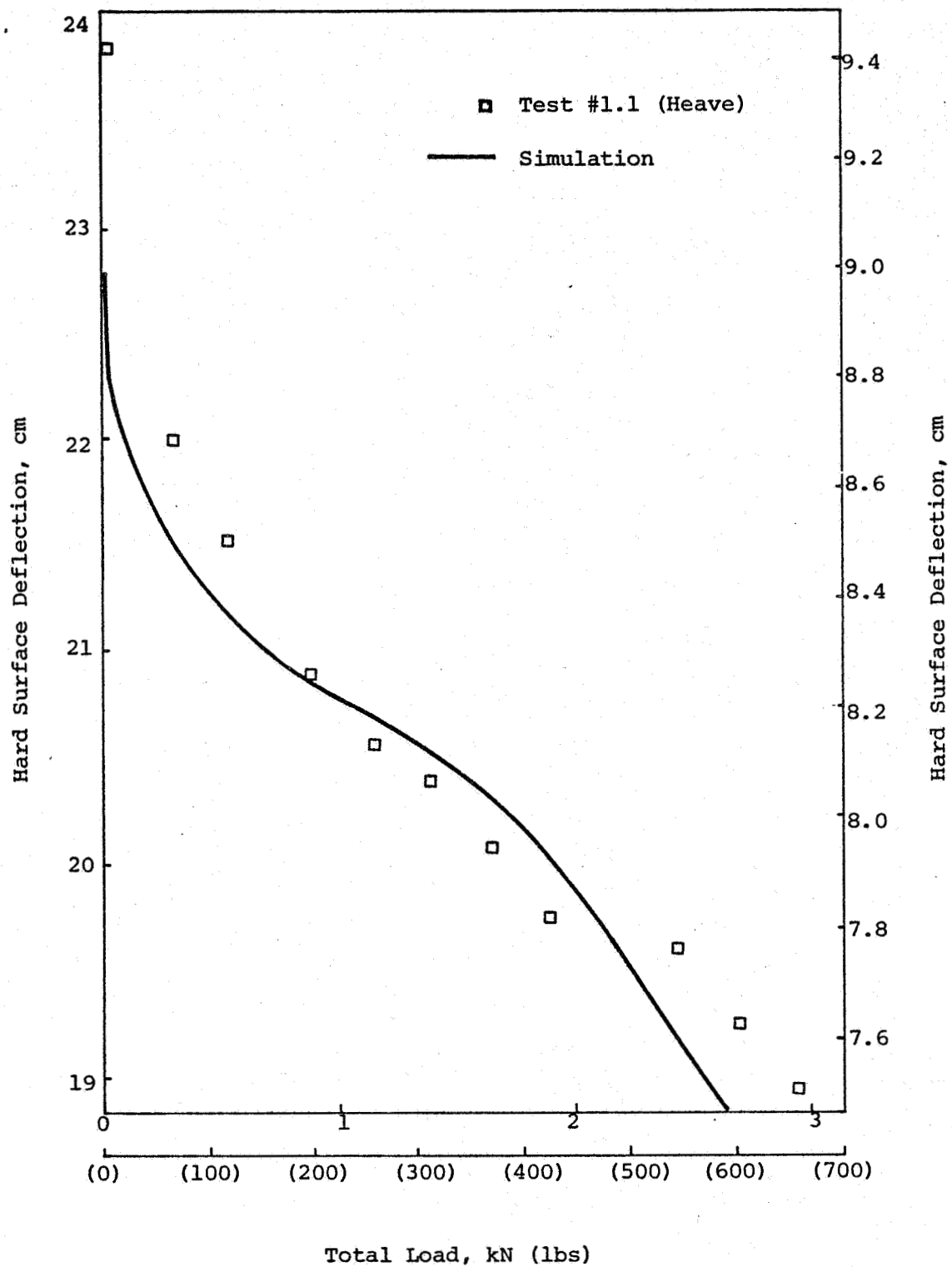


Figure 37. Static Model Verification -- Heave Deflection

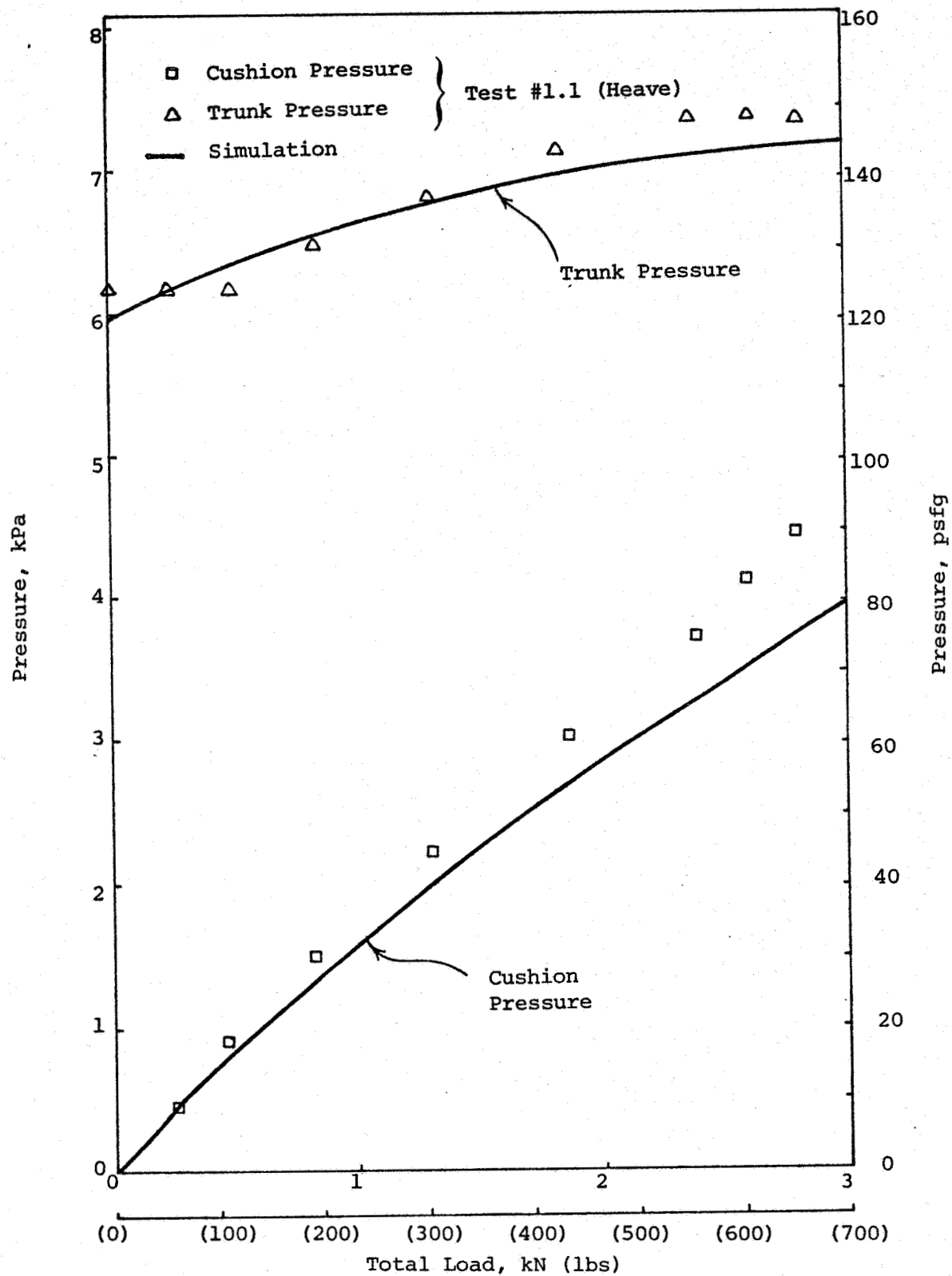


Figure 38. Static Model Verification -- Cushion and Trunk Pressure

shows the corresponding cushion and trunk pressures as the load is increased. The theory agrees reasonably well with experiment; the deflection and cushion pressure being within 10-15 percent from their test values, and trunk pressure predictions being even more accurate. Figure 39 shows the static pitch and roll angles as a function of the applied moment. The agreement here is not as good as in heave, with the analysis underestimating the angular deflection by 30-40 percent. The reason for this difference lies in the simplifications made in formulating the trunk model, in which the end segment is modeled as a frozen membrane due to the restraining effect of hoop tension. In fact, hoop tension drops off when the cushion is rotated in pitch or roll, so that the frozen approximation is less realistic in these modes than in heave because the reduced hoop restraint makes the trunk less stiff in angular deflection.

The Dynamic Model

Figures 40 and 41 compare the dynamic simulation results with the test records for the 15 cm (6") heave drop test. A 10 Hz low pass filter was included in the simulation to account for the test filter used to cut out noise. The first figure shows the dynamic trunk and cushion pressure history following the drop. As mentioned earlier, the first four vibration cycles have sufficient energy to bring about fan stall, which gives a characteristic dual peaked shape to the trunk and cushion pressure waveform. Then, after sufficient energy has been dissipated so that the fan backpressure does not exceed the stall threshold, the remainder of the vibration takes place without stall. The analysis predicts this behavior remarkably well, including the dual peaked waveform and the transition from stalled to non-stalled operation. The period of the stall cycle is also accurately predicted. Figure 41 compares theory and experiment for

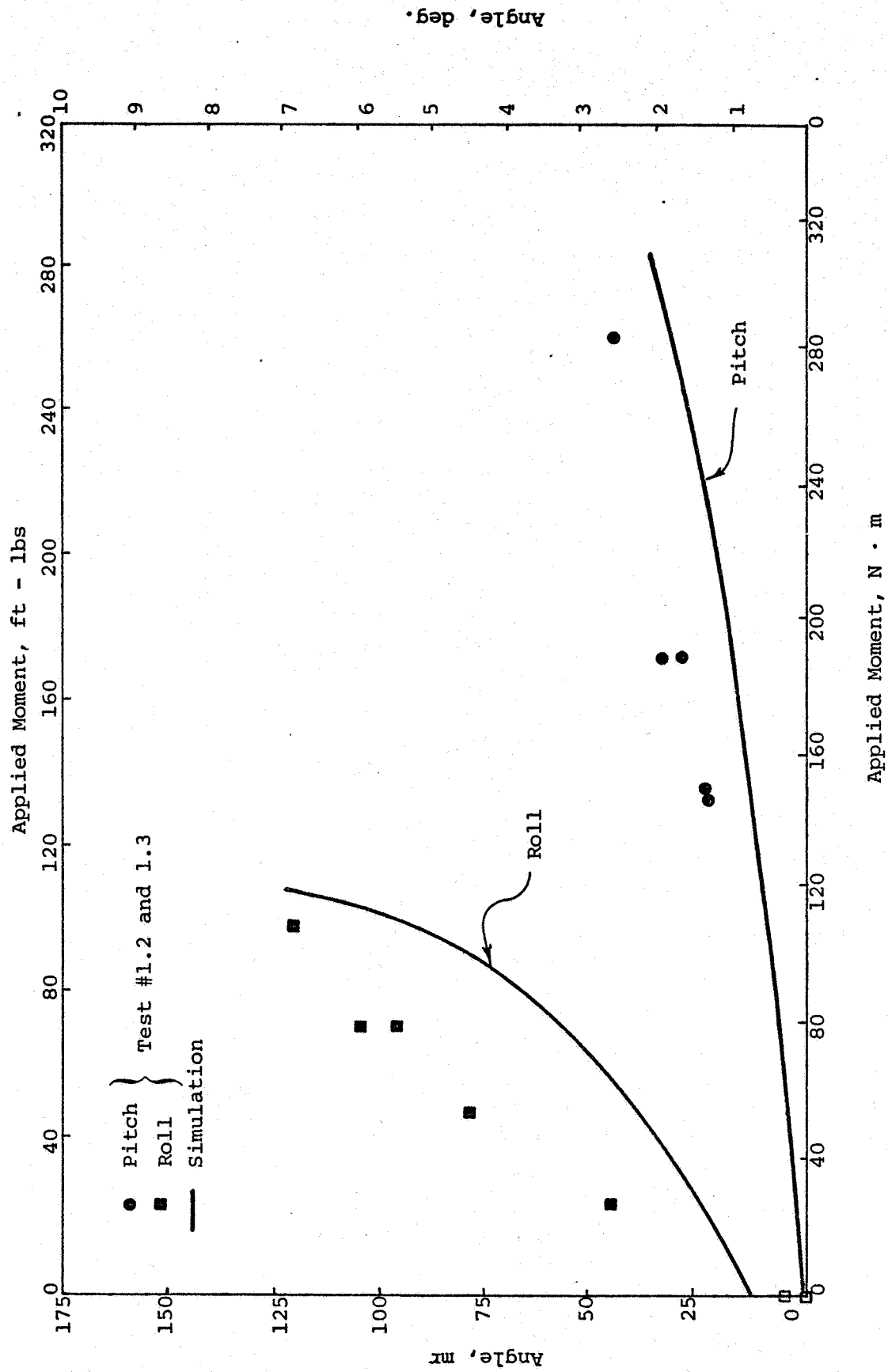


Figure 39. Static Model Verification -- Pitch and Roll Motion

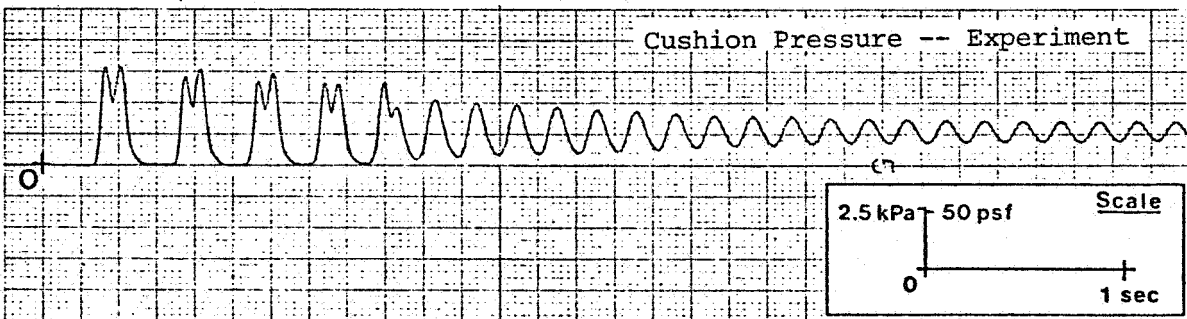
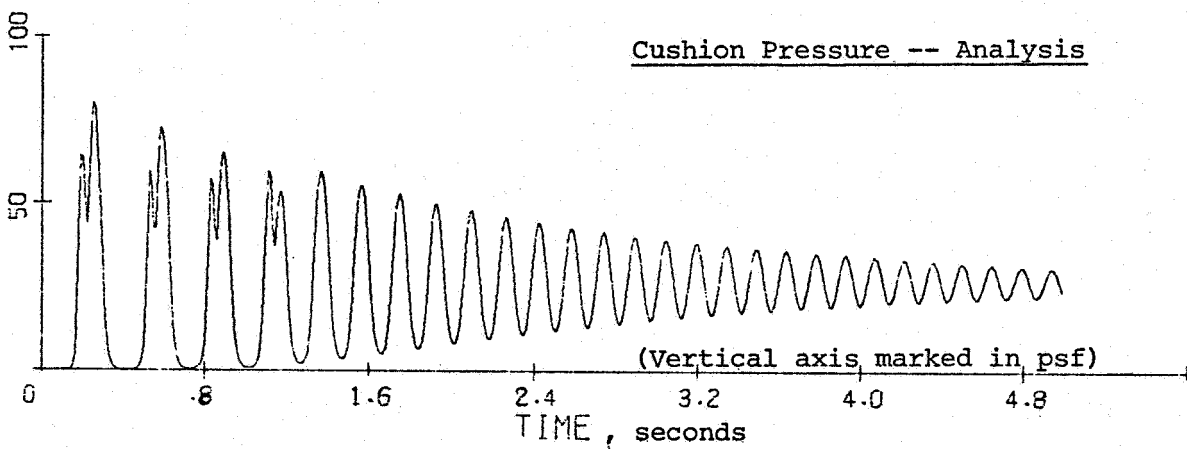
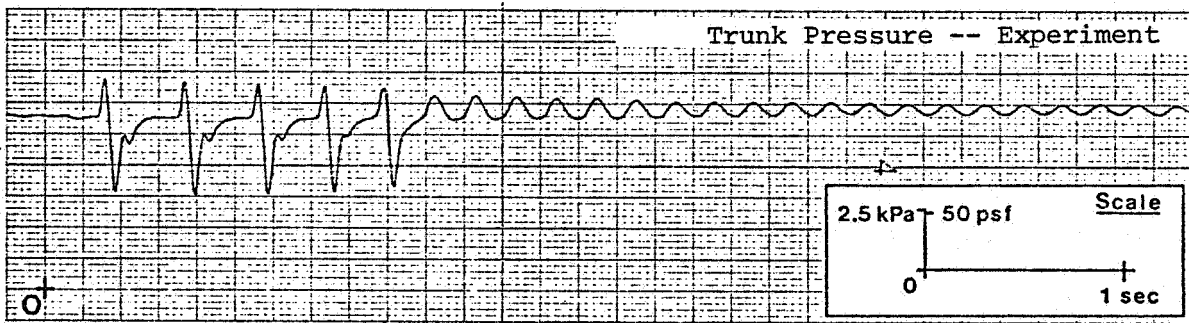
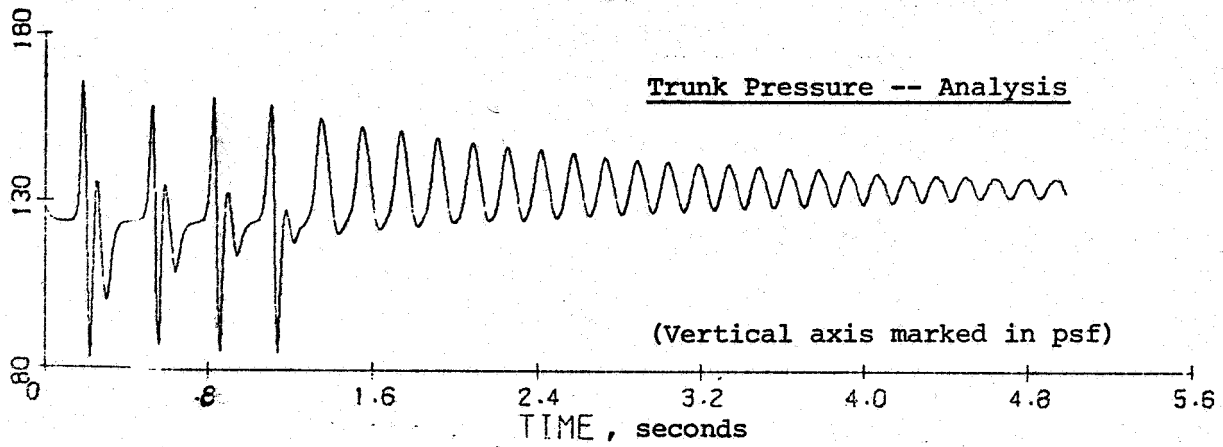


Figure 40. Dynamic Model Verification -- Trunk and Cushion Pressure

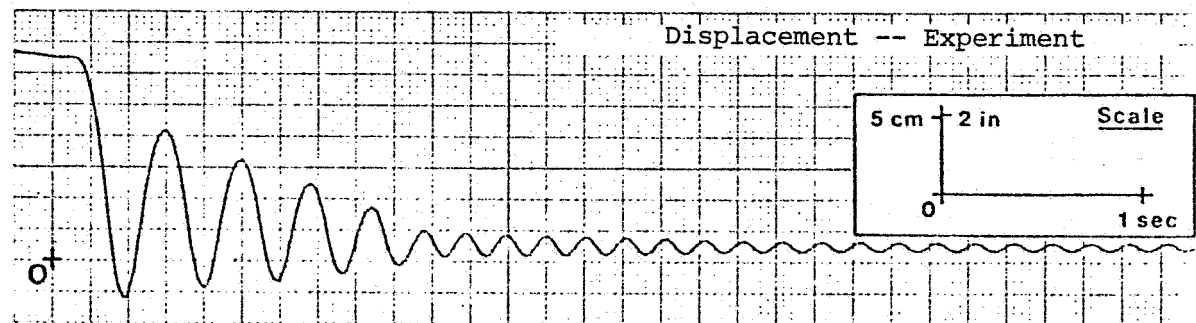
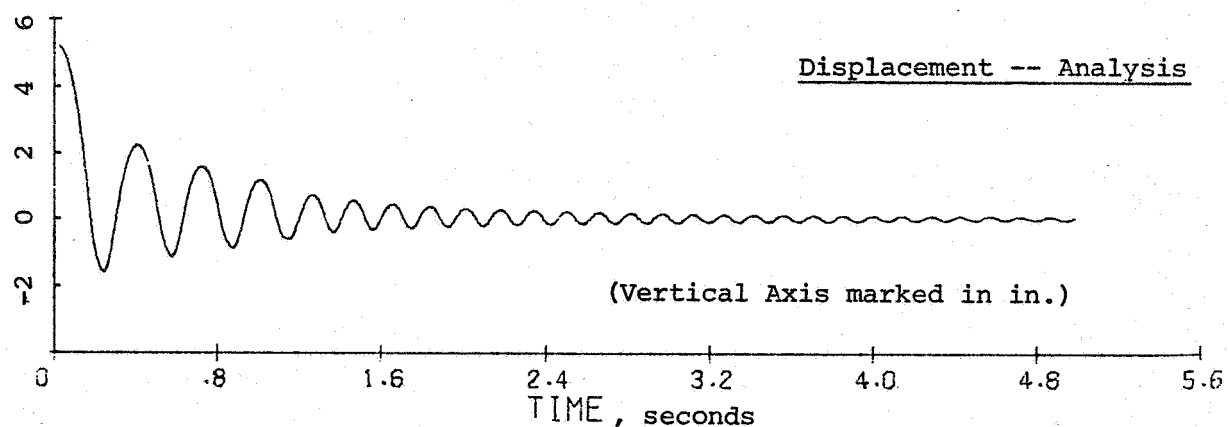
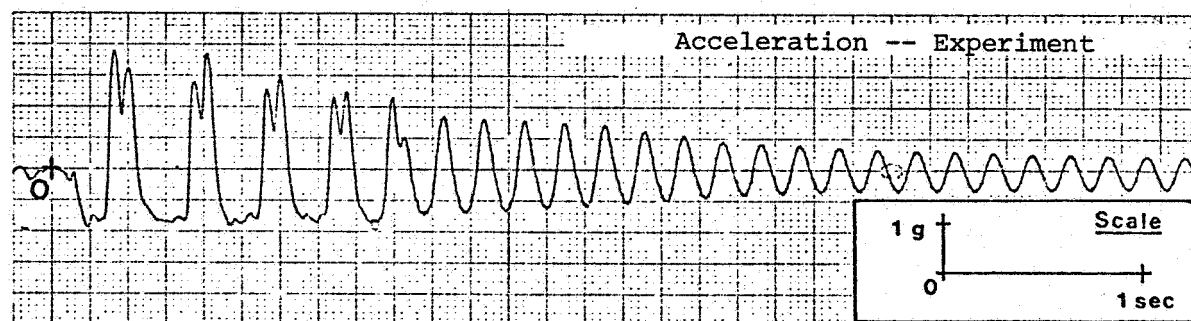
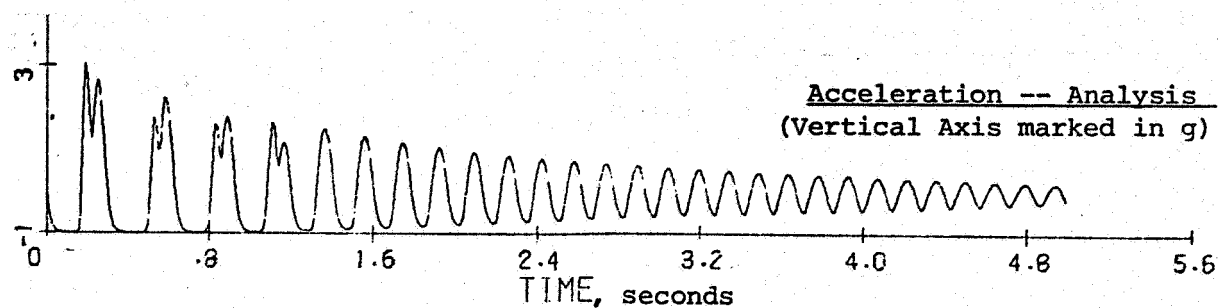
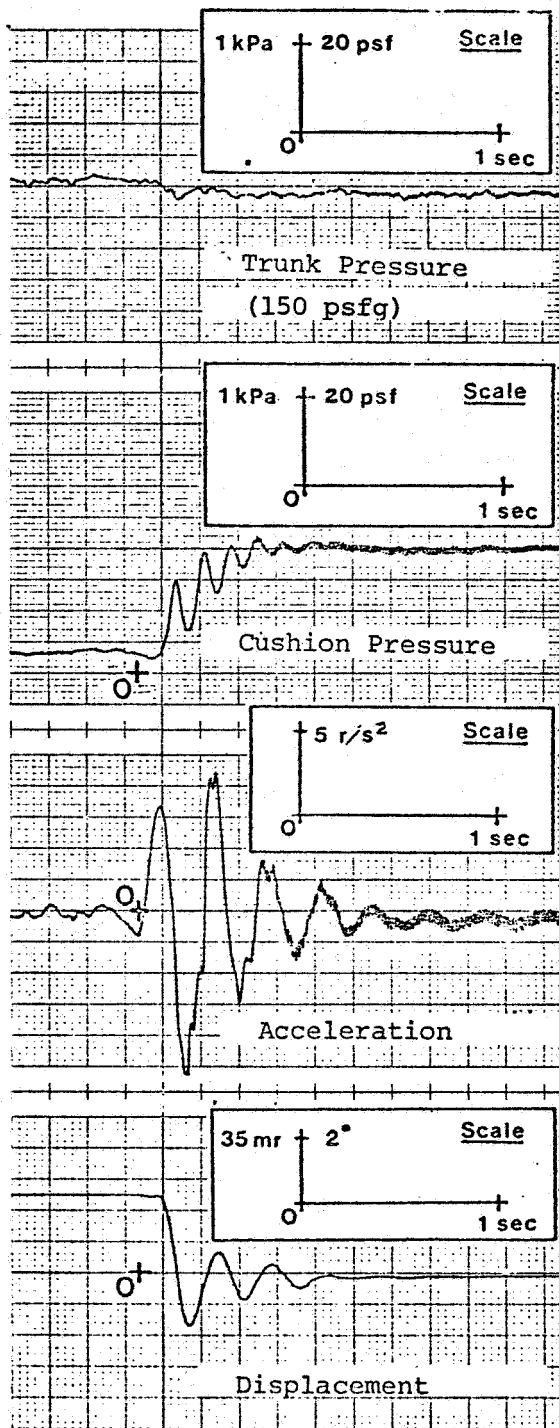


Figure 41. Dynamic Model Verification -- Heave
Acceleration and Displacement

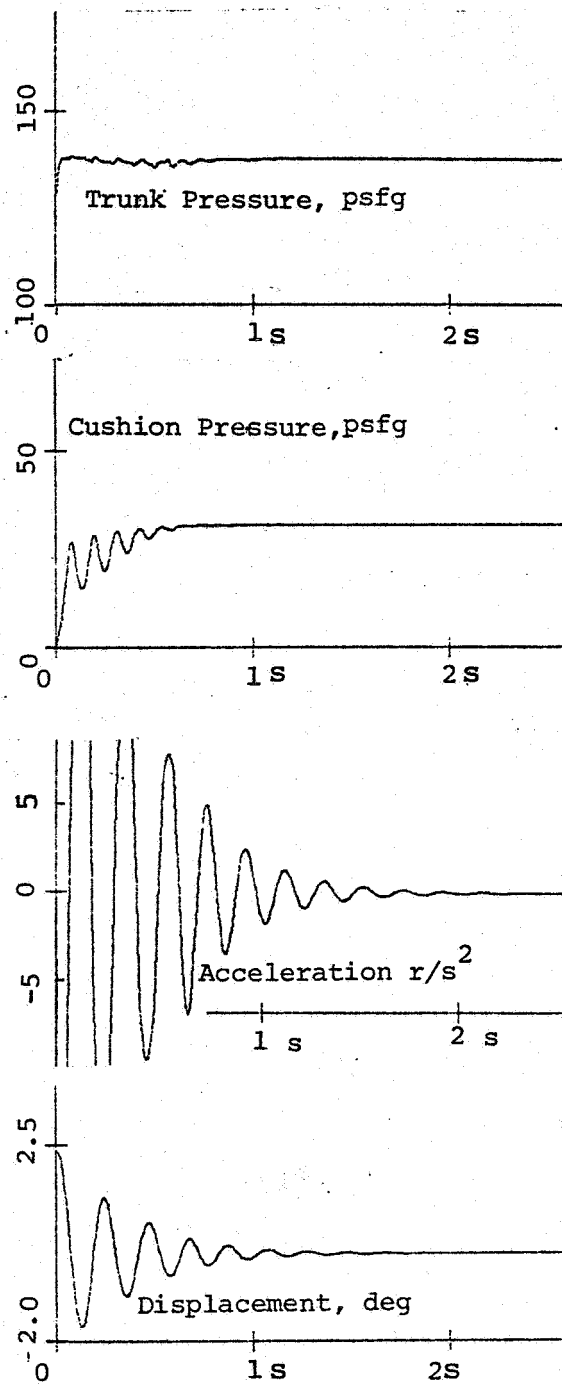
the heave acceleration and displacement. Here, too, the analysis agrees well with the test. The acceleration waveform is similar to that of the cushion pressure because a major part of the acceleration is caused by the cushion pressure acting over the cushion area. Thus, the acceleration waveform also exhibits the characteristic dual peaked stall cycles followed by the unstalled vibration. The heave displacement shows the reduction in damping between the initial and final cycles of the simulation. Like the experiment, the initial cycles are more damped because of the energy loss associated with fan stall, while the remainder of the vibration has much less damping and finally settles down to a low amplitude limit cycle oscillation.

Figure 42 shows the comparison between theory and experiment for the 41.4 mr (2.35°) pitch moment release test. The analytical results confirm that fan dynamics in pitch are insignificant because the trunk pressure (and hence fan back pressure) remains substantially constant. The simulation is able to predict the cushion pressure and displacement history very well, although peak acceleration estimates are higher than their measured values, apparently due to the simplifications inherent in the trunk damping model.

Although the complete time history of vibration provides very useful data on ACLS operation, the real value of the model as a design tool lies in its ability to determine the peak levels of the critical cushion parameters during touchdown and slideout. For instance, the maximum trunk pressure and dynamic trunk deflection form direct inputs to the layout and structural design of the trunk. Similarly, the impact value of heave acceleration and pitch rotation provide a very good initial indication of the smoothness and stability of the landing. It is therefore appropriate to evaluate the model based on its ability to predict the peak parameters of interest. Figures 43 to 47 show peak values and other key parameters as a function of the drop height (heave) or release angle (pitch and roll). Figure 43 shows the maximum impact deflection of the cushion (below equilibrium), which is



(a) Experiment



(b) Analysis

Figure 42. Dynamic Model Verification -- Pitch Mode

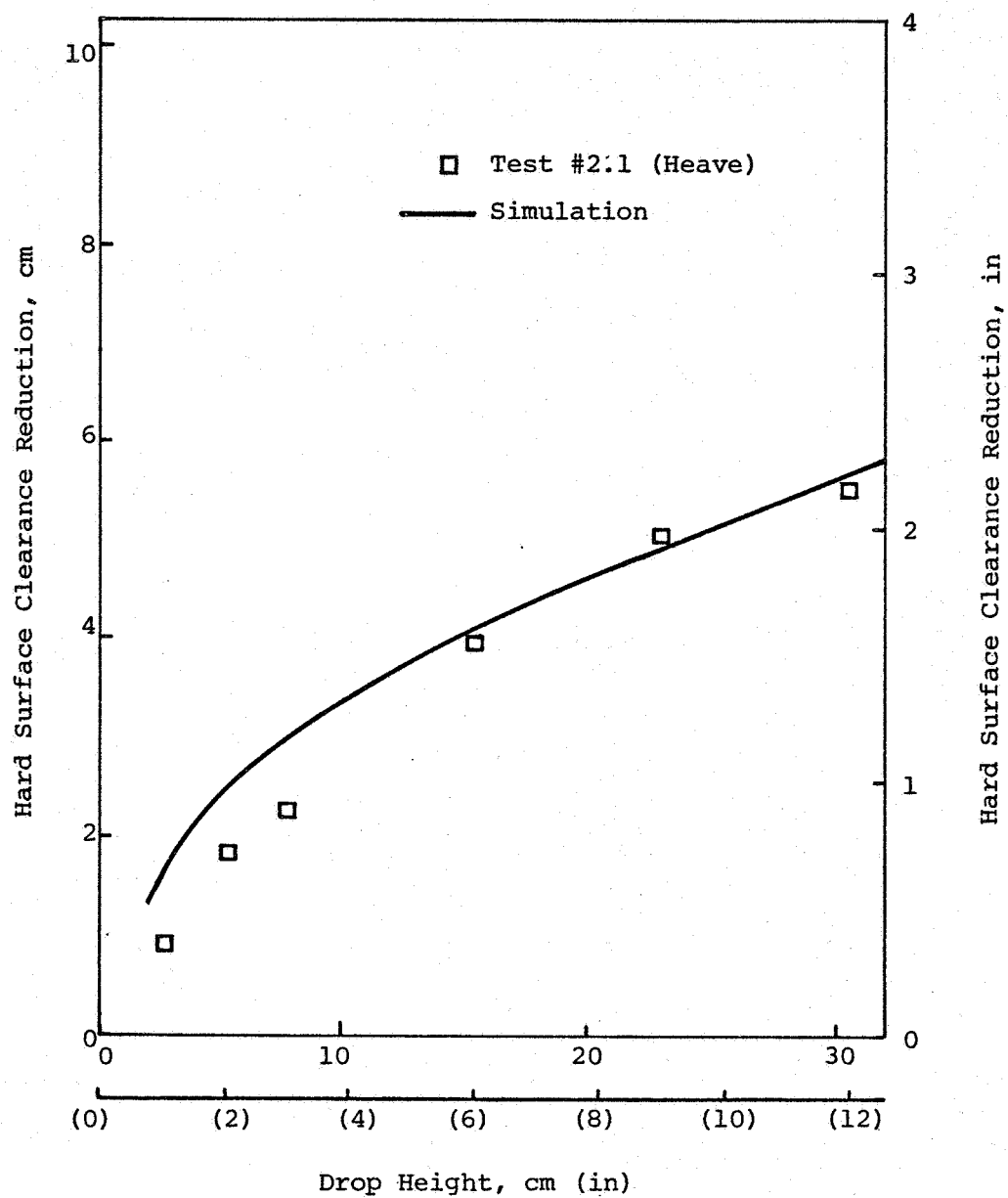


Figure 43. Maximum Reduction in Hard Surface Clearance

equivalent to the maximum reduction in hard surface clearance. When compared with the normal (static) clearance, this parameter will show how close the aircraft comes to hard surface contact during landing. As can be seen, agreement between theory and experiment is very good. Figure 44 shows the peak trunk and cushion pressure caused by impact. The simulation shows the right trends, although it tends to underestimate the cushion pressure by 10 - 25 percent. Figure 45 shows the peak acceleration and frequency associated with this acceleration (i.e., the stall frequency). The frequency is predicted quite closely -- within a margin of about 20 percent. The acceleration tends to be somewhat above the measured value, although the actual difference may be smaller than that shown because compliance in the members and joints of the aluminum cushion body (between the load points and the accelerometer mount) can reduce the measured acceleration to a level below that of a truly rigid structure. Figures 46 and 47 show the peak angular accelerations and natural frequencies in roll and pitch. The natural frequencies agree quite well; the theory predicting pitch frequency within a margin of 25 percent and roll frequency even more accurately. Roll frequency at the lower release angles is not shown because the test data was so damped that a complete cycle of oscillation was not available to estimate this parameter. Peak angular accelerations are not predicted as well as their corresponding frequencies, suggesting that the trunk damping model may need improvement. Unfortunately, as mentioned earlier, a more sophisticated damping model cannot be developed until a more advanced trunk deformation model is derived. Since the present trunk model gives good results for most of the other parameters, a major increase in simulation complexity may not be justified.

A summary of the prediction error bound for the various parameters discussed above is given in Table VI. The static model values represent the differences between theory and experiment for the steady-state condition. The dynamic model values (except frequency) represent the corresponding peak levels caused by impact

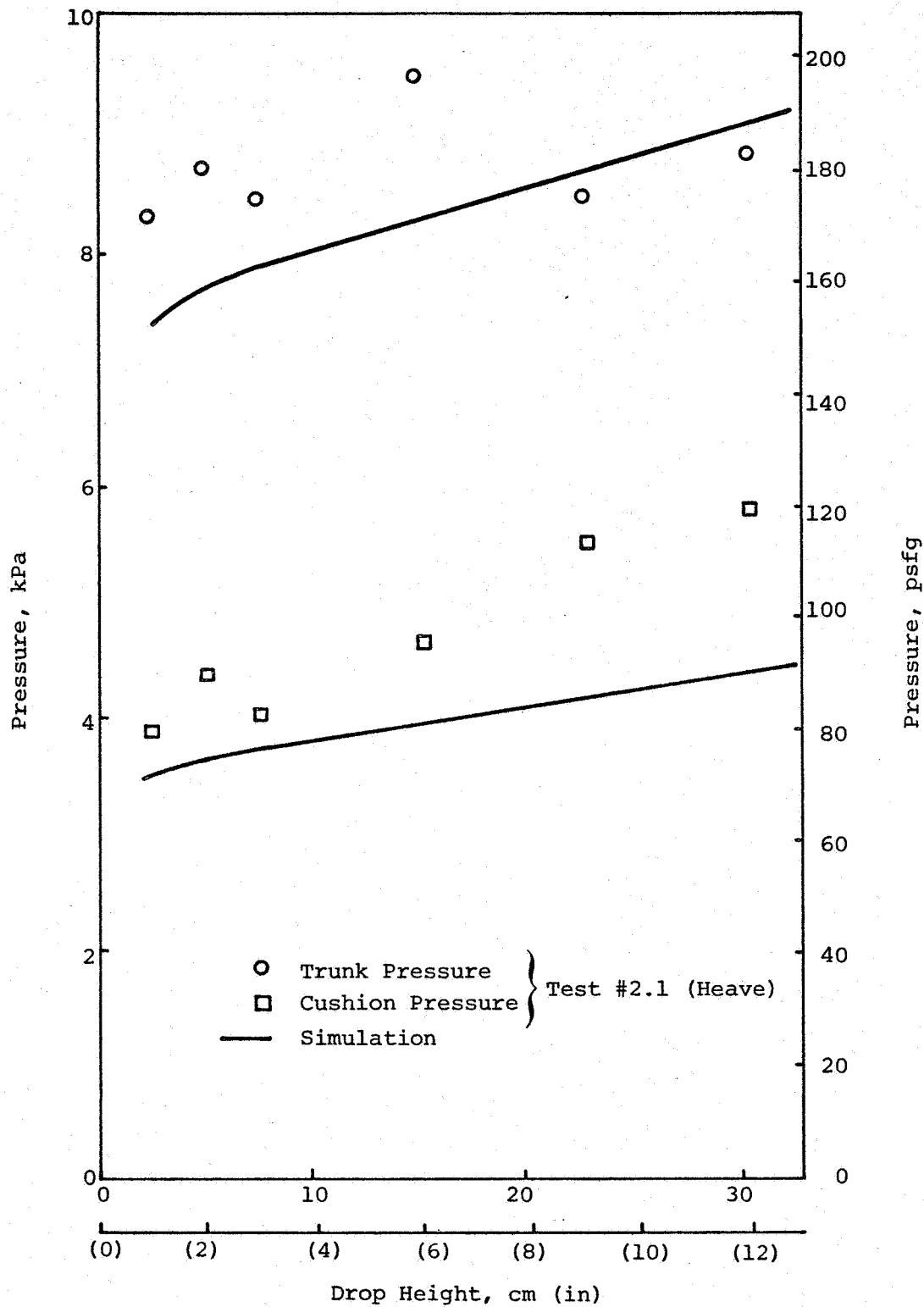


Figure 44. Peak Trunk and Cushion Pressure

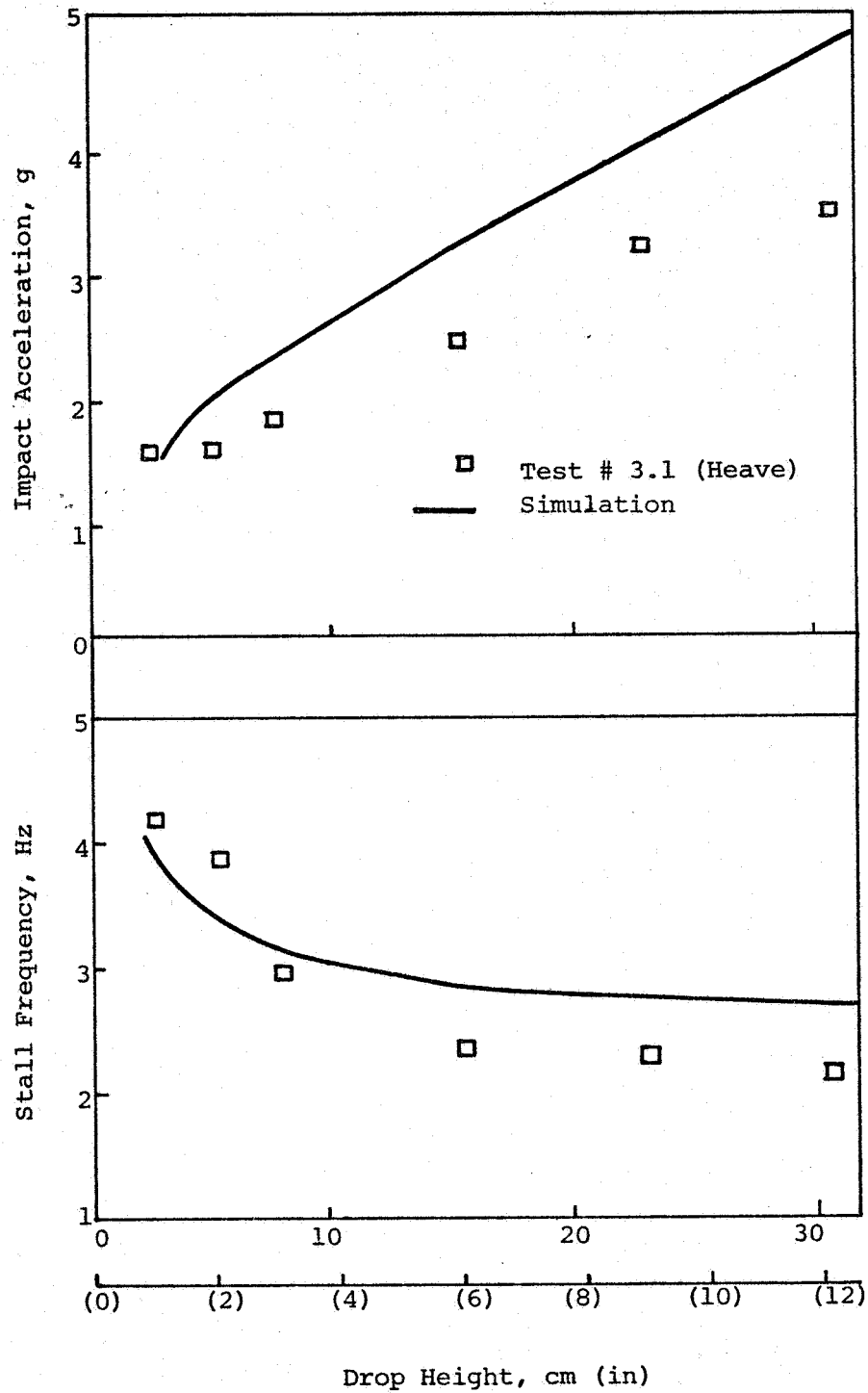


Figure 45. Impact Acceleration and Stall Frequency

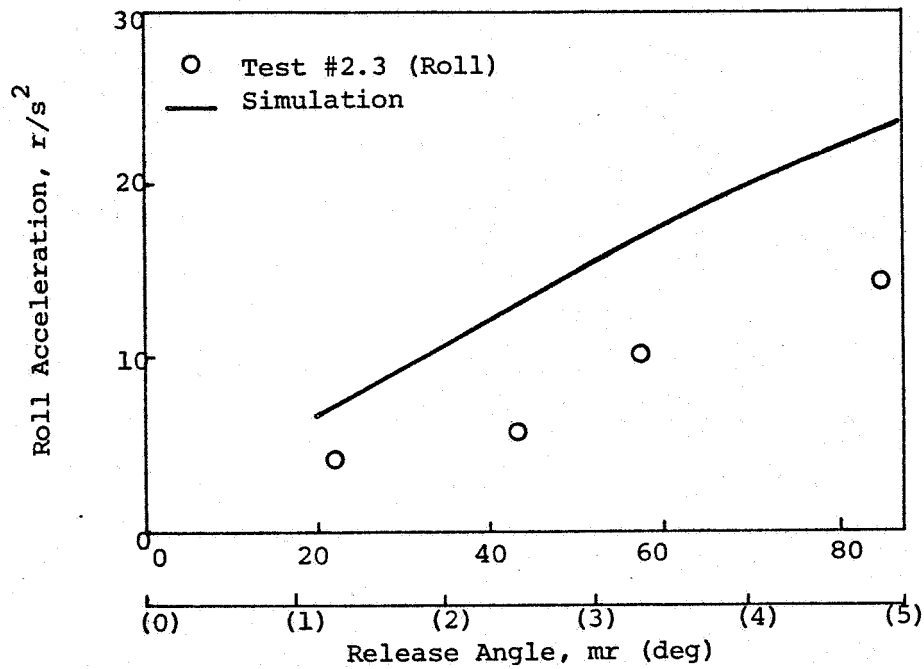
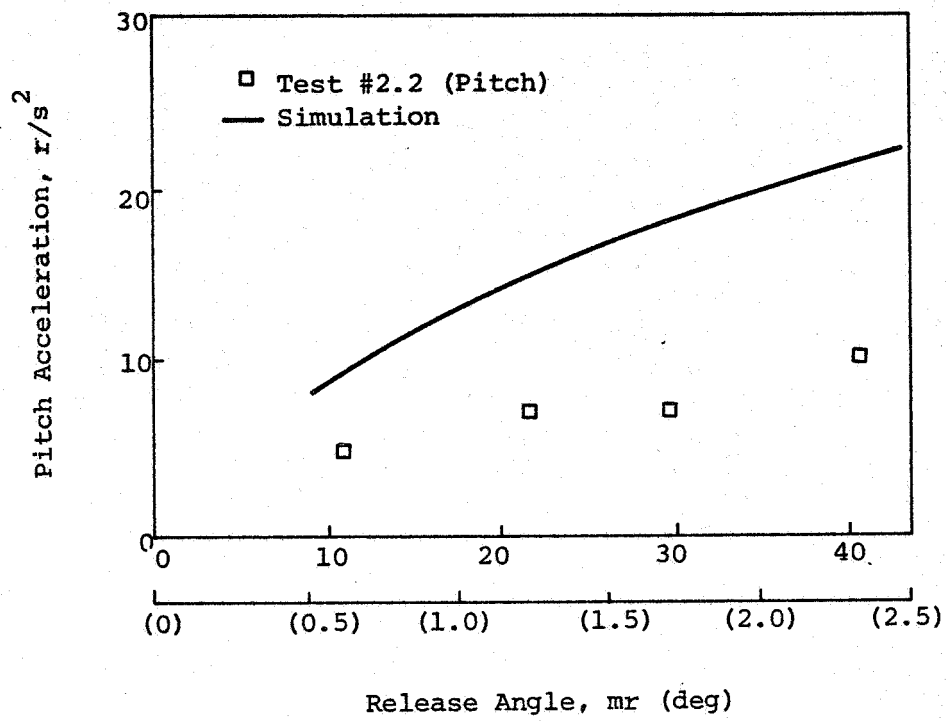


Figure 46. Peak Angular Acceleration

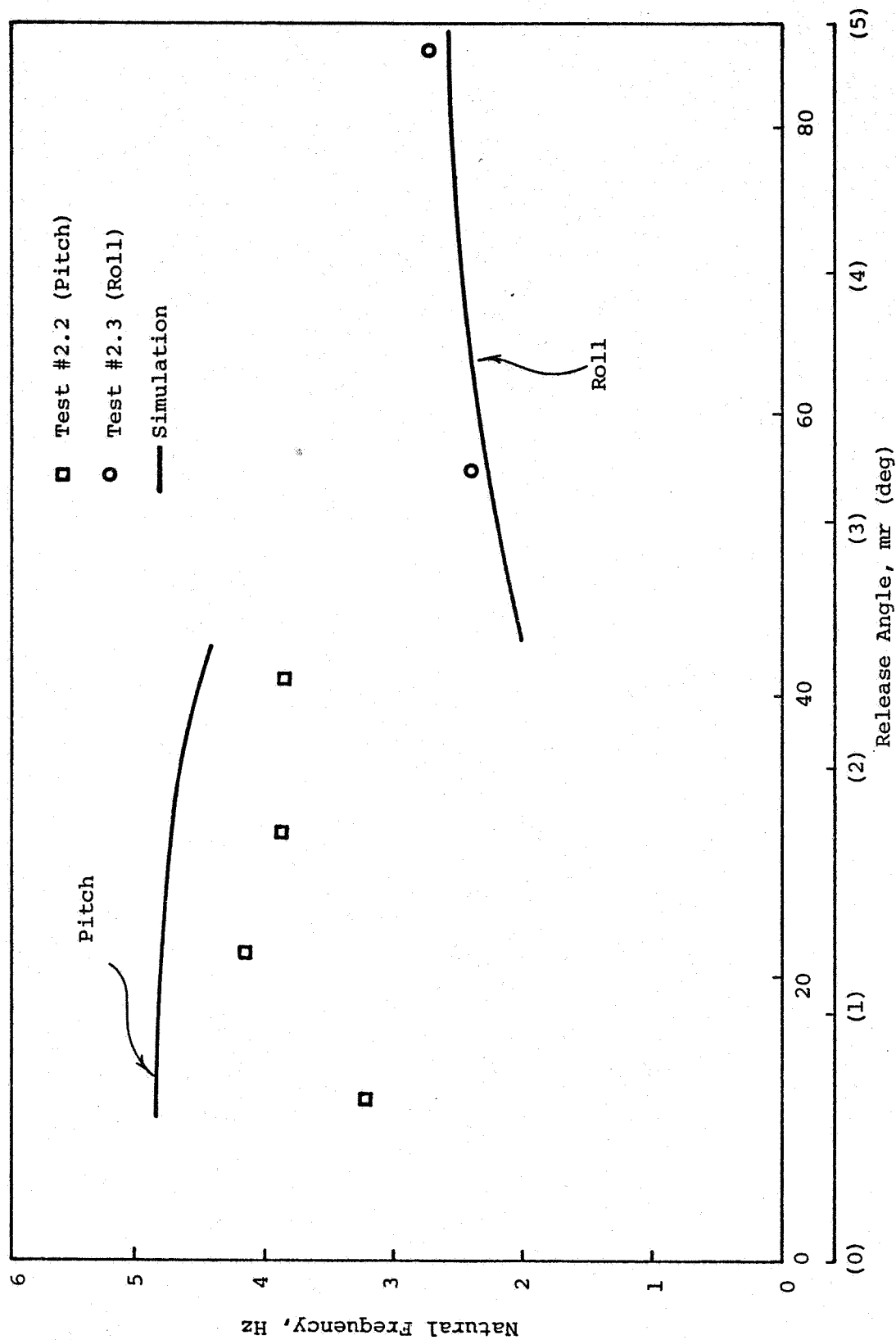


Figure 47. Pitch and Roll Natural Frequency

Table VI
Model Verification Summary

Parameter	Prediction Error Margin	
	Static Model	Dynamic Model
Clearance Reduction	10 - 15%	<5%
Trunk Pressure	<5%	10 - 15%
Cushion Pressure	10 - 15%	10 - 25%
Pitch Angle (Acceleration)	30 - 50%	(>50%)
Roll Angle (Acceleration)	20 - 50%	(40 - 50%)
Heave Acceleration	N/A	10 - 30%
Stall Frequency (Heave)	N/A	10 - 20%
Pitch Frequency	N/A	25%
Roll Frequency	N/A	<5%

(heave drop or moment release). With the exception of angular acceleration, which is difficult to predict because the trunk damping mechanism is very complex, the other outputs of the simulation compare well with test data; agreeing in most cases within a margin of 10-25 percent. The simulation therefore should serve as a valuable design and evaluation tool for improving ACLS performance.

MODEL USE

In this section, some typical simulations of landing and taxi dynamics are presented, to show the kinds of results that can be obtained when the analytical model is used to simulate a full-scale ACLS aircraft. Rather than choose an arbitrary configuration, the actual Buffalo aircraft was selected for simulation. The input data were collected from published reports (ref. 5) and through discussions with the XC-8A (Buffalo) Project Office at Wright-Patterson Air Force Base. Simulations were carried out to determine

- (a) The static characteristics of the ACLS
- (b) The touchdown and slideout dynamics for a 41 m/s (80 knots), 85 mm (5°) nose up landing with a sink rate of about 1 m/s (3.5 ft/sec).
- and (c) The behavior of the system during taxi at 3 m/s (6 knots) over an ungraded runway with a 23 cm (9 in) bump.

Although the Buffalo ACLS is powered by two independent air sources, the simulations were carried out assuming that the sources shared the load equally. Also, the effects of trunk elasticity (see footnote on page 84) were not taken into account. The equilibrium characteristics of the Buffalo obtained from the static model are shown in Table VII. The slight offset between the aircraft CG and geometric center of the cushion gives the aircraft

Table VII

PREDICTED EQUILIBRIUM FOR BUFFALO ACLS

STATIC EQUILIBRIUM CONDITIONS

HEIGHT OF CG	=	9.951	FT
PITCH ANGLE	=	.716	DEGREES
ROLL ANGLE	=	0.000	DEGREES
CUSHION PERIMETER	=	59.606	FT
CUSHION VOLUME	=	245.772	CU FT
TRUNK VOLUME	=	1041.345	CU FT
AIR GAP AREA	=	5.291	SQ FT
CUSHION AREA	=	192.199	SQ FT
GROUND CONTACT AREA	=	37.194	SQ FT
ORIFICE AREA TRUNK-ATMOS	=	.194	SQ FT
ORIFICE AREA TRUNK-CUSH	=	4.328	SQ FT
CUSHION PRESSURE	=	166.057	PSFG
TRUNK PRESSURE	=	360.598	PSFG
PLENUM PRESSURE	=	370.982	PSFG
TOTAL AIR FLOW	=	1723.953	CU FT/SEC
TOTAL CUSHION FLOW	=	1592.652	CU FT/SEC
FLOW PLENUM TO CUSHION	=	0.000	CU FT/SEC
FLOW PLENUM TO TRUNK	=	1723.953	CU FT/SEC
FLOW TRUNK TO CUSHION	=	1592.652	CU FT/SEC
FLOW TRUNK TO ATMOSPHERE	=	131.301	CU FT/SEC
FLOW PLENUM TO ATMOSPHERE	=	0.000	CU FT/SEC
FAN STALL MARGIN	=	22.144	PERCENT
THEORETICAL FAN POWER	=	1162.827	HP

a slight nose-up inclination at rest. The theoretical fan power is the pumping power that would be required by an ideal fan. The actual power will thus be higher than this value due to losses in the fan. The fan stall margin is the maximum percent increase in backpressure that the fan can experience without stalling. Figure 48 shows the static deflection of the Buffalo as the load and moment are changed. The main conclusion emerging from the static analysis is that the aircraft has very low stiffness in roll -- a conclusion that was confirmed through the tests, and which led to a wingtip skid retrofit to increase roll stability. The reason for the shape of the roll deflection curve can be understood from the trunk model. When a roll moment is applied, the first effect is to reduce the air gap under one of the side trunk segments, while increasing the gap under the other. In this part of the operating characteristics the cushion does not generate any appreciable restoring moment, as shown by the initial vertical part of the curve. Then, as the gap under the lower side trunk segment becomes very small, the segment begins to bow outwards and subsequently touch the ground, thus increasing the restoring moment. At even larger angles, the cushion pressure begins to drop because the higher side trunk segment is well off the ground, thereby venting the cushion. In this operating region, the roll stiffness begins to reduce again as shown by the curve.

The landing dynamics of the system are shown in Figure 49. From an initial nose-up attitude, the touchdown pitch moment causes the aircraft to pitch forward to a maximum nose-down pitch angle of 45 mr ($2\frac{1}{2}^\circ$). The pitch disturbance then dies out during slideout and braking. However, when the aircraft comes to a stop (about 9 seconds after touchdown), the braking force (and moment) disappear and the aircraft undergoes a second pitch-heave vibration, coming to rest with the final nose-up attitude as predicted by the static model. From Figure 49, the maximum increase in trunk pressure during landing is found to be $(420-360)/360 = 17$ percent. Since the trunk pressure is practically equal to the

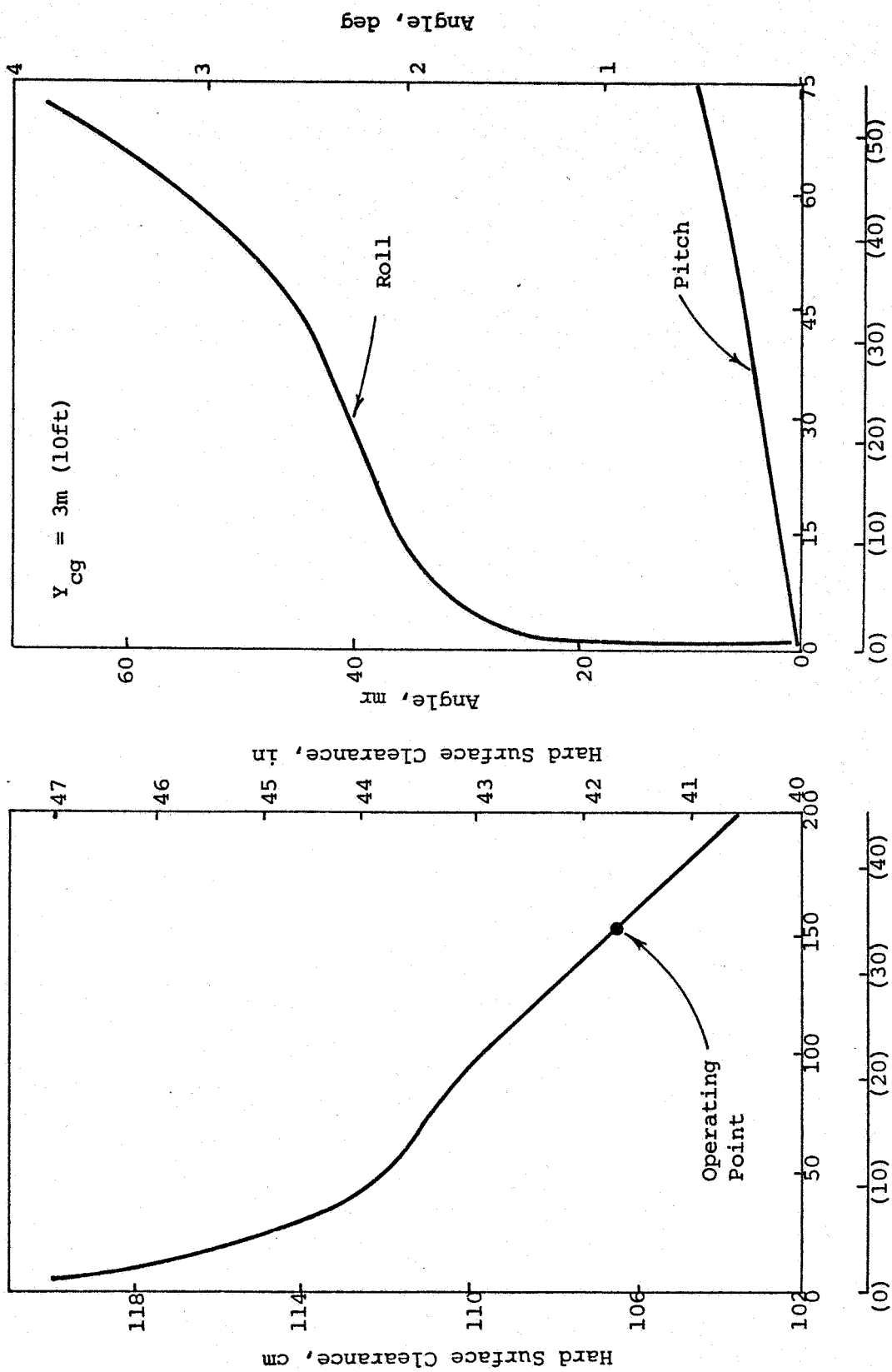


Figure 48. Static Characteristics of Buffalo ACLS

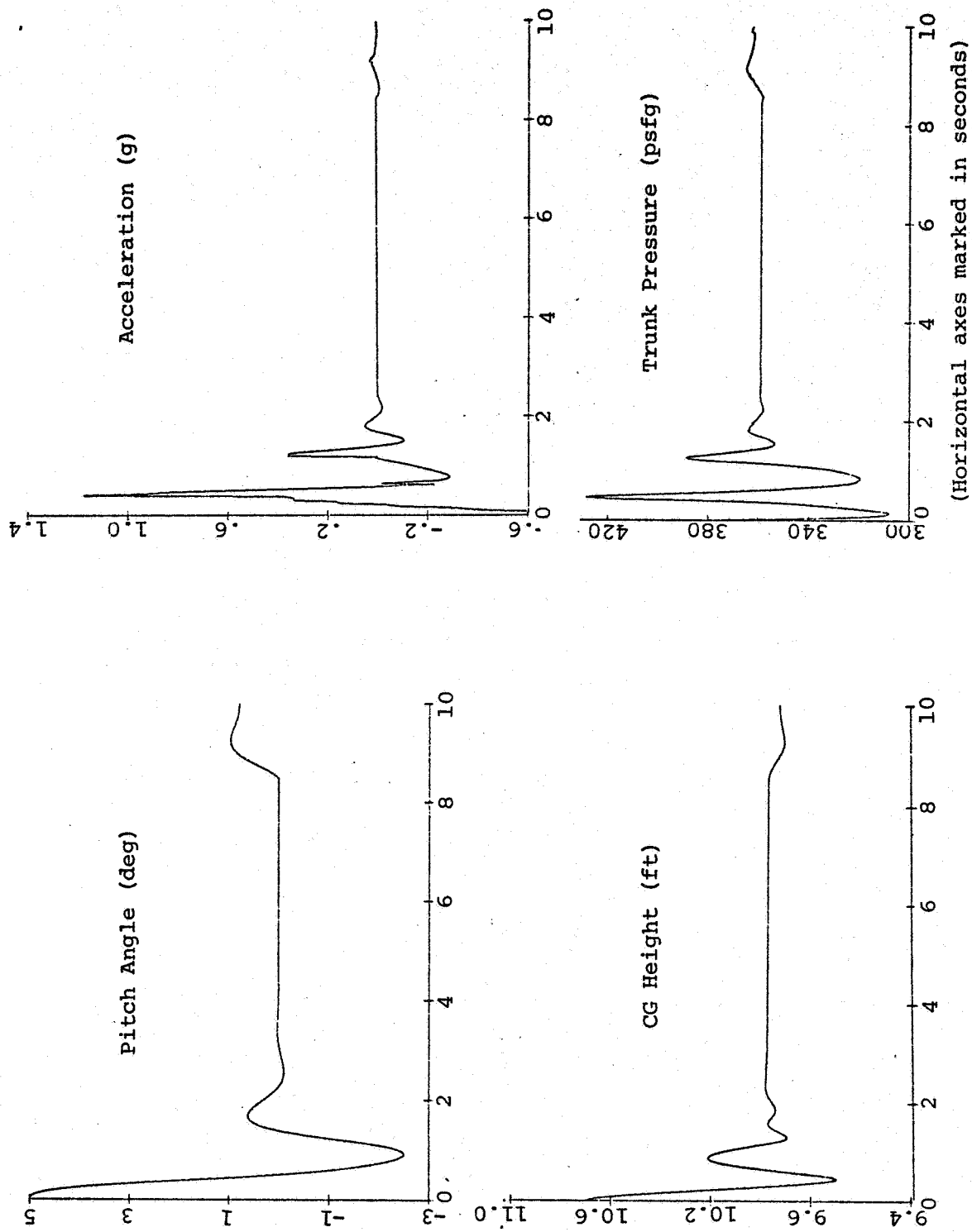


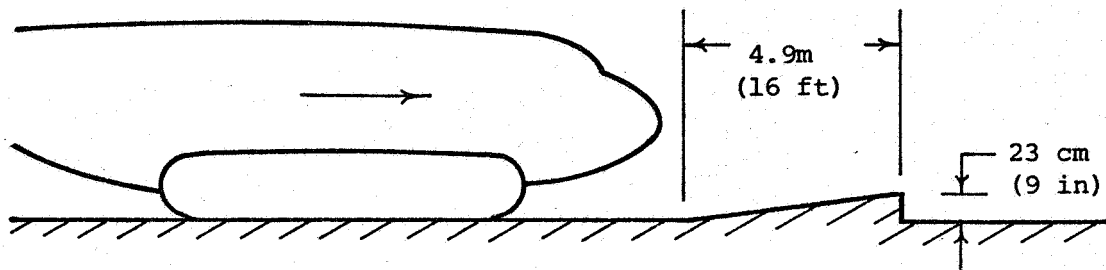
Figure 49. Landing Dynamics of Buffalo ACLS

fan backpressure, it can be concluded that fan stall will not occur because the stall margin of 22 percent is not exceeded.

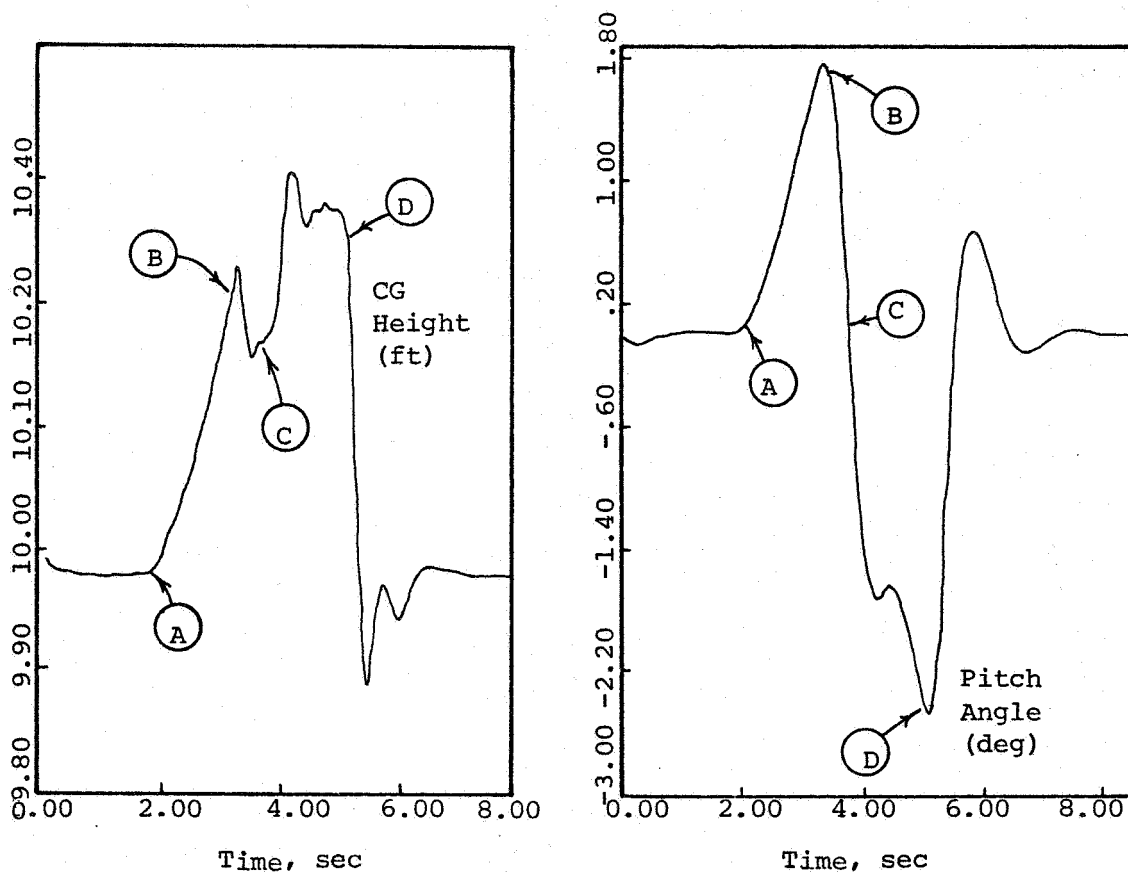
The taxi dynamics of the system are evaluated by considering the case shown in Figure 50a, in which the aircraft crosses a ramp-like irregularity. This type of irregularity provides both gradual excitation and a sudden change. The irregularity length was chosen slightly smaller than the cushion length so that, for some duration, the entire obstacle would be contained entirely within the cushion. The heave and pitch motion response is shown in Figure 50b. Point A marks the spot where the leading edge of the cushion first touches the ramp. This causes the nose to pitch up and the aircraft CG to rise. Because the excitation is gradual, the change is relatively smooth. At point B, the front of the cushion goes over the edge of the ramp, so there is a sudden change in the pitch angle as the nose begins to drop down. The CG of the system also drops as the cushion pressure is reduced by the sudden gap area increase at the front. At point C, the trailing edge of the cushion begins to move up the ramp, thus raising the system CG but continuing to increase the nose-down pitch angle. Finally, at point D, the back of the cushion goes over the edge of the ramp thus causing a sudden drop in CG elevation and restoring the aircraft to its normal pitch orientation. When crossing the obstacle, the aircraft CG rises by a maximum of about one-half the obstacle height, and the peak (nose down) pitch angle reaches a value of about $45 \text{ mr } (2 \frac{1}{2}^\circ)$.

The main conclusions that emerge from the Buffalo simulations are as follows.

- The aircraft will have poor roll stability.
- In equilibrium, the aircraft will maintain a slight nose-up attitude.



(a) Taxi Over Ramp



(b) Heave and Pitch Response

Figure 50. Taxi Dynamics of Buffalo ACLS

- The theoretical (minimum) fan power (both fans combined) will be about 800 kW (1000 hp).
- The maximum (nose-down) pitch angle during landing will be about 45 mr ($2\frac{1}{2}^{\circ}$).
- Under normal landing conditions, fan stall will not occur.
- Peak landing accelerations will be on the order of 1 g
- The trunk will have to withstand peak pressures of about 20 kPa (3 psi).
- Although taxi behavior depends on the field roughness, the satisfactory negotiation of a 23 cm (9 in.) bump suggests that the aircraft will be able to operate from rough fields.

CONCLUSION

A heave-pitch-roll analysis and computer simulation has been developed to evaluate the landing and taxi dynamics of an ACLS aircraft. Initial results have shown that fan dynamics and stall have a major effect on system performance. Comparison with zero forward speed test data shows that the model can predict most of the key system parameters within a margin of 10-25 percent.

The simulation can now be used as an analytical tool, to evaluate existing configurations and develop new designs that overcome current shortcomings such as low angular stiffness and poor stability. Concurrently with design development, additional test data should be obtained in two important areas, to complete the verification of the analysis. These areas are:

- The stall and backflow characteristics of ACLS fans
- The effects of forward speed on ACLS dynamics

When this work is complete, NASA will have available the technology base needed to implement practical and efficient ACLS for any aircraft application of interest.

APPENDIX
THE EQUATIONS OF THE HEAVE-PITCH-ROLL MODEL

Symbol List

A

- a - Horizontal distance between inner and outer trunk attachment points
- A - Area
- A_{af} - Area of fan inlet orifice
- A_c - Cushion area
- A_{cn} - Area of trunk in ground contact
- A_{dd} - Area of duct connecting fan to plenum
- A_{df} - Crossectional area of fan flow passages
- A_g - Orifice area, cushion to atmosphere (gap area)
- A_h - Area of trunk hole
- A_{pa} - Orifice area, plenum to atmosphere
- A_{pc} - Orifice area, plenum to cushion
- A_{ph} - Projected heave area of aircraft
- A_{pt} - Orifice area, plenum to trunk
- A_t - Trunk crossectional area
- A_{ta} - Orifice area, trunk to atmosphere
- A_{tc} - Orifice area, trunk to cushion
- A_u - Upstream orifice area
- A_v - Relief valve area
- A_1 to A_{11} - Trunk crossectional area components

B

b - Vertical distance between inner and outer trunk attachment points

b_{11} }
 b_{12} }
 b_{13} } Euler angle transformation factors
 b_{21} }
 b_{22} }
 b_{23} }

B_e - Damping coefficient of trunk segment

C

C_{af} - Fan inlet orifice discharge coefficient

C_c - X axis distance between aircraft CG and cushion center

C_d - Drag coefficient for heave motion of aircraft

C_{du} - Discharge coefficient of upstream orifice

C_{fx} - X axis distance between aerodynamic drag center and aircraft CG

C_{fz} - Z-axis distance between aerodynamic drag center and aircraft CG

C_g - Discharge coefficient for cushion to atmosphere flow

C_{pa} - Discharge coefficient for plenum to atmosphere flow

C_{pc} - Discharge coefficient for plenum to cushion flow

C_{pt} - Discharge coefficient for plenum to trunk flow

C_{ta} - Discharge coefficient for trunk to atmosphere flow

C_{tc} - Discharge coefficient for trunk to cushion flow

C_v - Relief valve discharge coefficient

D

d - Distance between inner trunk attachment points

dx - Width of straight trunk segment

D_c - Trunk damping constant

F

F - Force

F_{cn} - Equilibrium vertical cushion force

F_{cp} - Force on aircraft due to cushion pressure

F_{ct} - Trunk damping force along vehicle y-axis

F_{cy} - Total force along vehicle y-axis

F_{df} - Aerodynamic drag force along vehicle y-axis

F_{ey} - Total force along inertial y-axis

F_f - Z-axis distance between aircraft CG and center of cushion

F_{tp} - Force on aircraft due to trunk contact pressure

F_x - Force acting along inertial X-axis

F_y - ACLS force in the inertial vertical direction

F_z - Force acting along inertial Z-axis

G

g - Gravity acceleration

G_g - y-axis distance between aircraft CG and cushion center

H

- \vec{H} - Angular momentum vector about the CG
- H_w - Cushion width
- H_{wi} - Cushion width at no load
- H_x - Angular momentum component along vehicle x-axis
- H_y - Vertical distance between hard surface and lowest point of trunk
- H_y - Angular momentum component along vehicle y-axis
- H_{yi} - Value of H_y at no load
- H_z - Angular momentum component along vehicle z-axis

I

- $[I]$ - Inertia matrix
- I_f - Inertance of air in fan ducts
- I_s - Segment location identification number
- I_t - Segment type number
- I_x - Moment of inertia of aircraft about the vehicle x-axis
- I_y - Moment of inertia of aircraft about the vehicle y-axis
- I_z - Moment of inertia of aircraft about the vehicle z-axis
- $\left. \begin{array}{l} I_{xy} \\ I_{yz} \\ I_{zx} \end{array} \right\}$ Cross products of inertia of the aircraft with respect to the x, y and z axes of the vehicle

K

- k - Polytropic exponent for air expansion
- k_v - Relief valve spring stiffness
- K - Trunk height design constant

L

- ℓ - Perimeter of trunk crosssection
- ℓ_c - Perimeter of the ground contact zone for each trunk segment
- ℓ_{dd} - Length of duct between fan and plenum
- ℓ_{df} - Length of fan flow passages
- ℓ_p - Peripheral distance from inner trunk attachment point to first row of trunk holes
- ℓ_1 - Peripheral length of trunk sector (cushion side)
- ℓ_2 - Peripheral length of trunk sector (atmosphere side)
- ℓ_4 - Distance of hard surface from ground datum
- L_s - Length of straight segment of cushion

M

- m_v - Mass of pressure relief valve
- M - Half the number of segments in each straight section of the trunk
- M_a - Aircraft mass

N

- N - Half the number of segments in each curved section of the trunk
- N_h - Number of trunk orifices per row
- N_r - Number of rows of trunk orifices

N_v - Number of relief valves

N_1 - Number of trunk orifice rows communicating with cushion

N_2 - Number of trunk orifice rows communicating with atmosphere

P

P_a - Atmospheric pressure

P_{af} - Pressure drop across fan upstream orifice

P_{av} - Average contact pressure

P_c - Cushion pressure

P_f - Static pressure rise across fan

P_p - Plenum pressure

P_{pb} - Relief valve preload pressure

P_t - Trunk pressure

Q

Q - Flow

Q_{ca} - Flow from cushion to atmosphere

Q_f - Fan flow

Q_{fp} - Flow from fan to plenum

Q_{fx} - Static fan flow

Q_{pa} - Flow from plenum to atmosphere

Q_{pc} - Flow from plenum to cushion

Q_{pt} - Flow from plenum to trunk

Q_{ta} - Flow from trunk to atmosphere

Q_{tc} - Flow from trunk to cushion

Q_v - Flow through pressure relief valve

R

- r - Radius
- R - Radius of equivalent circular crosssection trunk
- R_1 - Radius of trunk sector (cushion side)
- R_2 - Radius of trunk sector (atmosphere side)

S

- S - Peripheral length of cushion
- S_h - Spacing between the rows of trunk holes
- S_v - Relief valve peripheral length

T

- t - Time
- T - Hoop tension in trunk
- \vec{T} - Torque vector about the aircraft CG
- T_{cpx} - Cushion pressure torque about vehicle x-axis
- T_{cpz} - Cushion pressure torque about vehicle z-axis
- T_{dfx} - Aerodynamic torque about vehicle x-axis
- T_{dfz} - Torque due to aerodynamic drag
- T_{fz} - Torque due to trunk contact friction
- T_{nx} - Cushion and contact pressure torque about vehicle x-axis
- T_{nz} - Cushion and contact pressure torque about vehicle z-axis
- T_{tpx} - Trunk contact pressure torque about vehicle x-axis
- T_{tpz} - Trunk contact pressure torque about vehicle z-axis

T_{tx} - Trunk damping torque about vehicle x-axis
 T_{tz} - Trunk damping torque about vehicle z-axis
 T_x - Torque component about vehicle x-axis
 T_y - Torque component about vehicle y-axis
 T_z - Torque component about vehicle z-axis

U

\vec{u}_i - Unit vector along intermediate axis during Euler angle rotation
 \vec{u}_Y - Unit vector along inertial Y-axis
 $\left. \begin{matrix} \vec{u}_x \\ \vec{u}_y \\ \vec{u}_z \end{matrix} \right\}$ Unit vectors along vehicle x, y, and z axes

V

V - Heave velocity component of aircraft
 V_c - Cushion volume
 V_p - Plenum volume
 V_t - Trunk volume
 V_t - Vertical velocity of trunk segment
 V_r - Velocity of trunk (contact) segment center relative to aircraft CG

X

x - Vehicle roll axis
 x_a - Relief valve stop clearance
 x_v - Relief valve motion

- X - Inertial roll axis
- X_{cg} - Aircraft CG motion in the inertial forward direction
- X_{ch} - Longitudinal distance between center of pressure and cushion center
- X_{cx} - Longitudinal distance between segment center and cushion center
- X_e - Horizontal distance from centroid of trunk crosssectional area to inner trunk attachment point
- X_g - Ground profile location coordinates
- X_t - X-axis distance between the center of the trunk contact area segment and the center of the cushion
- X_{tk} - Lateral distance between center of trunk contact pressure and cushion center
- X_1 to X_{12} }
 X_{cr} } X coordinates of centroids of trunk cross-
 X_b, X_e, X_{er} } sectional area components

Y

- y - Vehicle yaw axis
- Y - Inertial yaw axis
- Y_{cg} - Aircraft CG displacement in the inertial vertical direction
- Y_g - Ground profile height coordinate
- Y_{gh} - Hard surface clearance

Z

- z - Vehicle pitch axis
- Z - Inertial pitch axis
- z_{cg} - Distance along inertial Z axis
- z_{ch} - Lateral distance between center of cushion pressure and cushion center
- z_{cx} - Lateral distance between segment center and cushion center
- z_g - Ground profile location coordinate
- z_t - z -axis distance between the center of the trunk contact segment and the center of the cushion
- z_{tk} - Lateral distance between center of trunk contact pressure and cushion center
- z_v - Relief valve damping constant

Greek

- α - Fan curve polynomial coefficient
- β - Angle subtended by curved trunk segment
- δ - Angle between cushion axis and curved trunk segment
- δ_e - End trunk excursion
- δ_s - Side trunk excursion
- ρ - Air density
- θ - Roll angle about vehicle x -axis
- θ_e - Eulerian roll angle
- μ - ACLS braking coefficient
- ϕ - Pitch angle about vehicle z -axis
- ϕ_e - Eulerian pitch angle

ψ - Yaw angle about vehicle y-axis

ψ_e - Eulerian yaw angle

ω - Angular velocity

$\left. \begin{array}{l} \phi_1 \\ \phi_2 \\ \phi_3 \\ \phi_4 \end{array} \right\}$ Angles subtended by trunk sectors

Other

$(\dot{})$ - Velocity

$(\ddot{})$ - Acceleration

(i) - Refers to i^{th} segment of trunk

$(\vec{})$ - Vector

$()_i$ - Refers to initial or equilibrium value

$()_i$ - Refers to value of variable when trunk is not in ground contact

$()_r$ - Refers to change in value of variable caused by trunk-ground contact

$\frac{d}{dt}$ - Differentiation with respect to time

THE STATIC MODEL

The Trunk Model

To facilitate the analysis, the trunk is divided into eight sections as shown in Figure 51. Each section is divided into segments: M segments per straight section and N segments per curved section. Thus the total number of trunk segments is $4(M+N)$. The location of each trunk segment (i.e., right or left, front or rear) can thus be identified by the section number I_s . The type of each segment (i.e., straight or curved) is denoted by the binary variable I_t . A value of $I_t = 0$ represents a curved segment, while $I_t = 1$ represents a straight segment. Numbering each segment clockwise starting from the center of the rear end trunk gives the following values of I_s and I_t .

Segment No. (i)	Section No. (I_s)	Type (I_t)
$0 < i \leq N$	1	1
$N < i \leq N + M$	2	0
$N + M < i \leq N + 2M$	3	0
$N + 2M < i \leq 2N + 2M$	4	1
$2N + 2M < i \leq 3N + 2M$	5	1
$3N + 2M < i \leq 3N + 3M$	6	0
$3N + 3M < i \leq 3N + 4M$	7	0
$3N + 4M < i \leq 4N + 4M$	8	1

The above grouping is subsequently used to keep track of the location and type of the segments when determining the moments generated by the cushion.

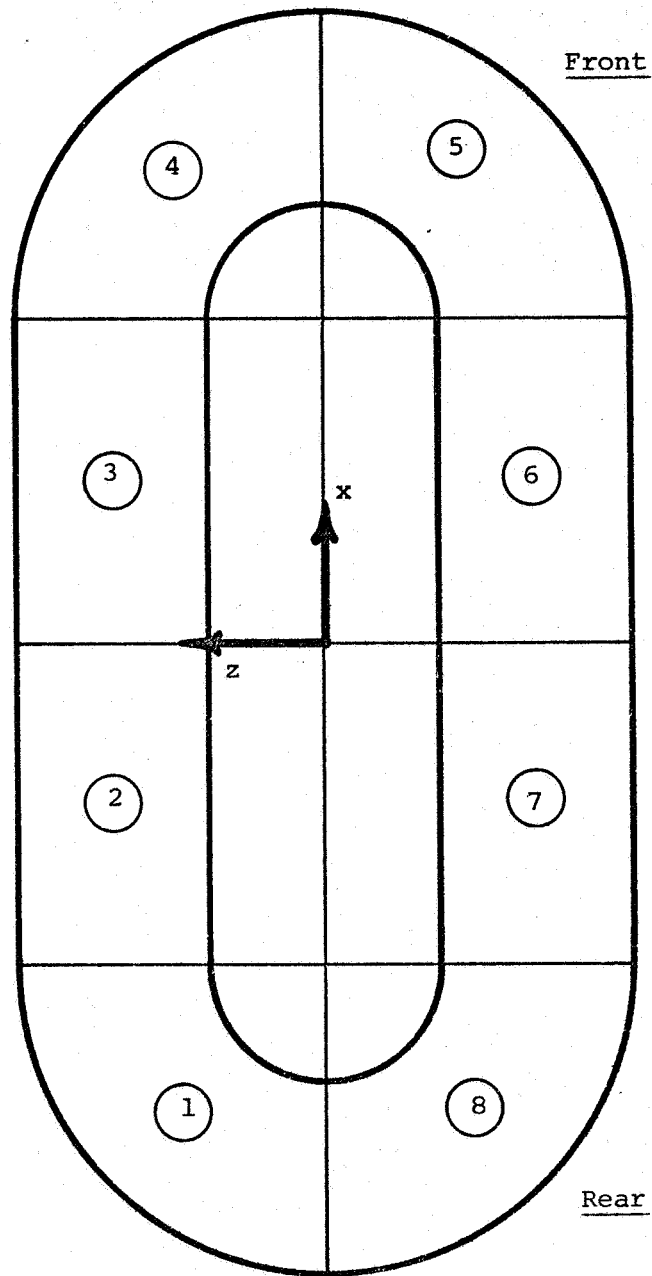


Figure 51. Trunk Sections (Bottom View)

Crosssectional Shape

Without Ground Contact - (a) The Side Trunk - The shape of the side trunk, made up of two circular arcs (Figure 52a), is defined by the four independent parameters a , b , ℓ , and H_y . The first three parameters are constants for any given design, while the fourth is found the pressure ratio through a membrane analysis (ref. 11) of the side trunk. The trunk height H_y can be expressed as

$$H_y/H_{yi} = f(P_c/P_t) \quad (A-1)$$

where

$$H_y = \text{trunk height}$$

$$H_{yi} = \text{trunk height at } P_c = 0, \text{ and}$$

$$P_c/P_t = \text{cushion-to-trunk pressure ratio}$$

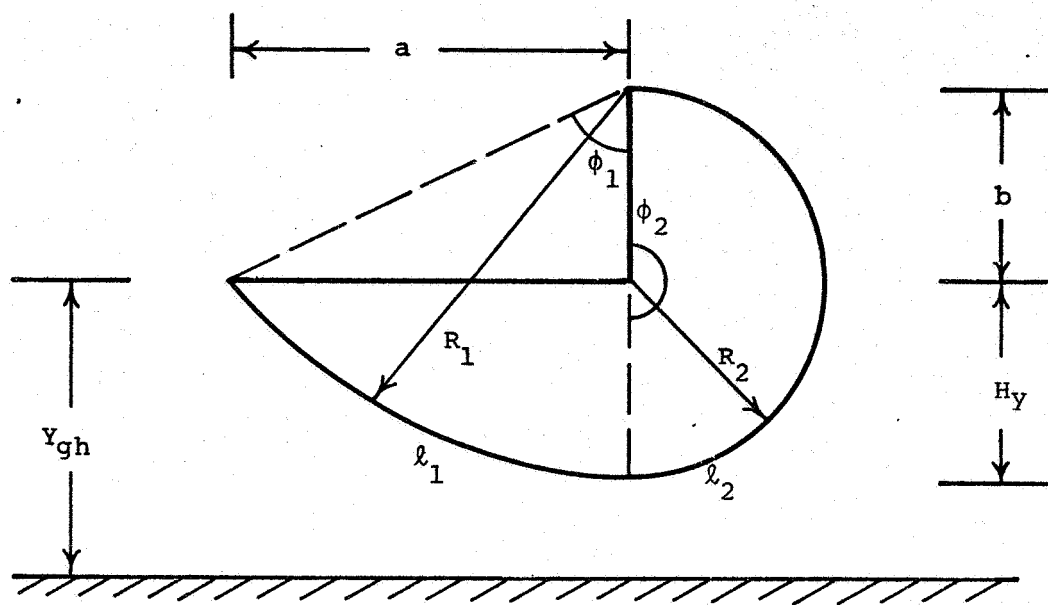
The above functional relationship is found by simultaneous solution of the following ten equations; the first nine for geometric compatibility and the tenth for force equilibrium.

$$R_1 \phi_1 = \ell_1 \quad (A-2)$$

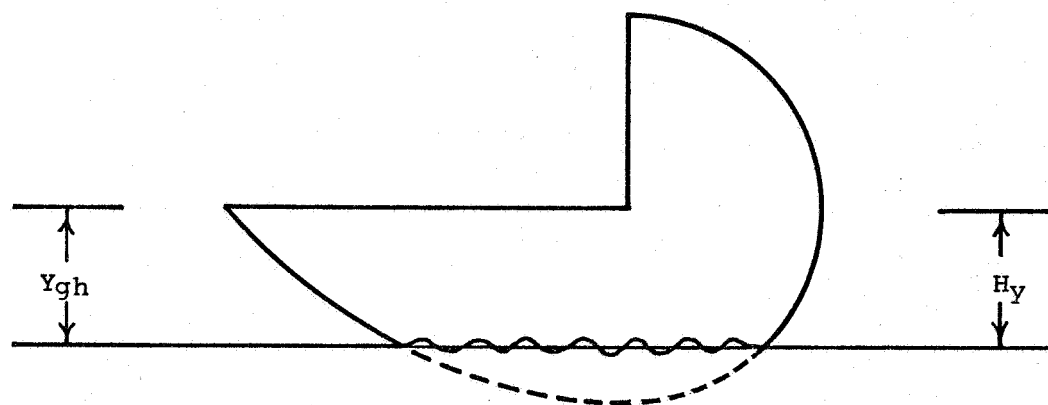
$$R_2 \phi_2 = \ell_2 \quad (A-3)$$

$$\ell_1 + \ell_2 = \ell \quad (A-4)$$

$$\cos \phi_2 = (R_2 - H_y)/R_2 \quad (A-5)$$



(a) No Ground Contact



(b) With Ground Contact

Figure 52. Trunk Shape

$$R_1 \cos(\phi_1 - \pi/2) + R_2 \sin \phi_2 = a \quad (\text{A-6})$$

$$R_1 \sin(\phi_1 - \pi/2) - (H_y - R_1) = b \quad (\text{A-7})$$

$$H_{yi} = R + \left(\sqrt{R^2 - \left(\frac{a^2 + b^2}{4} \right)} - \frac{b}{a} \sqrt{\frac{a^2 + b^2}{2}} \right) \cos(\tan^{-1} b/a) \quad (\text{A-8})$$

$$\ell = \left[2\pi - 2\sin^{-1} \left(\frac{\sqrt{a^2 + b^2}}{2R} \right) \right] R \quad (\text{A-9})$$

$$R_1/R_2 = 1 - (P_c/P_t) \quad (\text{A-10})$$

(b) The End Trunk - The shape of the end trunk is also made up of two circular arcs and defined by the four independent parameters a , b , ℓ , and H_y . However, because the end trunk shape is independent of the pressure ratio (frozen), the trunk height H_y is constant.

$$H_y = K \quad (\text{A-11})$$

where K is the design value of the end trunk height. For the simulations described in this report, H_y is taken to be equal to H_{yi} .

With Ground Contact - When the value of H_y , as calculated from Equation (A-1) or (A-11), exceeds the available ground clearance, the trunk shape changes due to ground contact. In keeping with the assumption of the hybrid trunk model, ground contact only affects the shape in the contact zone, and causes the trunk to conform with the ground contour as shown in Figure 52b. In this situation,

$$H_y = Y_{gh}(i) \quad (A-12)$$

Segment Center Distance

The segment center distance $X_{cx}(i)$ and $Z_{cx}(i)$ (Figure 4) are found as follows.

Section 1 ($I_s = 1$)

$$X_{cx}(i) = -L_s/2 - (d/2 + R_2 \sin \phi_2) \cos \delta(i) \quad (A-13)$$

$$Z_{cx}(i) = (d/2 + R_2 \sin \phi_2) \sin \delta(i) \quad (A-14)$$

where

$$\delta(i) = (i-0.5)\beta, \text{ and}$$

$$\beta = \pi/2N$$

Section 2 ($I_s = 2$)

$$X_{cx}(i) = -L_s/2 + (i-0.5-N) dx \quad (A-15)$$

$$Z_{cx}(i) = R_2 \sin \phi_2 + d/2 \quad (A-16)$$

where

$$dx = L_S/2M$$

Section 3 ($I_S = 3$)

$$X_{cx}(i) = (i-N-M-0.5) dx \quad (A-17)$$

$$Z_{cx}(i) = R_2 \sin\phi_2 + D/2 \quad (A-18)$$

Section 4 ($I_S = 4$)

$$X_{cx}(i) = L_S/2 + (d/2 + R_2 \sin\phi_2) \sin\delta(i) \quad (A-19)$$

$$Z_{cx}(i) = (d/2 + R_2 \sin\phi_2) \cos\delta(i) \quad (A-20)$$

where

$$\delta(i) = (i-N-2M-0.5)\beta$$

Section 5 ($I_S = 5$)

$$X_{cx}(i) = L_S/2 + (d/2 + R_2 \sin\phi_2) \cos\delta(i) \quad (A-21)$$

$$Z_{cx}(i) = (d/2 + R_2 \sin\phi_2) \sin\delta(i) \quad (A-22)$$

where

$$\delta(i) = (i-2N-2M-0.5)\beta$$

Section 6 ($I_s = 6$)

$$X_{cx}(i) = L_s/2 - (i-3N-2M-0.5) dx \quad (A-23)$$

$$Z_{cx}(i) = -(R_2 \sin \phi_2 + d/2) \quad (A-24)$$

Section 7 ($I_s = 7$)

$$X_{cx}(i) = -(i-3N-3M-0.5) dx \quad (A-25)$$

$$Z_{cx}(i) = -(R_2 \sin \phi_2 + d/2) \quad (A-26)$$

Section 8 ($I_s = 8$)

$$X_{cx}(i) = -L_s/2 - (d/2 + R_2 \sin \phi_2) \sin \delta(i) \quad (A-27)$$

$$Z_{cx}(i) = -(d/2 + R_2 \sin \phi_2) \cos \delta(i) \quad (A-28)$$

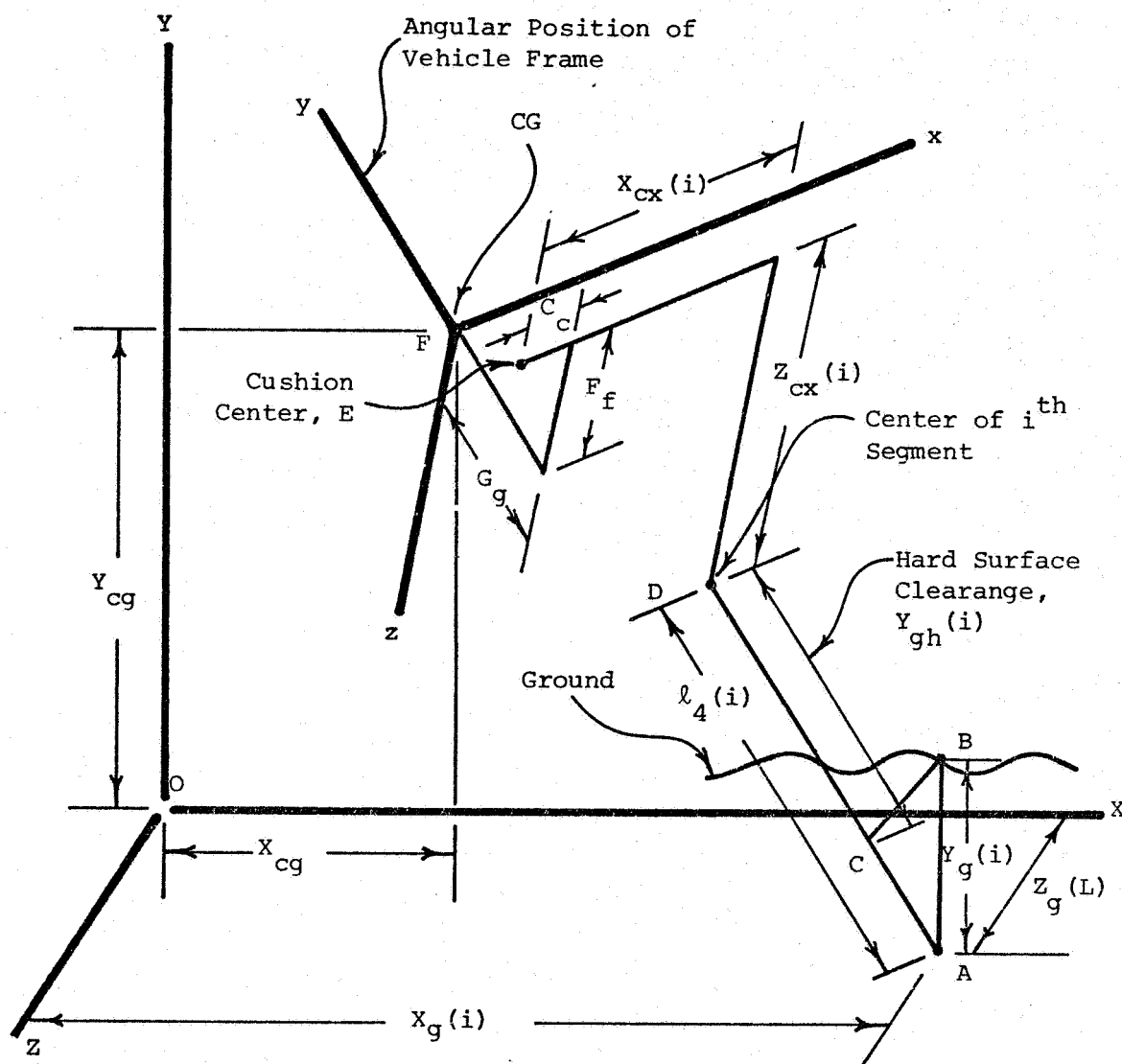
where

$$\delta(i) = (i-3N-4M-0.5)\beta$$

Hard Surface Clearance

The hard surface clearance for each segment, $Y_{gh}(i)$, is found from the position of the ACLS (X_{cg} , Y_{cg} , θ_e , ϕ_e) and from the ground profile (Figure 53). This is carried out in three steps.

- (a) The parameters $X_g(i)$, $Z_g(i)$, $\ell_4(i)$ and the orientation of vector \vec{DA} for each segment are calculated



- (b) The ground profile coordinates and DA are used to calculate the length CA
- (c) The hard surface clearance for each segment is then given by $\ell_4(i) - CA$

The results of the analysis give

$$\begin{aligned} x_g(i) = & x_{cg} + [x_{cx}(i) - c_c] b_{11} \\ & - [\ell_4(i) + G_g] b_{21} + [z_{cx}(i) - F_f] b_{31} \quad (A-29) \end{aligned}$$

$$\begin{aligned} z_g(i) = & [x_{cx}(i) - c_c] b_{13} \\ & - [\ell_4(i) + G_g] b_{23} + [z_{cx}(i) - F_f] b_{33} \quad (A-30) \end{aligned}$$

$$\begin{aligned} \ell_4(i) = & y_{cg}/b_{22} + [x_{cx}(i) - c_c] b_{12}/b_{22} \\ & + [z_{cx}(i) - F_f] b_{32}/b_{22} - G_g \quad (A-31) \end{aligned}$$

where $b_{m,n}$, the transformation factors that convert from the vehicle frame to the inertial (Euler Angle) frame are given by

$$b_{11} = \cos\psi_e \cos\phi_e + \sin\theta_e \sin\phi_e \sin\psi_e$$

$$b_{12} = \sin\phi_e \cos\theta_e$$

$$b_{13} = -\sin\psi_e \cos\phi_e + \sin\theta_e \sin\phi_e \cos\psi_e$$

$$b_{21} = \sin\psi_e \cos\phi_e \sin\theta_e - \sin\phi_e \cos\psi_e$$

$$b_{22} = \cos\phi_e \cos\theta_e$$

$$b_{23} = \sin\phi_e \sin\psi_e + \cos\psi_e \cos\phi_e \sin\theta_e$$

The length CA is given by

$$CA = Y_g(i) \cos\phi_e \cos\theta_e \quad (A-32)$$

where the ground coordinate $Y_g(i)$ is found from the profile relationship

$$Y_g(i) = f[X_g(i), Z_g(i)] \quad (A-33)$$

The hard surface clearance is then given by

$$Y_{gh}(i) = l_4(i) - CA \quad (A-34)$$

Areas and Volumes

The orifice areas and cushion and trunk volumes, for a particular trunk orientation, are calculated independently for each segment and then combined to give the total system value. For convenience, some of the areas and volumes are divided into two components - the i component and the r component (denoted by the subscripts i and r). The i values are calculated assuming that the trunk segment under consideration is out of ground contact. The r values represent the changes in the segment areas and volumes due to trunk-ground contact. The actual segment areas and volumes are found by subtracting the respective r values from the i values. The total areas and volumes are determined by combining the areas and volumes for each segment. For example

$$V_t = \sum_{i=1}^{4(M+N)} (V_{ti}(i) - V_{tr}(i)) \quad (A-35)$$

where

V_t = total trunk volume

$V_{ti}(i)$ = i value of trunk volume for i^{th} segment

$V_{tr}(i)$ = r value of trunk volume for i^{th} segment

$(V_{tr}(i) = 0 \text{ if } i^{th} \text{ segment is not in ground contact.})$

Similar relations hold good for cushion area, A_c ; cushion volume, V_c ; and gap area, A_g . Other parameters, such as A_{tc} , A_{ta} , A_{tac} , A_{tcc} , and A_{cn} are calculated directly in a single step.

Without Ground Contact - From Figure 54, the trunk cross-sectional area $A_{ti}(i)$ is given by

$$A_{ti}(i) = A_1 - A_2 + A_3 - A_4 + A_5 \quad (A-36)$$

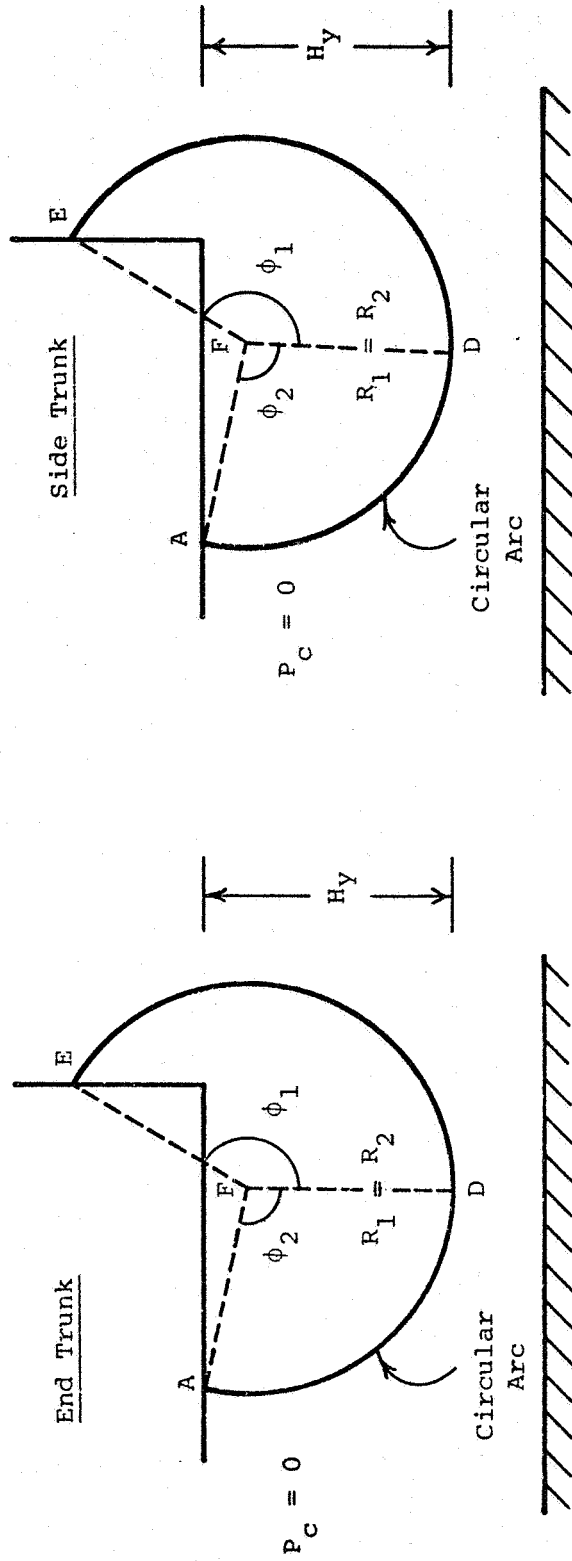
where

$$A_1 = \phi_2 R_2^2 / 2$$

$$A_2 = (R_2 - H_y) (R_2 \sin \phi_2) / 2$$

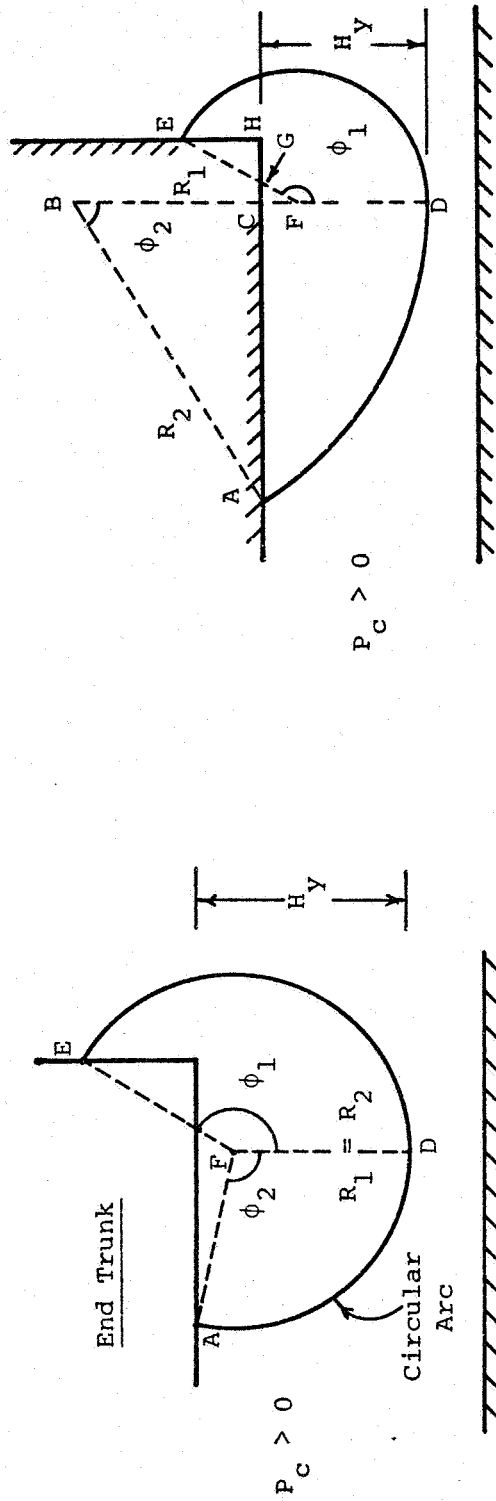
$$A_3 = \phi_1 R_1^2 / 2$$

$$A_4 = Xb / 2$$



(a) No Ground Contact; Zero Cushion Pressure

Figure 54. Trunk Shape Model



(b) No Ground Contact; Positive Cushion Pressure

Figure 54 (cont.). Trunk Shape Model

(c) With Ground Contact

Sector	Sector
1 = ABD	6 = BDJ
2 = ABC	7 = BJL
3 = EDF	8 = DFK
4 = ECH	9 = FLK
5 = GFG	

Figure 54 (concluded). Trunk Shape Model

$$A_5 = (a - R_2 \sin \phi_2 - X) (H_y - R_1)/2$$

and

$$X = \frac{b(a - R_2 \sin \phi_2)}{b + H_y - R_1}$$

The trunk volume for the i^{th} segment is given by

$$V_{ti}(i) = \begin{cases} dx A_{ti}(i) & ; I_t = 0 \\ (\frac{d}{2} + X_e) \beta A_{ti}(i) & ; I_t = 1 \end{cases} \quad (A-37)$$

where X_e is the horizontal distance of the centroid of the area A_{ti} from the inner trunk attachment point. X_e is calculated as follows

$$X_e = \frac{A_1 X_1 - A_2 X_2 + A_3 X_3 - A_4 X_4 + A_5 X_5}{A_{ti}(i)} \quad (A-38)$$

where X_1, X_2 , etc., are the X coordinates of the centroids of the areas A_1, A_2 , etc., respectively.

$$X_1 = R_2 \sin \phi_2 - 4 \sin^2 (\phi_2/2) R_2/3\phi_2$$

$$X_2 = 0.6667 R_2 \sin \phi_2$$

$$X_3 = R_2 \sin \phi_2 + 4 \sin^2 (\phi_1/2) R_1/3\phi_1$$

$$X_4 = a - 0.333X$$

$$X_5 = R_2 \sin \phi_2 + 0.333 (a - R_2 \sin \phi_2 - X)$$

The cushion area for the i^{th} segment is given by

$$A_{ci}(i) = \begin{cases} (d/2 + R_2 \sin \phi_2) dx & ; I_t = 0 \\ (d/2 + R_2 \sin \phi_2)^2 \beta/2 & ; I_t = 1 \end{cases} \quad (\text{A-39})$$

To calculate the trunk-to-cushion flow area it is necessary to start with the number of trunk holes communicating with the cushion. The number of rows of holes communicating with the cushion is given by the integer value of $(\ell_2 - \ell_p / S_h) + 1$. The number of communicating holes is $\left[(\ell_2 - \ell_p / S_h) + 1 \right] N_h$. The trunk-to-cushion flow area for the i^{th} segment is thus given by

$$A_{tci}(i) = \text{integer} \left[\frac{\ell_2 - \ell_p}{S_h} + 1 \right] N_h A_h \cdot dx/S \quad (\text{A-40})$$

$$\text{for } I_t = 0$$

and

$$A_{tci}(i) = \text{integer} \left[\frac{\ell_2 - \ell_p}{S_h} + 1 \right] N_h A_h \cdot \beta (d/2 + R_2 \sin \phi_2)/S \quad (\text{A-40})$$

$$\text{for } I_t = 1$$

where S , the cushion periphery, is given by

$$S = 2L_s + 2\pi (d/2 + R_2 \sin \phi_2)$$

The trunk-to-atmosphere flow area for the i^{th} segment is given by

$$A_{tai}(i) = N_r A_h N_h \cdot dx/S - A_{tci}(i) \quad (\text{A-41})$$

$$\text{for } I_t = 0$$

and

$$A_{tai}(i) = N_r A_h N_h \cdot \frac{\beta(d/2 + R_2 \sin \phi_2)}{S} - A_{tci}(i) \quad (\text{A-41})$$

$$\text{for } I_t = 1$$

The cushion-to-atmosphere flow area (gap area) for the i^{th} segment is

$$A_{gi}(i) = \begin{cases} [Y_{gh}(i) - H_y] dx & ; I_t = 0 \\ [Y_{gh}(i) - H_y] (d/2 + R_2 \sin \phi_2) \beta; & I_t = 1 \end{cases} \quad (\text{A-42})$$

Finally, the cushion volume for the i^{th} segment is given by

$$V_{ci}(i) = Y_{gh}(i) (d/2 + R_2 \sin \phi_2 - A_1 + A_2) dx \quad (\text{A-43})$$

$$\text{for } I_t = 0$$

and

$$V_{ci}(i) = Y_{gh}(i) \frac{\beta}{2} (d/2 + R_2 \sin \phi_2)^2 - \beta(d/2 + X_{12})(A_1 - A_2) ; I_t = 1 \quad (\text{A-43})$$

where

$$X_{12} = \frac{X_1 A_1 - X_2 A_2}{A_1 - A_2}$$

With Ground Contact - Ground contact occurs when $Y_{gh}(i) < H_y$ for the trunk sides, or $Y_{gh}(i) < K$ for the trunk ends. With ground contact, the trunk cross-sectional area changes as follows:

$$A_{tr}(i) = \begin{cases} A_6 - A_7 + A_8 - A_9 & ; \phi_4 \leq \pi/2 \\ A_6 - A_7 + A_{10} - A_{11} & ; \phi_4 > \pi/2 \end{cases} \quad (A-46)$$

where A_6 , A_7 , etc., are the areas of the sectors shown in Figure 54.

$$A_6 = R_2^2 \phi_3 / 2$$

$$A_7 = \frac{(R_2 - H_y + Y_{gh}(i))}{2} R_2 \sin \phi_3$$

$$A_8 = R_1^2 \phi_4 / 2$$

$$A_9 = \frac{(R_1 - H_y + Y_{gh}(i))}{2} R_1 \sin \phi_4$$

$$A_{10} = [R_1 - H_y + Y_{gh}(i)] R_1$$

$$A_{11} = R_1^2 \pi / 4$$

and

$$\phi_3 = \cos^{-1} \left[\frac{R_2 - [H_y - Y_{gh}(i)]}{R_2} \right]$$

$$\phi_4 = \cos^{-1} \left[\frac{R_1 - [H_y - Y_{gh}(i)]}{R_1} \right]$$

The r value of the trunk volume $V_{tr}(i)$ is calculated as follows

$$V_{tr}(i) = \begin{cases} (A_6 - A_7 + A_8 - A_9) dx ; \\ \quad \phi_4 \leq \pi/2 \\ \quad I_t = 0 \\ \\ (A_6 - A_7 + 2A_8 - 2A_9 - A_{10} + A_{11}) dx ; \\ \quad \phi_4 > \pi/2 \\ \quad I_t = 0 \\ \\ (A_6 - A_7 + A_8 - A_9) \beta (X_{er} + d/2) ; & (A-47) \\ \quad \phi_4 \leq \pi/2 \\ \quad I_t = 1 \\ \\ (A_6 - A_7) \beta (2X_{er} X_{br} + d/2) \\ + \beta d/2 (2A_8 - 2A_9 - A_{10} + A_{11}) \\ + 2\beta X_{er} (A_8 - A_9) - \beta X_{br} (A_{10} - A_{11}) ; \\ \quad \phi_4 > \pi/2 \\ \quad I_t = 1 \end{cases}$$

where X_{er} and X_{br} are the X-coordinates of the centroids of area

$$X_{er} = \frac{A_6 X_6 - A_7 X_7 + A_8 X_8 - A_9 X_9}{A_6 - A_7 + A_8 - A_9} \quad (A-48)$$

$$X_{br} = \frac{A_6 X_6 - A_7 X_7 + A_{11} X_{11} - A_{10} X_{10}}{A_6 - A_7 + A_{11} - A_{10}} \quad (A-49)$$

and X_6, X_7 , etc., are X coordinates of the areas A_6, A_7 , etc., respectively.

$$X_6 = R_2 \sin \phi_2 - 4 \sin^2 (\phi_3/2) R_2/3\phi_3$$

$$X_7 = R_2 \sin \phi_2 - 0.333 R_2 \sin \phi_3$$

$$X_8 = R_2 \sin \phi_2 + 4 \sin^2 (\phi_4/2) R_1/3\phi_4$$

$$X_9 = R_2 \sin \phi_2 + 0.333 R_1 \sin \phi_4$$

$$X_{10} = R_2 \sin \phi_2 + R_1/2$$

$$X_{11} = R_2 \sin \phi_2 + 4 \sin^2 (\pi/4) R_1/1.5\pi$$

The r value of the cushion area $A_{cr}(i)$ is given by

$$A_{cr}(i) = \begin{cases} dx R_2 \sin \phi_3 & ; I_t = 0 \\ \frac{\beta}{2} \left[2 \left(\frac{d}{2} + R_2 \sin \phi_2 \right) R_2 \sin \phi_3 \right. \\ \left. - R_2^2 \sin^2 \phi_3 \right] & ; I_t = 1 \end{cases} \quad (A-50)$$

The number of trunk orifice rows communicating with the cushion N_1 , is given by

$$N_1 = \text{integer} \left[\frac{\ell_2 - \ell_p - \phi_3 R_2}{S_h} \right] + 1 \quad (\text{A-51})$$

The area of the trunk orifices communicating with the cushion (for the i^{th} segment) is given by

$$A_{tci}(i) = \begin{cases} N_1 N_h A_h dx/S & ; I_t = 0 \\ N_1 N_h A_h \beta (d/2 + R_2 \sin \phi_3)/S & ; I_t = 1 \end{cases} \quad (\text{A-52})$$

Similarly, the number of orifice rows communicating with the atmosphere N_2 is given by

$$N_2 = \left[\frac{\ell_1 - \ell + \ell_p + (N_r - 1) S_h - \phi_4 R_1}{S_h} \right] + 1 \quad (\text{A-53})$$

The value of the trunk-to-atmosphere area for the i^{th} segment is

$$A_{tai}(i) = \begin{cases} N_2 N_h A_h dx/S & ; I_t = 0 \\ N_2 N_h A_h \beta (d/2 + R_2 \sin \phi_2)/S & ; I_t = 1 \end{cases} \quad (\text{A-54})$$

The orifice area communicating with the cushion for the i^{th} segment is given by

$$A_{tcr}(i) = \text{integer} \left(\frac{\ell_2 - \ell_p}{S_h} + 1 \right) N_h A_h dx/S_i - A_{tci}(i) \quad \text{for } I_t = 0 \quad (\text{A-55})$$

$$\begin{aligned}
A_{tcr}(i) &= \text{integer} \left(\frac{l_2 - l_p}{S_h} + 1 \right) N_h A_h \\
&\quad \cdot \frac{\beta(d/2 + R_2 \sin \phi_2)}{S_i} \\
&\quad - A_{tci}(i) \quad \text{for } I_t = 1
\end{aligned} \tag{A-55}$$

Similarly the orifice area for the i^{th} segment communicating with the atmosphere is given by

$$\begin{aligned}
A_{tar}(i) &= N_r N_h A_h dx/S - A_{tc}(i) - A_{ta}(i) \\
&\quad - A_{tcr}(i) \quad \text{for } I_t = 0
\end{aligned} \tag{A-56}$$

$$\begin{aligned}
A_{tar}(i) &= N_r N_h A_h \beta(d/2 + R_2 \sin \phi_2)/S - A_{tc}(i) \\
&\quad - A_{ta}(i) - A_{tcr}(i) \quad \text{for } I_t = 1
\end{aligned} \tag{A-56}$$

The r value of the clearance gap area is given by

$$A_{gr}(i) = A_{gi}(i) \tag{A-57}$$

The above equation is easily derived when it is recognized that ground contact blocks off the gap area.

The r value of the cushion volume is given by

$$V_{cr}(i) = \begin{cases} - dx (A_6 - A_7) & ; I_t = 0 \\ - \beta(d/2 + x_{cr}) (A_6 - A_7) & ; I_t = 1 \end{cases} \tag{A-58}$$

where

$$x_{cr} = \frac{A_6 X_6 - A_7 X_7}{A_6 - A_7}$$

The trunk-ground contact area on the cushion side of the contact zone is given by

$$A_{cni} = R_2 \sin \phi_3 dx \quad \text{for } I_t = 0 \quad (A-59)$$

$$A_{cni} = \frac{\beta}{2} (d/2 + R_2 \sin \phi_2)^2 - (d/2 + R_2 \sin \phi_2 - R_2 \sin \phi_3)^2 \quad (A-59)$$

$$\text{for } I_t = 1$$

The trunk-ground contact area on the atmosphere side of the contact zone is

$$A_{cni}(i) = R_1 \sin \phi_4 dx \quad (A-60)$$

$$\text{for } I_t = 0, \phi_4 \leq \pi/2$$

$$A_{cni}(i) = \frac{\beta}{2} (d/2 + R_2 \sin \phi_2 + R_1 \sin \phi_4)^2 - (d/2 + R_2 \sin \phi_2)^2 \quad (A-60)$$

$$\text{for } I_t = 1, \phi_4 \leq \pi_2$$

$$A_{\text{cnr}}(i) = R_1 dx \quad (\text{A-60})$$

$$\text{for } I_t = 0, \phi_4 > \pi/2$$

$$A_{\text{cnr}}(i) = \frac{\beta}{2} \left[(d/2 + R_2 \sin \phi_2 + R_1)^2 - (d/2 + R_2 \sin \phi_2)^2 \right] \quad (\text{A-60})$$

$$\text{for } I_t = 1, \phi_4 > \pi/2$$

Finally, the perimeter of the contact zone for the i^{th} segment is given by

$$l_c(i) = 2 dx \quad \text{for } I_t = 0 \quad (\text{A-61})$$

and

$$l_c(i) = \beta \left[2(d/2 + R_2 \sin \phi_2) - R_2 \sin \phi_3 + R_1 \sin \phi_4 \right] \quad (\text{A-61})$$

The values of V_t , A_c , V_c and A_g for the full trunk and cushion are obtained by subtracting the r values from the i values for each segment and summing them over all the segments.

$$V_t = \sum_{i=1}^{4(N+M)} [V_{ti}(i) - V_{tr}(i)] \quad (\text{A-35})$$

$$A_c = \sum_{i=1}^{4(N+M)} [A_{ci}(i) - A_{cr}(i)] \quad (\text{A-62})$$

$$V_c = \sum_{i=1}^{4(N+M)} [V_{ci}(i) - V_{cr}(i)] + V_d \quad (A-63)$$

and

$$A_g = \sum_{i=1}^{4(N+M)} [A_{gi}(i) - A_{gr}(i)] \quad (A-64)$$

The values of A_{tc} , A_{ta} , A_{cn} , A_{tac} , and A_{tcc} are obtained by adding the values for each segment.

$$A_{tc} = \sum_{i=1}^{4(N+M)} A_{tci}(i) \quad (A-65)$$

$$A_{ta} = \sum_{i=1}^{4(N+M)} A_{tai}(i) \quad (A-66)$$

$$A_{cn} = \sum_{i=1}^{4(N+M)} A_{cni}(i) + A_{cnr}(i) \quad (A-67)$$

$$A_{tac} = \sum_{i=1}^{4(N+M)} A_{tar}(i) \quad (A-68)$$

$$A_{tcc} = \sum_{i=1}^{4(N+M)} A_{tcr}(i) \quad (A-69)$$

Center of Pressure

The distance of the centers of pressure of each segment from the center of the cushion are required in order to estimate the torques acting on the ACLS. The positions of the centers of pressure depend on whether or not the segment is in ground contact as illustrated in Figure 55.

Without Ground Contact - Since the pressures inside the trunk and the cushion are uniform, the pressure centers coincide with the respective centroids of the projected area. The center of pressure distances $X_{ch}(i)$ and $Z_{ch}(i)$ are:

$$\underline{I_s = 1}$$

$$X_{ch}(i) = -L_s/2 - (d/2 + R_2 \sin \phi_2) \beta_2 \cos \delta(i) \quad (A-70)$$

where

$$\beta_2 = \frac{1.333}{\beta} \sin(\beta/2)$$

$$Z_{ch}(i) = Z_{cx}(i) \beta_2 \quad (A-71)$$

where $Z_{cx}(i)$ is evaluated from Equation (A-14).

$$\underline{I_s = 2}$$

$$X_{ch}(i) = X_{cx}(i) \quad (A-72)$$

$$Z_{ch}(i) = Z_{cx}(i)/2 \quad (A-73)$$

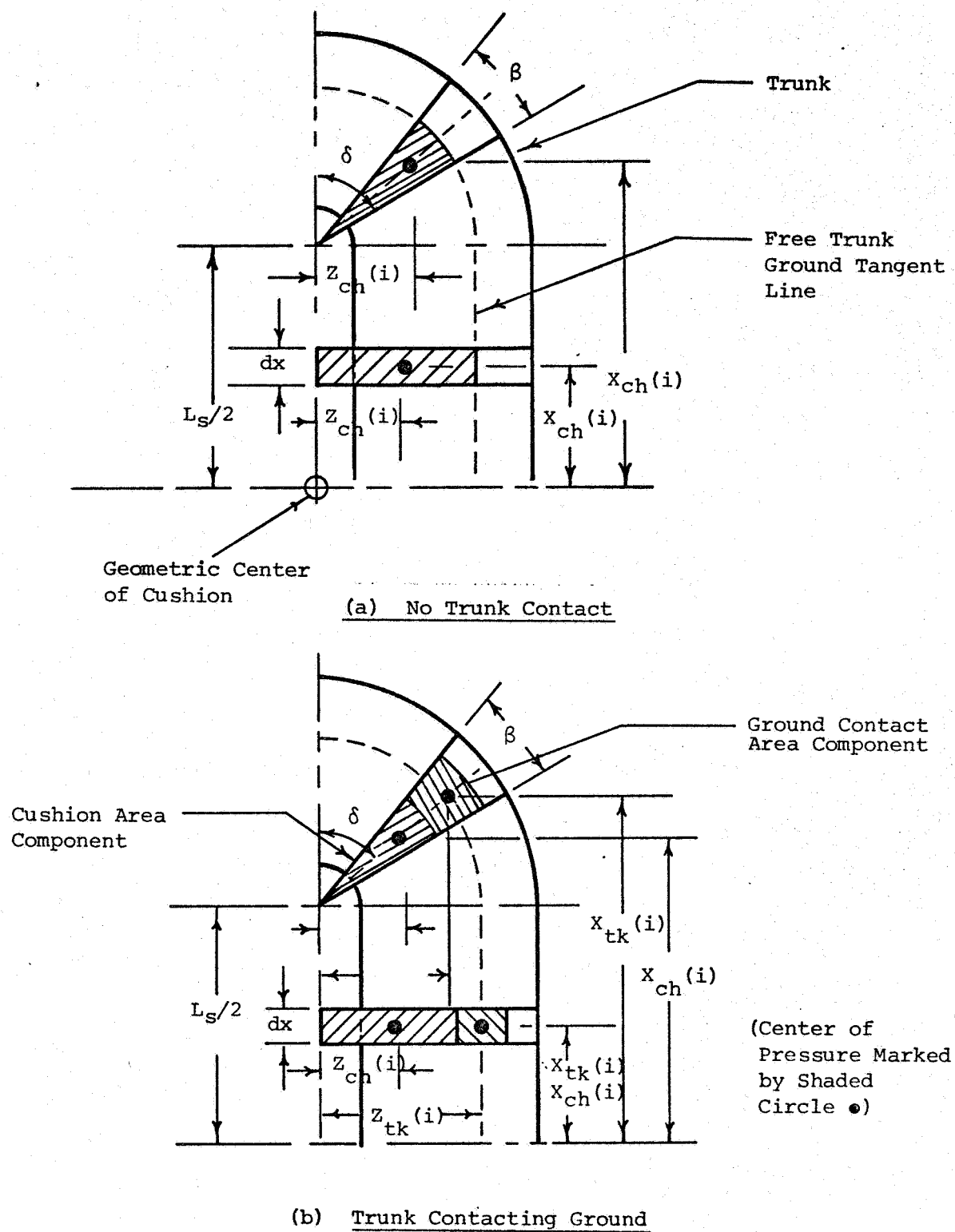


Figure 55. The Position of the Center of Pressure

where $X_{cx}(i)$ and $Z_{cx}(i)$ are obtained from Equations (A-15) and (A-16) respectively.

$$\underline{I_s = 3}$$

$$X_{ch}(i) = X_{cx}(i) \quad (A-74)$$

$$Z_{ch}(i) = Z_{cx}(i)/2 \quad (A-75)$$

where $X_{cx}(i)$ and $Z_{cx}(i)$ are obtained from Equations (A-17) and (A-18) respectively.

$$\underline{I_s = 4}$$

$$X_{ch}(i) = L_s/2 + (d/2 + R_2 \sin \phi_2) \sin \delta(i) \beta_2 \quad (A-76)$$

$$Z_{ch}(i) = Z_{cx}(i) \beta_2 \quad (A-77)$$

where $Z_{cx}(i)$ is obtained from Equation (A-20).

$$\underline{I_s = 5}$$

$$X_{ch}(i) = L_s/2 + (d/2 + R_2 \sin \phi_2) \cos \delta(i) \beta_2 \quad (A-78)$$

$$Z_{ch}(i) = Z_{cx}(i) \beta_2 \quad (A-79)$$

where $Z_{cx}(i)$ is evaluated from Equation (A-22).

$$\underline{I_s = 6}$$

$$X_{ch}(i) = X_{cx}(i) \quad (A-80)$$

$$Z_{ch}(i) = Z_{cx}(i)/2 \quad (A-81)$$

where $X_{cx}(i)$ and $Z_{cx}(i)$ are obtained from Equations (A-23) and (A-24) respectively.

$$\underline{I_s = 7}$$

$$X_{ch}(i) = X_{cx}(i) \quad (A-82)$$

$$Z_{ch}(i) = Z_{cx}(i)/2 \quad (A-83)$$

where $X_{cx}(i)$ and $Z_{cx}(i)$ are obtained from Equations (A-25) and (A-26) respectively.

$$\underline{I_s = 8}$$

$$X_{ch}(i) = - \left[L_s/2 + (d/2 + R_2 \sin \phi_2) \sin \delta(i) \beta_2 \right] \quad (A-84)$$

$$Z_{ch}(i) = Z_{cx}(i) \beta_2 \quad (A-85)$$

where $Z_{cx}(i)$ is obtained from Equation (A-28).

With Ground Contact - The center of cushion pressure distances $X_{ch}(i)$, $Z_{ch}(i)$ and the center of trunk pressure distances $X_{tk}(i)$, $Z_{tk}(i)$ for the i^{th} segment in ground contact are

$$\underline{I_s = 1}$$

$$\begin{aligned} X_{ch}(i) = & -L_s/2 - \beta_2 (d/2 + R_2 \sin \phi_2 \\ & - R_2 \sin \phi_3) \cos \delta(i) \end{aligned} \quad (A-86)$$

$$X_{tk}(i) = -L_s/2 - X_{xz} \cos \delta(i) \quad (A-87)$$

where

$$X_{x2} = \frac{4}{3} \frac{\sin(\beta/2)}{\beta} \left(\frac{R_r^3 - R_{r1}^3}{R_r^2 - R_{r1}^2} \right)$$

$$R_r = d/2 + R_2 \sin \phi_2 + R_1 \sin \phi_4 \quad (\phi_4 \leq \pi/2)$$

$$R_{r1} = d/2 + R_2 \sin \phi_2 - R_2 \sin \phi_3$$

$$Z_{ch}(i) = \beta_2 (d/2 + R_2 \sin \phi_2 - R_2 \sin \phi_3) \sin \delta(i) \quad (A-88)$$

$$Z_{tk}(i) = X_{x2} \sin \delta(i) \quad (A-89)$$

$$\underline{I_s = 2, 3}$$

$$X_{ch}(i) = X_{cx}(i) \quad (A-90)$$

$$X_{tk}(i) = X_{cx}(i) \quad (A-91)$$

where $X_{cx}(i)$ is obtained from Equation (A-15) for $I_s = 2$, and from Equation (A-17) for $I_s = 3$.

$$Z_{ch}(i) = (d/2 + R_2 \sin \phi_2 - R_2 \sin \phi_3)/2 \quad (A-92)$$

$$\begin{aligned}
Z_{tk}(i) &= d/2 + R_2 \sin \phi_2 \\
&\quad + (R_1 \sin \phi_4 - R_2 \sin \phi_3)/2
\end{aligned} \tag{A-93}$$

$$\underline{I_s = 4}$$

$$\begin{aligned}
X_{ch}(i) &= L_s/2 + \beta_2 (d/2 + R_2 \sin \phi_2 \\
&\quad - R_2 \sin \phi_3) \sin \delta(i)
\end{aligned} \tag{A-94}$$

$$X_{tk}(i) = L_s/2 + X_{x2} \sin \delta(i) \tag{A-95}$$

$$Z_{ch}(i) = \beta_2 (d/2 + R_2 \sin \phi_2 - R_2 \sin \phi_3) \cos \delta(i) \tag{A-96}$$

$$Z_{tk}(i) = X_{x2} \cos \delta(i) \tag{A-97}$$

$$\underline{I_s = 5}$$

$$\begin{aligned}
X_{ch}(i) &= L_s/2 + \beta_2 (d/2 + R_2 \sin \phi_2 \\
&\quad - R_2 \sin \phi_3) \cos \delta(i)
\end{aligned} \tag{A-98}$$

$$X_{tk}(i) = L_s/2 + X_{x2} \cos \delta(i) \tag{A-99}$$

$$Z_{ch}(i) = -\beta_2 (d/2 + R_2 \sin \phi_2 - R_2 \sin \phi_3) \sin \delta(i) \tag{A-100}$$

$$Z_{tk}(i) = -X_{x2} \sin \delta(i) \tag{A-101}$$

$$\underline{I_s = 6,7}$$

$$X_{ch}(i) = X_{cx}(i) \tag{A-102}$$

$$X_{tk}(i) = X_{cx}(i) \quad (A-103)$$

where $X_{cx}(i)$ is given by Equation (A-23) for $I_s = 6$, and by Equation (A-25) for $I_s = 7$.

$$Z_{ch}(i) = - (d/2 + R_2 \sin \phi_2 - R_2 \sin \phi_e) / 2 \quad (A-104)$$

$$Z_{tk}(i) = -d/2 - R_2 \sin \phi_2 - (R_1 \sin \phi_4 - R_2 \sin \phi_3) / 2 \quad (A-105)$$

$$\underline{I_s = 8}$$

$$X_{ch}(i) = -L_s/2 - \beta_2 (d/2 + R_2 \sin \phi_2 - R_2 \sin \phi_3) \sin \delta(i) \quad (A-106)$$

$$X_{tk}(i) = -L_s/2 - X_{x2} \sin \delta(i) \quad (A-107)$$

$$Z_{ch}(i) = -\beta_2 (d/2 + R_2 \sin \phi_2 - R_2 \sin \phi_3) \cos \delta(i) \quad (A-108)$$

$$Z_{tk}(i) = -X_{x2} \cos \delta(i) \quad (A-109)$$

It should be noted that the upper bound on ϕ_4 in Equation (A-93) and (A-105) is $\pi/2$

The Flow Model

The flow through system is shown in Figure 56. The flow through the upstream fan orifice is given by

$$Q_f = A_{af} C_{af} \sqrt{\frac{-2P_{af}}{\rho}} \quad (A-110)$$

where

Q_f = volume flow through the fan

A_{af} = orifice area, atmosphere to fan inlet

C_{af} = fan inlet orifice discharge coefficient

P_{af} = fan entrance pressure (negative, gage)

ρ = air density

The fan pressure rise, P_f , is given by

$$P_f = P_p - P_{af} \quad (A-111)$$

where

P_p = plenum pressure (gage)

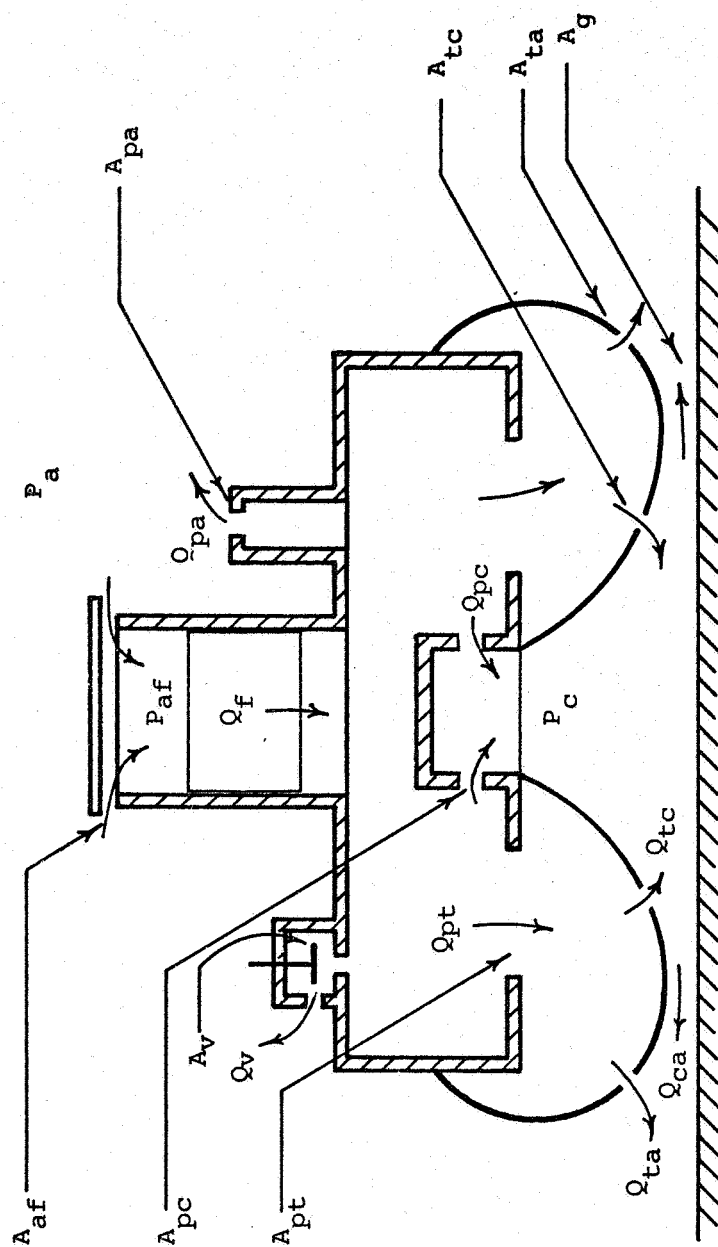


Figure 56. Flow Through the ACLS

The fan flow is obtained from the fan characteristic, and is a function of the fan pressure rise.

$$Q_f = f(P_f) \quad (A-112)$$

The remaining flows are found as follows.

$$Q_{pa} = A_{pa} C_{pa} \sqrt{\frac{2 P_p}{\rho}} \quad (A-113)$$

where

Q_{pa} = plenum-atmosphere flow rate (excluding relief valve flows)

A_{pa} = plenum to atmosphere orifice area

C_{pa} = discharge coefficient for A_{pa}

$$Q_{fp} = Q_f - Q_{pa} \quad (A-114)$$

where

Q_{fp} = fan-to-plenum flow rate

$$Q_{fp} = Q_{pc} + Q_{pt} \quad (A-115)$$

where

Q_{pc} = plenum-to-cushion flow rate

Q_{pt} = plenum-to-trunk flow rate

$$Q_{pc} = A_{pc} C_{pc} \sqrt{\frac{2(P_p - P_c)}{\rho}} \quad (A-116)$$

where

P_c = cushion pressure (gage)

A_{pc} = plenum-to-cushion orifice area

C_{pc} = discharge coefficient for A_{pc}

($Q_v = 0$, since in static operation, the pressure relief valve is closed)

$$Q_{pt} = A_{pt} C_{pt} \sqrt{\frac{2(P_p - P_t)}{\rho}} \quad (A-117)$$

where

P_t = trunk pressure (gage)

A_{pt} = plenum-to-trunk orifice area

C_{pt} = discharge coefficient for A_{pt}

$$Q_{pt} = Q_{tc} + Q_{ta} \quad (A-118)$$

where

Q_{tc} = trunk-to-cushion flow rate

Q_{ta} = trunk-to-atmosphere flow rate

$$Q_{tc} = C_{tc} \sqrt{\frac{2(P_t - P_c)}{\rho}} \left(A_{tc} + \frac{2}{3} A_{tcc} \right) \quad (A-119)$$

where

A_{tc} = trunk-to-cushion orifice area

A_{tcc} = orifice area on cushion side of the trunk-ground contact

C_{tc} = discharge coefficient of the trunk holes on the cushion side

The factor 2/3 comes in Equation (A-119) due to the triangular pressure profile assumed in the trunk-ground contact zone (see Figure 17). Since the pressure on the cushion side of the contact zone is linearly increasing from P_c to P_t , the flow is 2/3 of what it would be if the pressure was uniform and equal to P_c .

A_{tcc} is zero if there is no trunk-ground contact.

$$Q_{ta} = C_{ta} \sqrt{\frac{2P_t}{\rho}} \left(A_{ta} + \frac{2}{3} A_{tac} \right) \quad (A-120)$$

where

A_{ta} = trunk-atmosphere orifice area

A_{tac} = orifice area on atmosphere side of trunk contact

C_{ta} = discharge coefficient of the trunk holes on the atmosphere side

Just as in Equation (A-119), the factor $2/3$ comes in Equation (A-120) due to the pressure profile assumed in the trunk-ground contact area. Since the pressure on the atmosphere side of the trunk contact zone is linearly reducing from P_t to 0 (gage), the flow is two-thirds of what it would be if the pressure was uniform and equal to zero.

A_{tac} is zero if there is no trunk contact with the ground.

$$Q_{ca} = Q_{pc} + Q_{tc} \quad (A-121)$$

where

Q_{ca} = cushion-to-atmosphere flow rate

$$Q_{ca} = A_g C_g \sqrt{\frac{2P_c}{\rho}} \quad (A-122)$$

where

A_g = cushion gap area

C_g = coefficient discharge for A_g

The Force Model

The vertical force developed by the cushion is given by

$$F_{cn} = (P_c A_c + P_t A_{cn}) \cos \theta_e \cos \phi_e \quad (A-123)$$

where

P_c = cushion pressure, gage

A_c = cushion area

P_t = trunk pressure, gage

A_{cn} = trunk-ground contact area

θ_e = Eulerian roll angle

ϕ_e = Eulerian pitch angle

The torque developed about the cushion center by the cushion pressure force and trunk contact force about the vehicle x axis, T_{nx} , and vehicle z axis, T_{nz} , are:

$$T_{nx} = - \sum_{i=1}^{4(M+N)} \left\{ P_c [A_{ci}(i) - A_{cr}(i)] [Z_{ch}(i)] \right. \\ \left. + P_t [A_{cni}(i) + A_{cnr}(i)] [Z_{tk}(i)] \right\} \quad (A-124)$$

$$T_{nz} = \sum_{i=1}^{4(M+N)} \left\{ P_c [A_{ci}(i) - A_{cr}(i)] [X_{ch}(i)] \right. \\ \left. + P_t [A_{cni}(i) + A_{cnr}(i)] [X_{tk}(i)] \right\} \quad (A-125)$$

Under equilibrium conditions

$$F_{cn} = M_a g \quad (A-126)$$

$$T_{nx} = -F_f M_a g / (\cos \phi_e \cos \theta_e) \quad (A-127)$$

$$T_{nz} = C_c M_a g / (\cos \phi_e \cos \theta_e) \quad (A-128)$$

Under the equilibrium loading, the aircraft orients itself at a particular Y_{cg} , ϕ_e and θ_e . For a given value of X_{cg} , the variables Y_{cg} , ϕ_e and θ_e uniquely define the aircraft and ACLS position (Z_{cg} and ψ_e are zero). The area and distance variables needed to evaluate Equations (A-123), (A-124) and (A-125) are found from the relationships derived in the previous sections, and can be expressed as

$$A_{ci}(i) = F_1 (Y_{cg}, \theta_e, \phi_e) \quad (A-129)$$

$$A_{cr}(i) = F_2 (Y_{cg}, \theta_e, \phi_e) \quad (A-130)$$

$$A_{cn}(i) = F_3 (Y_{cg}, \theta_e, \phi_e) \quad (A-131)$$

$$X_{ch}(i) = F_4 (Y_{cg}, \theta_e, \phi_e) \quad (A-132)$$

$$X_{tk}(i) = F_5 (Y_{cg}, \theta_e, \phi_e) \quad (A-133)$$

$$Z_{ch}(i) = F_6 (Y_{cg}, \theta_e, \phi_e) \quad (A-134)$$

and $Z_{tk}(i) = F_7 (Y_{cg}, \theta_e, \phi_e) \quad (A-135)$

Also the orifice areas required by Equations (A-119), (A-120) and (A-122) depend on Y_{cg}, θ_e, ϕ_e and can be expressed as

$$A_{tc} = F_8 (Y_{cg}, \theta_e, \phi_e) \quad (A-136)$$

$$A_{ta} = F_9 (Y_{cg}, \theta_e, \phi_e) \quad (A-137)$$

and $A_g = F_{10} (Y_{cg}, \theta_e, \phi_e) \quad (A-138)$

For the static solution, it is necessary to solve Equations (A-110) to (A-138) simultaneously to determine the equilibrium aircraft position and ACLS pressures and flows.

THE DYNAMIC MODEL

The dynamic behavior of the ACLS is determined from the simultaneous solution of the state equations describing the body dynamics and fluid mechanics of the system.

The Force Model

The following assumptions are made in deriving the equations of motion.

- a) The aircraft does not experience any rotational motion about the vehicle y axis, i.e., there is no yaw motion in the vehicle coordinate frame ($\psi = \dot{\psi} = \ddot{\psi} = 0$).
- b) Forces acting along the vehicle z axis are zero ($F_z = 0$).
- c) The aircraft CG stays in the inertial xy plane, i.e., $F_{ze} = 0$ and $z_{cg} = \dot{z}_{cg} = \ddot{z}_{cg} = 0$.
- d) The component of the vehicle x axis force along the inertial vertical axis is negligible compared to the corresponding component of the vehicle y axis force, i.e., $F_x \sin \phi_e \cos \theta_e \ll F_y \cos \phi_e \cos \theta_e$.
- e) The forward motion of the aircraft CG (i.e., the motion along the inertial X axis) occurs at a constant deceleration which is determined from the braking coefficient of the ACLS.
- f) All forces act along the appropriate vehicle axes and not along the inertial axes. This comes about because

the ACLS model has been set up such that the ground underneath any particular trunk segment is considered parallel to the hard surface.

Forces and Torques

Vehicle y-axis Forces - The dynamic forces along the vehicle y axis consist of

- a) The cushion pressure force, F_{cp} .

$$F_{cp} = P_c A_c \quad (A-139)$$

- b) The trunk pressure force during trunk-ground contact F_{tp} .

$$F_{tp} = P_t A_{cn} \quad (A-140)$$

- c) The aerodynamic drag force, F_{df} .

$$F_{df} = - 1/2 C_d A_{ph} \rho V^3 / |V| \quad (A-141)$$

where V , the velocity component along the vehicle y axis is

$$V = \dot{X}_{cg} (\cos\phi_e \sin\theta_e \sin\psi_e - \cos\psi_e \sin\phi_e) \\ + \dot{Y}_{cg} (\cos\phi_e \cos\theta_e)$$

- d) The trunk damping force during trunk-ground contact, F_{ct}

$$F_{ct} = \begin{cases} \sum_{i=1}^{4(M+N)} - D_c l_c(i) V_t(i) & \text{if the segment is in} \\ & \text{ground contact} \\ 0 & \text{if the segment is not in ground contact.} \end{cases} \quad (A-142)$$

where the velocity of the trunk segment with respect to ground, $V_t(i)$ is given by the addition of the component of \dot{Y}_{cg} along the vehicle y axis and the component along the vehicle y axis of the relative velocity of the trunk segment center with respect to the CG, $V_r(i)$. The first component is $\dot{Y}_{cg} \cos \phi_e \cos \theta_e$. The second component is

$$V_r(i) = \vec{\omega} \times \vec{r}(i) \big|_{y \text{ axis}}$$

where

$$\vec{\omega} = \dot{\phi} \vec{u}_z + \dot{\theta} \vec{u}_x$$

$$\begin{aligned} \vec{r}(i) = & [x_{tk}(i) - c_c] \vec{u}_x + [-G_g - y_{gh}(i)] \vec{u}_y \\ & + (z_{tk} - F_f) \vec{u}_z \end{aligned}$$

and \vec{u}_x , \vec{u}_y and \vec{u}_z are unit vectors along the vehicle x, y and z axes. After substitution

$$\begin{aligned} V_t(i) = & [\dot{Y}_{cg} \cos \phi_e \cos \theta_e] + \dot{\phi} [x_{tk}(i) - c_c] \\ & - \dot{\theta} [z_{tk}(i) - F_f] \end{aligned} \quad (A-143)$$

The total force along the vehicle y axis is

$$F_{cy} = F_{cp} + F_{tp} + F_{df} + F_{ct} \quad (A-144)$$

and total force along the inertial Y axis is

$$F_{ey} = F_{cy} \cos \phi_e \cos \theta_e \quad (A-145)$$

Vehicle x-axis Torques - The torques acting about the aircraft CG on the vehicle x axis consist of:

- a) The cushion pressure torque, T_{cpx} .

$$T_{cpx} = -P_c [Z_{ch}(i) - F_f] [A_{ci}(i) - A_{cr}(i)] \quad (A-146)$$

- b) The torque due to trunk contact, T_{tpx} .

$$T_{tpx} = -P_t [Z_{tk}(i) - F_f] [A_{cni}(i) + A_{cnr}(i)] \quad (A-147)$$

- c) The torque due to aerodynamic drag, T_{dfx} .

$$T_{dfx} = -F_{df} C_{fz} \quad (A-148)$$

where C_{fz} is the distance along the vehicle z axis of the center of aerodynamic drag from the CG. C_{fz} is positive if the CG is left of the drag center.

- d) The torque due to trunk damping, T_{tx}

$$T_{tx} = - \sum_{i=1}^{4(M+N)} [Z_{tk}(i) - F_f] F_{ct}(i) \quad (A-149)$$

The total torque along the vehicle x axis, T_x , is then given by

$$T_x = T_{cpx} + T_{tpx} + T_{dfx} + T_{tx} \quad (A-150)$$

Vehicle z-axis Torques - The torques acting about the aircraft CG about the vehicle z axis consist of:

- a) The cushion pressure torque, T_{cpz}

$$T_{cpz} = P_c [X_{ch}(i) - C_c] [A_{ci}(i) - A_{cr}(i)] \quad (A-151)$$

- b) The torque due to trunk contact, T_{tpz}

$$T_{tpz} = P_t [X_{tk}(i) - C_c] [A_{cni}(i) + A_{cnr}(i)] \quad (A-152)$$

- c) The torque due to aerodynamic drag, T_{dfz}

$$T_{dfz} = F_{df} C_{fx} \quad (A-153)$$

where C_{fx} is the distance along the vehicle x axis of the center of drag from CG. C_{fx} is positive if the CG is behind the drag center.

- d) The torque due to trunk damping, T_{tz}

$$T_{tz} = \sum_{i=1}^{4(M+N)} [X_{tk}(i) - C_c] F_{ct}(i) \quad (A-154)$$

e) The torque due to ground friction, T_{fz}

$$T_{fz} = \begin{cases} - \sum_{i=1}^{4(M+N)} P_t [A_{cni}(i) + A_{cnr}(i)] \mu \\ \quad [Y_{gh}(i) + G_g] ; \dot{X}_{cg} \neq 0 \\ 0 ; \dot{X}_{cg} = 0 \end{cases} \quad (A-155)$$

The total torque along the vehicle z axis, T_z , is then given by

$$T_z = T_{cpz} + T_{tpz} + T_{dfz} + T_{tz} + T_{fz} \quad (A-156)$$

The Equations of Motion

The equations of motion give the relation between the forces and torques acting on the aircraft and its linear and rotational motion.

Linear Motion - The equations of linear motion are derived by applying Newton's second law in the inertial coordinate frame. The vertical motion of the aircraft CG is given by:

$$M_a \ddot{Y}_{cg} = F_y - M_a g \quad (A-157)$$

where F_y is the inertial vertical component of the vehicle y axis force. The equation of motion along the inertial x axis (forward motion) is simply

$$\ddot{x}_{cg} = -\mu \quad (A-158)$$

where μ is the specified deceleration rate.

Rotational Motion - If the total torque acting about CG of the aircraft is denoted by the vector \vec{T} , then

$$\vec{T} = d\vec{H}/dt \quad (A-159)$$

where \vec{H} is the angular momentum vector about the CG in the inertial frame.

The rate of change of momentum, $d\vec{H}/dt$, can be expressed as the sum of two components; one describing its rate of change relative to the vehicle frame and the other accounting for the rotation of the vehicle frame relative to the inertial frame. Thus

$$\frac{d\vec{H}}{dt} = \left(\frac{\partial \vec{H}}{\partial t} \right)_{v.f.} + \vec{\omega} \times (\vec{H})_{v.f.} \quad (A-160)$$

where $\vec{\omega}$ is the angular velocity vector of the vehicle frame (relative to the inertial frame) and is given by

$$\vec{\omega} = \dot{\theta} \vec{u}_x + \dot{\psi} \vec{u}_y + \dot{\phi} \vec{u}_z \quad (A-161)$$

where \vec{u}_x , \vec{u}_y and \vec{u}_z are unit vectors along the x, y and z axes of the vehicle frame.

The angular momentum vector \vec{H} and torque vector \vec{T} can also be divided into instantaneous components along the vehicle axes as follows

$$\vec{H} = H_x \vec{u}_x + H_y \vec{u}_y + H_z \vec{u}_z \quad (\text{A-162})$$

$$\vec{T} = T_x \vec{u}_x + T_y \vec{u}_y + T_z \vec{u}_z \quad (\text{A-163})$$

since \vec{H} is taken about the CG,

$$[H] = [I] \cdot [\omega] \quad (\text{A-164})$$

where $[H]$ is the angular momentum matrix

$$H = \begin{bmatrix} H_x \\ H_y \\ H_z \end{bmatrix}$$

$[I]$ is the inertia matrix

$$[I] = \begin{bmatrix} I_x & I_{xy} & I_{xz} \\ I_{xy} & I_y & I_{yz} \\ I_{xz} & I_{yz} & I_z \end{bmatrix}$$

and $[\omega]$ is the angular velocity matrix

$$[\omega] = \begin{bmatrix} \dot{\theta} \\ \dot{\psi} \\ \dot{\phi} \end{bmatrix}$$

Expressing Equations (A-159) and (A-160) in matrix form,

$$\begin{bmatrix} T_x \\ T_y \\ T_z \end{bmatrix} = \begin{bmatrix} I_x & I_{xy} & I_{xz} \\ I_{xy} & I_y & I_{yz} \\ I_{zx} & I_{yz} & I_z \end{bmatrix} \cdot \begin{bmatrix} \ddot{\theta} \\ \ddot{\psi} \\ \ddot{\phi} \end{bmatrix} + \begin{bmatrix} \dot{\theta} \\ \dot{\psi} \\ \dot{\phi} \end{bmatrix} \times \begin{bmatrix} I_x & I_{xy} & I_{xz} \\ I_{xy} & I_y & I_{yz} \\ I_{zx} & I_{yz} & I_z \end{bmatrix} \cdot \begin{bmatrix} \dot{\theta} \\ \dot{\psi} \\ \dot{\phi} \end{bmatrix} \quad (\text{A-165})$$

Equation (A-165) gives three simultaneous equations which can be solved to obtain the rotational accelerations $\ddot{\theta}$, $\ddot{\psi}$ and $\ddot{\phi}$ in terms of the angular velocities and torques. Substituting $\dot{\psi} = \ddot{\psi} = \ddot{\phi} = 0$ (no yaw motion) and solving for $\ddot{\theta}$ and $\ddot{\phi}$ gives

$$\ddot{\theta} = \frac{I_z [T_x + \dot{\phi} (I_{xy} \dot{\theta} + I_{yz} \dot{\phi})] - I_{zx} [T_z - \dot{\theta} (I_{xy} \dot{\theta} + I_{yz} \dot{\phi})]}{I_z I_x - I_{zx}^2} \quad (\text{A-166})$$

$$\ddot{\phi} = \frac{I_x [T_z - \dot{\theta} (I_{xy} \dot{\theta} + I_{yz} \dot{\phi})] - I_{zy} [T_x + \dot{\phi} (I_{xy} \dot{\theta} + I_{yz} \dot{\phi})]}{I_z I_x - I_{zx}^2} \quad (\text{A-167})$$

Angular Coordinate Transformation

The angular position of the aircraft in the inertial frame is defined by the Eulerian angles θ_e , ψ_e , and ϕ_e . To obtain a specified angular orientation, the aircraft must be rotated in the following sequence. First, rotation through angle ψ_e about

the inertial Y axis. Second, rotation through angle θ_e about an intermediate axis (i axis), which coincides *at this point only* with the vehicle roll axis (x axis). Finally, rotation through angle ϕ_e about the vehicle z axis. With this definition, the angular velocity vector can be expressed as

$$\vec{\omega} = \dot{\psi}_e \vec{u}_Y + \dot{\theta}_e \vec{u}_i + \dot{\phi}_e \vec{u}_z \quad (\text{A-168})$$

By solving for the projections of the vehicle axes on the Euler angle rotation axes the following relationships can be obtained.

$$\vec{u}_Y = \vec{u}_z \cos \theta_e - \vec{u}_x \sin \theta_e \quad (\text{A-169})$$

$$\vec{u}_z = \vec{u}_Y \cos \phi_e - \vec{u}_x \sin \phi_e \quad (\text{A-170})$$

and
$$\vec{u}_i = \vec{u}_x \cos \phi_e - \vec{u}_Y \sin \phi_e \quad (\text{A-171})$$

From Equations (A-161) and (A-168) to (A-171) the relation between vehicle frame and Euler angle velocity components is found as follows

$$\dot{\theta} = \dot{\psi}_e \sin \phi_e \cos \theta_e + \dot{\theta}_e \cos \phi_e \quad (\text{A-172})$$

$$\dot{\psi} = \dot{\psi}_e \cos \phi_e \cos \theta_e - \dot{\theta}_e \sin \phi_e \quad (\text{A-173})$$

$$\dot{\phi} = \dot{\phi}_e - \dot{\psi}_e \sin \theta_e \quad (\text{A-174})$$

Substituting $\dot{\psi} = 0$ (no yaw) the above equations can be solved to give

$$\dot{\theta}_e = \dot{\theta} \cos \phi_e \quad (\text{A-175})$$

$$\dot{\phi}_e = \dot{\phi} + \dot{\theta} \sin \phi_e \tan \theta_e \quad (\text{A-176})$$

$$\dot{\psi}_e = \dot{\theta} \sin \phi_e \sec \theta_e \quad (\text{A-177})$$

The above three equations are the required transformation equations which convert velocities in the vehicle frame ($\dot{\theta}$, $\dot{\phi}$ and $\dot{\psi}$) to those in the Eulerian frame ($\dot{\theta}_e$, $\dot{\phi}_e$ and $\dot{\psi}_e$). The Eulerian angular velocities can then be integrated to uniquely fix the instantaneous orientation of the aircraft.

The Flow Model

The flow model determines the variations in pressures and flows as a function of time. There are three parts to the flow model: the fluid chambers (i.e., plenum, cushion and trunk), the pressure relief valve, and the fan. The principal assumptions of the flow model are as follows.

- a) The flow through all orifices is one-dimensional and quasi-static, i.e., the pressure in the plane of the orifice is uniform, and the unsteady state terms in Bernoulli's equation are small compared to the change in velocity head.
- b) The flow through the orifices is incompressible, i.e., the pressure drop is small compared to the total pressure, and the air density is constant.

- c) The pressure and volume changes of the air during expansion and compression in the various fluid chambers are governed by a polytropic relationship, i.e., $p v^k = \text{const.}$

The Fluid Chambers

Plenum - From the polytropic pressure-density relation

$$\frac{(P_p + P_a)}{\rho^k} = \text{constant} \quad (\text{A-178})$$

Taking time derivatives,

$$\frac{dP_p}{dt} = \frac{k(P_p + P_a)}{\rho} \cdot \frac{d\rho}{dt} \quad (\text{A-179})$$

Conservation of mass in the plenum requires that

$$\begin{aligned} \frac{d}{dt} (\rho V_p) &= \rho Q_f - \rho Q_{pa} \\ &\quad - \rho Q_{pc} - \rho Q_{pt} - \rho Q_v \end{aligned} \quad (\text{A-180})$$

From Equations (A-179) and (A-180),

$$\begin{aligned} \frac{d}{dt} P_p &= \frac{k(P_p + P_a)}{(V_p)} (Q_{fx} - Q_{pa} \\ &\quad - Q_{pc} - Q_{pt} - Q_v) \end{aligned} \quad (\text{A-181})$$

Cushion - The continuity equation for the cushion is similar to that of the plenum but with an additional term to include the rate of change of cushion volume due to motion.

$$\frac{dP_c}{dt} = \frac{k(P_c + P_a)}{V_c} \left[Q_{pc} + Q_{tc} - Q_{ca} - \frac{dv_c}{dt} \right] \quad (A-182)$$

where

$$\frac{dv_c}{dt} = \text{rate of change of cushion volume.}$$

Trunk - The continuity equation for the trunk is similar to that of the cushion

$$\frac{dP_t}{dt} = \frac{k(P_t + P_a)}{V_t} \left[Q_{pt} - Q_{tc} - Q_{ta} - \frac{dv_t}{dt} \right] \quad (A-183)$$

where

$$\frac{dv_t}{dt} = \text{rate of change of trunk volume.}$$

The Pressure Relief Valve

A schematic diagram of the pressure relief valve is shown in Figure 57. The valve is modelled as a second order mass-spring-dashpot system. The equation of unrestrained valve motion (i.e., the valve motion if stops were absent) is found from the relationship below.

$$m_v \ddot{x}_v + z_v \dot{x}_v + k_v x_v = (P_p - P_{pb}) A_v \quad (A-184)$$

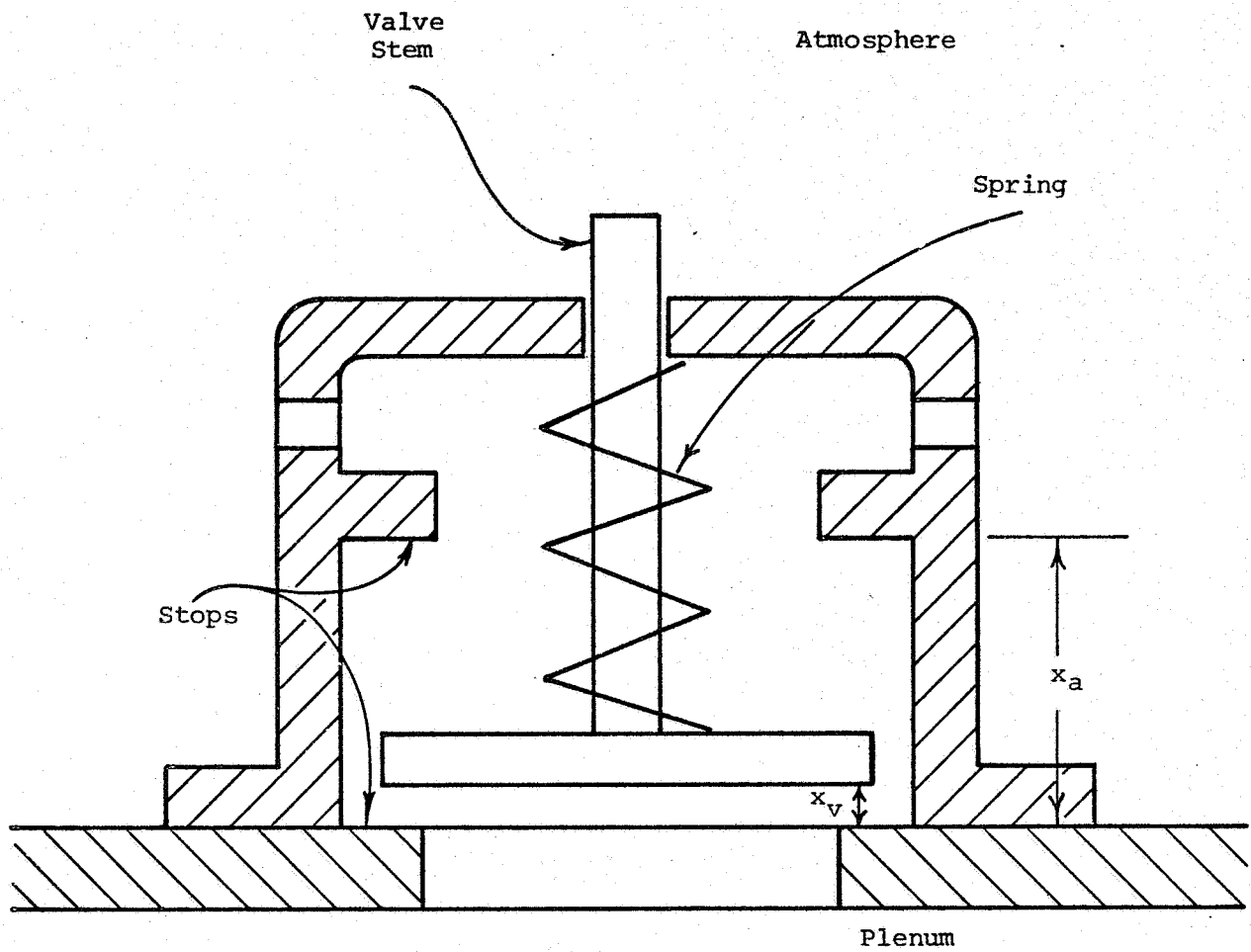


Figure 57. Schematic Diagram of Pressure Relief Valve

The above equation neglects the aircraft acceleration in comparison to the valve stem acceleration.

Due to the presence of stops, there are two constraints on valve motion.

(i) If $x_v \leq 0$, and $P_p < P_{pb}$

Then $\dot{x}_v = \ddot{x}_v = 0$

(ii) If $x_v \geq x_a$ and $P_p A_v > P_{pb} A_v + k_v x_a$

Then $\dot{x}_v = \ddot{x}_v = 0$

where x_a is the range of valve motion between stops. The above constraints ensure that the valve motion does not exceed the stop limits.

The vent area A_v for a given valve displacement x_v is found from

$$A_v = x_v S_v \quad (A-185)$$

where S_v is an equivalent valve periphery which can be a constant or be a function of the valve displacement depending on the valve design. The flow through the valve, which depends on the vent area A_v , is given by

$$Q_v = A_v C_v \sqrt{2P_p / \rho N_v} \quad (A-186)$$

where C_v is the discharge coefficient of the valve and N_v is the number of (identical) relief valves.

The Fan

The dynamic equations for the fan are

$$\frac{dQ_{fx}}{dt} = \frac{P_f + P_{af} - P_p}{I_f} \quad (A-187)$$

where I_f is the inertance of the fan and Q_{fx} is the dynamic fan flow, and

$$P_f = f(Q_{fx}) \quad (A-188)$$

where the function represents the static fan characteristic for positive and negative flow rates. The fan volume, represented by the fan capacitance is lumped together with the plenum volume, so that V_p in Equation (A-181) includes the added volume due to the fan.

REFERENCES

1. Earl, T. Desmond; Air Cushion Landing Gear Feasibility Study. Tech Report AFFDL-TR-67-32, Wright-Patterson AFB, Ohio, May 1967
2. Earl, T. Desmond; Cooper, Richard H.; Air Cushion Landing Gear for Aircraft. Tech Report AFFDL-TR-68-124, Wright-Patterson AFB, Ohio, August 1968
3. Stauffer, C. L.; Ground/Flight Test Report of Air Cushion Landing Gear (LA-4). Tech. Report AFFDL-TR-69-23, Wright-Patterson AFB, Ohio, September 1969
4. Ryken, John M.; A Study of Air Cushion Landing Systems for Space Shuttle Vehicles. NASA CR-111803, December 1970
5. Coles, A. V.; Air Cushion Landing System CC-115 Aircraft. Tech. Report AFFDL-TR-72-4, Part 1. Wright-Patterson AFB, Ohio, May 1972
6. Ryken, John M.; A Study of Air Cushion Landing Systems for Recovery of Unmanned Aircraft. Tech Report AFFDL-TR-72-87, Wright-Patterson AFB, Ohio, July 1972
7. Ryken, John M.; Design of an Air Cushion Recovery System for the Jindivik Drone Aircraft. Tech. Report AFFDL-TR-74-38, Wright-Patterson, AFB, Ohio, March 1976
8. Earl, T. Desmond; ACLS for a Commercial Transport. Society of Automotive Engineers. Paper No. 740452, May 1974
9. Earl, T. D.; Stauffer, C. L.; and Satterlee, C. E.; Tests of the Bell Aerospace LA-4 ACLS fitted with Suction Braking and Predictions for other Aircraft. Tech. Report AFFDL-TR-75-135, Wright-Patterson AFB, Ohio, November 1975
10. Gorman, Dennis, M.; Equilibrium Characteristics of a Distributed Peripheral Jet. M.S. Thesis, Air Force Institute of Technology, Wright-Patterson AFB, Ohio, March 1970
11. Digges, Kennerly H.; Theory of an Air Cushion Landing System for Aircraft. Tech. Report AFFDL-TR-71-50, Wright-Patterson AFB, Ohio, June 1971
12. Vaughan, John C.; and Steiger, James T.; Vertical Energy Absorption Analysis of an Air Cushion Recovery System. Tech. Memorandum AFFDL-TM-72-03-FEM, Wright-Patterson AFB, Ohio, August 1972

13. Vaughan, John C.; Campbell, Shade; and Pool, David J.; Static and Drop Tests of a Quarter-Scale Model of the CC-115 Aircraft Equipped with an Air Cushion Landing System. Tech. Memorandum AFFDL-TM-72-01-FEM, Wright-Patterson AFB, Ohio, September 1972
14. Kunstadt, Ernest; Study of Reverse-Flow Characteristics of a Tip Fan and an Ejector. M.S. Thesis, Air Force Institute of Technology, Wright-Patterson AFB, Ohio, 1973
15. Parker, Philip, M.; Air Cushion Landing System Performance on a Tenth-Scale Model Jindivik RPV. Tech. Memorandum AFFDL-TM-74-58-FEM, Wright-Patterson AFB, Ohio, March 1974
16. Rogers, John R.; Two-Dimensional Air Cushion Landing System Peripheral Jet Configuration Study. Tech. Report AFFDL-TR-73-5, Wright-Patterson AFB, Ohio, September 1973
17. Rodrigues, John C.; Drop and Static Tests on a Tenth-Scale Model of an Air Cushion Landing System (ACLS). Tech. Report AFFDL-TR-73-46, Wright-Patterson AFB, Ohio, September 1973
18. Carreras, Eduardo M.; Static Two-Dimensional Performance of a Cushion Fed Air Cushion Landing System. Tech. Memorandum AFFDL-TM-74-56-FEM, Wright-Patterson AFB, Ohio, March 1974
19. Bauer, Frederic C.; Air Cushion Landing System Drop Dynamics Theory (Mechanical). Tech. Memorandum AFFDL-TM-74-57-FEM, Wright-Patterson AFB, Ohio, March 1974
20. Stuart, John L.; An Experimentally Based Prediction of the Static Performance in the Vertical Direction of an Air Cushion Landing System. Tech. Memorandum AFFDL-TM-74-55-FEM, Wright-Patterson AFB, Ohio, March 1974
21. Vaughan, John C.; Steiger, James T.; Pool, David J.; and Campbell, Shade; Laboratory Tests of an Air Cushion Recovery System for the Jindivik Aircraft. Tech. Report AFFDL-TR-74-64, Wright-Patterson AFB, Ohio, April 1974
22. Han, Lit S.; Air Cushion Pressure During Stiff-Operation for Air Cushion Landing System, Part I Theory. Tech. Report AFFDL-TR-71-4, Part I, Wright-Patterson AFB, Ohio, May 1971
23. Han, Lit S.; Air Cushion Pressure During Stiff-Operation for Air Cushion Landing Systems, Part II & Experiments. Tech. Report AFFDL-TR-71-4 Part II, Wright-Patterson AFB, Ohio, March 1972

24. Han, Lit S.; Two-Dimensional Discrete-Jet Configuration for an Air Cushion Landing System. Tech. Memorandum AFFDL-TM-75-114-FEM, Wright-Patterson AFB, Ohio, July 1975
25. Forzono, Carmine J.; An Experimental Investigation of Trunk Flutter of an Air Cushion Landing System. M.S. Thesis, The Ohio State University, 1975
26. Captain, K.M.; Boghani, A. B.; and Wormley, D.N.; Dynamic Heave-Pitch Analysis of Air Cushion Landing Systems. NASA CR-2530, May 1975
27. Lee, David G.; and Davidson, H. Dulany; Low Speed Aerodynamic Characteristics of an A-4 Aircraft with an Air Cushion Landing System. Evaluation Report AL-98, Naval Ship Research and Development Center, Bethesda, Maryland, February 1973
28. Milns, Peter; and Gardner, Lloyd; A-4 Twin Pod Air Cushion Test Specimen. Report D180-15370-1, The Boeing Company, Seattle, Washington, March 1973
29. Thompson, William C.; Landing Performance of an Air Cushion Landing System Installed on a 1/10-Scale Dynamic Model of the C-8 Buffalo Airplane. NASA TN D-7295, September 1973
30. Leland, Trafford J. W.; and Thompson, William C.; Landing-Impact Studies of a 0.3 Scale Model Air Cushion Landing System for a Navy Fighter Airplane. NASA TN D-7875, March 1975
31. Ho, F. H.; Analysis of the Transient Dynamic Pitch Characteristics of an Air Cushion Recovery System for the Jindivik Aircraft. B. F. Goodrich Research and Development Center, Ohio, July 1974
32. Bass, R. L.; and Johnson, J. E.; An Experimental Study of Skirt Flutter on Surface Effect Take-off and Landing (SETOL) Craft. Contract N62269-73-C-0216, Southwest Research Institute, San Antonio, Texas, June 1973
33. McCudden, H. B.; Sorenson, P. D.; Lutz, G. R.; et al.; Conceptual Design of an Air Cushion Landing System for an Unmanned Aircraft. Tech. Report AFFDL-TR-72-155, Wright-Patterson AFB, Ohio, January 1973

34. Hurkamp, Charles H.; The Potential Influence of the ACLS on the Development of Logistic Cargo Aircraft. Paper presented at 1st Conference on Air Cushion Landing Systems, The University of Tennessee, Tullahoma, Tennessee, December 1972.
35. Thompson, W.C.; Boghani, A.B.; and Leland, T.J.W.; Experimental and Analytical Dynamic Flow Characteristics of an Axial Flow Fan for an Air Cushion Landing System Model, NASA TN D 8413, June 1977.